Finite element modelling of three dimensional fluid-structure interaction.

Taylor, Richard

Swansea University
Prifysgol Abertawe

Finite Element Modelling of Three Dimensional Fluid-Structure Interaction

Richard Taylor

Submitted to Swansea University in fulfilment
of the requirements for the Degree of Doctor of Philosophy

2013

DECLARATION

This work has not previously been accepted in substance for any degree and is not being concurrently submitted in candidature for any degree.

Signed ..... (candidate)

Date 08/01/13

STATEMENT 1

This thesis is the result of my own investigations, except where otherwise stated. Where correction services have been used, the extent and nature of the correction is clearly marked in a footnote(s).

Other sources are acknowledged by footnotes giving explicit references. A bibliography is appended.

Signed ..... (candidate)

Date 08/01/13

STATEMENT 2

I hereby give consent for my thesis, if accepted, to be available for photocopying and for inter-library loan, and for the title and summary to be made available to outside organisations

Signed ..... (candidate)

Date 08/01/13

Summary

This work is focused on the numerical modelling of fluid-structure interaction in three dimensions. Both internal and external laminar flow around flexible bodies are considered.

The fluid flow simulated is based on the incompressible Navier-Stokes equations and the general focus is on laminar Newtonian flow. The *streamline upwind/ pressure stabilising Petrov-Galerkin* (SUPG/PSPG) method is employed to achieve a stable low order finite element discretisation of the fluid, while the solid is discretised spatially by a standard Galerkin finite element approach. The behavior of the solid is governed by Neo-Hooke elasticity. For temporal discretisation the discrete implicit *generalised-α* method is employed for both the fluid and the solid domains. The motion of the fluid mesh is solved using an *arbitrary Lagrangian-Eulerian* (ALE) scheme employing a nonlinear pseudo-elastic mesh update method. The fluid-solid interface is modelled using a finite element interpolation method that allows for non-matching meshes and satisfies the required conservation laws.

The resulting sets of fully implicit strongly coupled nonlinear equations are then decomposed into a general framework consisting of fluid, interface and solid domains. These equations are then solved using different solution techniques consisting of strongly coupled *monolithic Newton* and *block Gauss-Seidel* methods as well as a weakly coupled *novel staggered scheme.* These solvers are employed to solve a number of three dimensional numerical examples consisting of:

External flow:

- a soft elastic beam fixed at both ends
- a thin cantilever plate

Internal flow:

- a slender flexible pipe fixed at both ends
- a slender pipe with a 'weak patch'
- a slender pipe fixed at one end

The criteria of rate of convergence, stability, accuracy and computational cost are used to determine the relative suitability of each solver. Where possible, these strategies are also compared to available references or analytical solutions.

Acknowledgements

I would like to thank my supervisors, Prof. Djorje Perić and Dr. Wulf Dettmer, whose guidance and support have proven invaluable throughout the course of this work. I would also like to thank collegues Dr. Maartje Joosten and Dr. Deniz Somer, whose early assistance in my introduction to the field of FSI was greatly appreciated.

Additionally, I thank Swansea University in general and the School of Engineering specifically for providing the helpful and supportive work environment that I have enjoyed these past years. In particular I wish to thank my friends and collegues of the C2EC: Kevin Mason, Hannah Buckland, Sean Walton, Dan Memory, Bruce Jones, Elliot Parramore, Mike Weberstadt, Patrick Wlodarski, and Andy Tappenden with whom I enjoyed many experiences both in, and out of the office.

Finally I wish to thank my family for their constant support, both financial and emotional. Without them none of this would have been possible.

DECLARATION

This work has not previously been accepted in substance for any degree and is not being concurrently submitted in candidature for any degree.

Signed ..... (candidate)

Date .....

STATEMENT 1

This thesis is the result of my own investigations, except where otherwise stated. Where correction services have been used, the extent and nature of the correction is clearly marked in a footnote(s).

Other sources are acknowledged by footnotes giving explicit references. A bibliography is appended.

Signed ..... (candidate)

Date .....

STATEMENT 2

I hereby give consent for my thesis, if accepted, to be available for photocopying and for inter-library loan, and for the title and summary to be made available to outside organisations.

Signed ..... (candidate)

Date .....

Contents

Chapter 1

Introduction

1.1 Introduction to FSI

The study of fluid-structure interaction (FSI) may be applied to a wide variety of situations occurring in both nature and controlled environments. Some physical phenomena which merit numerical simulation include:

Aerospace engineering: The study of flutter and vortex induced vibration is essential to the stability of aircraft in flight.

Civil engineering: Natural wind flow around slender structures such as lattice towers, bridges, sky scrapers and power grids may sometimes result in small oscillating deflections which grow larger over time. Such oscillations occurring at the resonant frequency of the structure may result in catastrophic failure.

Mechanical engineering: Internal flow problems such as those found in internal combustion engines require careful simulation during design to ensure optimum performance.

Biomedical engineering: The human body contains many examples of fluid-structure interaction, particularly when dealing with blood flow. The design of biomedical implants such as a replacement heart valve is heavily dependent on the accurate simulation of the impact of the apparatus on blood flow in the area.

In general, the term *fluid-structure interaction* may be said to describe the strongly coupled behavior of a fluid flowing around a solid object that exerts a traction force on

the body, resulting in a deflection of the solid which in turn affects the fluid flow through moving boundary conditions. While solutions of individual problems governed by fluid and solid mechanics are standard, the solution of coupled FSI systems is currently an area of intense research. With the continuous advancement of computational resources available resulting in the steady growth of computer-aided engineering (CAE), many new applications of numerical approximation techniques to computational simulation of FSI have been developed in the last decade. It should be noted that while the computational implementation techniques may be new, many of the numerical iteration techniques they are based on, such as the Newton-Raphson method, are not. This work employs solution techniques developed and implemented primarily in two dimensions by Prof. D. Perić and Dr. W. Dettmer. Publications of these solution strategies include: the monolothic Newton method, see *e.g.* Dettmer and Perić [16, 19, 20, 21, 51, 22], the block Gauss-Seidel procedure, see *e.g.* Joosten *et al* [39, 40], and the novel staggered scheme, see *e.g.* Dettmer and Perić [23].

At present the scientific community has yet to establish a set of widely available three dimensional benchmarks in the numerical simulation of FSI behavior. Additionally, it is still relatively unclear which of the many solution techniques currently available is most suitable. It is the aim of this work to provide some advancement in the available knowledge in these areas of research. In the following sections of this chapter, additional details of the aim of this work and the layout of the subsequent chapters are briefly provided.

1.2 Aim of the Thesis

The aim of this work is to employ stabilised finite element numerical solution techniques to solve a variety of three dimensional FSI problems in order to present the results obtained with the objective of establishing useful benchmark models. A performance analysis of the *monolithic Newton*, *block Gauss-Seidel*, and *novel staggered* solution methods is also to be presented in order to assess their relative suitability. All of the solvers employed in this work may be considered to be robust and applicable to a wide range of FSI problems, however due to a lack of established benchmark model problems in three dimensional FSI analysis it is currently unclear which of these methods may be the most suitable. The analysis to be presented will be based on the criteria of: rate of convergence, stability, accuracy,

and computational cost. This work therefore aims to present a variety of external and internal flow FSI model problems in three dimensions. The focus in this work is restricted to laminar incompressible Newtonian fluid flow, with the fluid domain discretised using stabilised finite elements adapted to capture the motion of the fluid mesh along the fluid-solid interface.

1.3 Layout of the Thesis

Chapter 2: The application of numerical modelling to FSI is introduced using simple one dimensional galloping and flutter model problems. A small analysis of the Newton-Raphson and Gauss-Seidel iterative methods in the context of the model problems is then presented.

Chapter 3: The mathematical formulation of the governing equations employed in this work to describe the moving reference frame, incompressible Navier-Stokes equations and boundary conditions in both the fluid and the solid is provided. An introduction to time integration is also presented, to be described in more detail in Chapter 4.

Chapter 4: The finite element discretisation of both the fluid and solid domains is described, with a detailed adaptation of the fluid finite element discretisation to the moving reference frame to be provided in chapter 5. The stabilisation of fluid elements using the SUPG/PSPG technique, and the application of the discrete implicit generalised-α method for time integration is presented. A few examples of two dimensional Eulerian fluid finite element meshes employed to solve fluid flow are then provided.

Chapter 5: A detailed description is presented of the application of the arbitrary Lagrangian-Eulerian description of fluid flow to adapt the finite element discretisation of the fluid to a moving mesh. The nonlinear pseudo-elastic method used to describe the mesh movement is provided, as well as the finite element interpolation technique employed to describe the fluid-solid interface.

Chapter 6: A decomposition of the full FSI system into fluid, interface and solid domains is presented in order to present a simple description of the solution techniques employed in this work. The monolithic Newton, block Gauss-Seidel and novel staggered solution methods are then described, and a summary of their applied algorithms provided.

Chapter 7: An external flow model problem consisting of a soft elastic beam, fixed at both

ends and subjected to a steady fluid flow is solved using the three solution methods and a comparison of results obtained is provided.

Chapter 8: A more complex external flow model problem than chapter 7 is presented, consisting of a thin flexible plate fixed at one end to a fully rigid body and subjected to steady fluid flow. In addition to a comparison of the three solution methods, results obtained are also compared to existing publications containing the same model problem presented by von Scheven [53] and Kassiotis et al [41, 42].

Chapter 9: First, an internal flow model problem consisting of a thin flexible pipe subjected to an oscillating fluid flow is presented. The pipe is fixed at both ends, with the downstream end fixed in such a way as to allow radial deflection only. A second model problem is then presented in which a small section of the pipe is set to half of the stiffness of the pipe in order to present a fully asymmetric model problem.

Chapter 10 An internal flow model problem consisting of a thin flexible pipe fixed only at one end, and subjected to a steady internal flow is presented using a range of increasing inflow velocities in order to obtain the critical velocity at which the free end of the pipe will begin to oscillate. This value for the critical velocity is then compared to an analytical solution presented by Blevins [5].

Chapter 11: The results obtained from the previous example chapters are summarised, and the relative suitability of the different solution techniques observed throughout is discussed. Final conclusions are presented, along with a discussion of room for future work.

Chapter 2

Basics of FSI with Model Problem

2.1 Introduction to Solving FSI

A body subjected to a steady, incompressible fluid flow may sometimes undergo oscillating translational displacement of increasing amplitude, known as 'Galloping'. In this section, a one dimensional, one degree of freedom model of this behavior is considered, such as the mass-spring system shown in figure 2.1. This model is then used as a basis for an introduction to solving FSI using numerical methods.

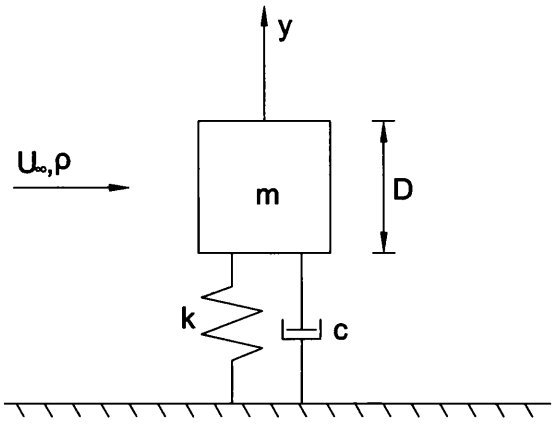

Figure 2.1: Damped mass-spring system.

The system consists of a mass m, supported by a spring of stiffness k and damping

factor c, free to oscillate in the vertical direction only and subjected to a horizontal steady, incompressible fluid flow of velocity U_∞ and density ρ. Applying equilibrium to this system results in the following governing equation of motion, in which the sum momentum, damping, and stiffness of the structure are equated to the vertical force produced by the fluid acting on the structure.

$$m\ddot{y} + c_y\dot{y} + k_y y = F_y \tag{2.1}$$

In the simplified system being considered, the single degree of freedom is in the y direction. Therefore only vertical force is considered in equilibrium. The vertical force generated by a horizontal, inviscid fluid flow can be calculated by applying the laws of conservation of mass and momentum to obtain a relationship of known structural and material properties.

$$F_y = \frac{1}{2}\rho U_\infty^2 D C_y(\alpha), \tag{2.2}$$

where $C_y(\alpha)$ is an aerodynamic coefficient dictated by the solid geometry and the angle of the fluid flow relative to the horizontal axis, known as *the angle of attack*, α. Inserting this identity into equation (2.1) gives a governing equation of motion where only the $\mathbf{y}, \dot{\mathbf{y}}, \ddot{\mathbf{y}}$ values are unknown.

$$m\ddot{y} + c_y\dot{y} + k_y y = \frac{1}{2}\rho U_\infty^2 D C_y(\alpha) \tag{2.3}$$

2.1.1 Discretising the System

Before attempting to solve this system of governing equations computationally, it is necessary to apply an appropriate time integration scheme. For this exercise, a single step implicit time integration scheme was chosen. Examples of such schemes include the backward Euler, generalised midpoint and the generalised-α methods, however, in this case the trapezoidal rule was implemented to integrate $\mathbf{y}$, $\dot{\mathbf{y}}$, and $\ddot{\mathbf{y}}$ in time as follows.

$$y_{n+1} = y_n + \frac{\Delta t}{2}[\dot{y}_{n+1} + \dot{y}_n]$$

$$y_{n+1} = y_n + \Delta t \dot{y}_n + \frac{\Delta t^2}{4}[\ddot{y}_{n+1} + \ddot{y}_n] \tag{2.4}$$

In order to identify the forward values of $\dot{\mathbf{y}}$ and $\ddot{\mathbf{y}}$, these equations are rearranged to give:

$$\dot{y}_{n+1} = \frac{2(y_{n+1} - y_n)}{\Delta t} - \dot{y}_n$$

$$\ddot{y}_{n+1} = \frac{4(y_{n+1} - y_n)}{\Delta t^2} - \frac{4\dot{y}_n}{\Delta t} - \ddot{y}_n \tag{2.5}$$

2.1.2 Solving the System Numerically

In order to solve this system for the unknown values of $\mathbf{y}, \dot{\mathbf{y}}, \ddot{\mathbf{y}}$, a variety of numerical solution methods could be implemented, such as Newtonian or Gaussian methods. In this case the Newton-Raphson iterative method was employed. This method was implemented by taking the second integration in time using the trapezoidal method.

$$y_{n+\frac{1}{2}} = \frac{y_{n+1} + y_n}{2} = \frac{2y_n + \Delta y_n}{2}$$

$$\dot{y}_{n+\frac{1}{2}} = \frac{y_{n+1} - y_n}{\Delta t} = \frac{\Delta y_n}{\Delta t}$$

$$\ddot{y}_{n+\frac{1}{2}} = \frac{2(y_{n+1} - y_n)}{\Delta t^2} - \frac{2\dot{y}_n}{\Delta t} = \frac{2\Delta y_n}{\Delta t^2} - \frac{2\dot{y}_n}{\Delta t}, \tag{2.6}$$

and rearranging the governing equation in the residual form as:

$$R = m\ddot{y} + c_y\dot{y} + k_y y - \frac{1}{2}\rho U_\infty^2 D C_y(\alpha) \tag{2.7}$$

Then solving for the unknown vertical displacement $\mathbf{y}$ iteratively using:

$$y_{n+1} = y_n - \frac{R}{K} \quad \text{where} \quad K = \frac{\delta R}{\delta y} \tag{2.8}$$

2.1.3 1-DOF Model Problem

In order to produce viable results using this method, the properties of the body and its support were set to $k = 3.0$, $c = 2.0$, $m = 20.0$. The chord length of the body was set to $D = 1.0$. The density of the surrounding fluid was set to $\rho = 1.0$, with a range of inflow velocities considered up to a maximum of $U_\infty = 2.5$. Solving this system produced a range of maximum steady amplitudes of oscillation corresponding to the range of inflow velocities considered, shown in Figure 2.2.

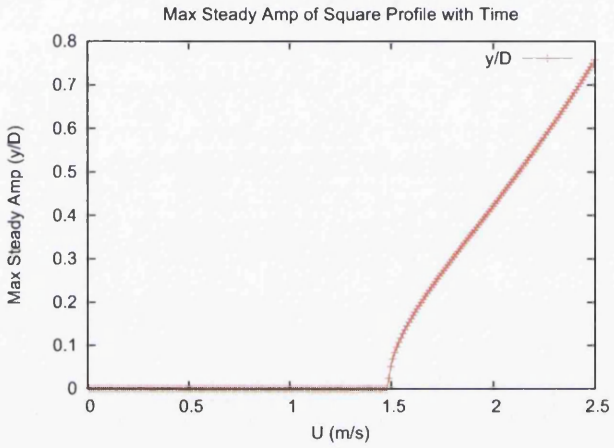

Figure 2.2: 1-DOF Model Problem: Max Steady Amplitude vs Inflow Velocity

Figure 2.2 shows that the oscillations of the system as a result of the inflow velocity are positively damped up to the critical velocity of $U_{crit} \approx 1.5$, at which point the system begins to experience increasingly large amplitude oscillations known as divergence. At $U = 2.5$ the maximum steady amplitude of the system is $\frac{y}{D} = 0.75751$.

2.2 Comparison of N-R and G-S methods solving 2-DOF Flutter

Flutter is defined by aerospace terminology as the coupled torsion-plunge instability of a structure by such texts as *e. g.* Blevins [5] and Den Hartog [27]. More specifically, the fields of mechanical, civil and aerospace engineering have a vested interest in the effect that flutter can have on slender structures, as this can result in large-scale deformations or even total structural failure, such as the collapse of the Takoma Narrows bridge in 1940.

2.2.1 Description of Model Problem

As an introduction to the computational modelling of flutter, a simplified set of equations governing flutter behavior were derived and solved using the Newton-Raphson and Gauss-Seidel iterative methods in order to highlight some of the differences between them. Consider the same mass-spring system used in section 2.1, allowed to deflect in both vertical translation and rotation, as shown in figure 2.3.

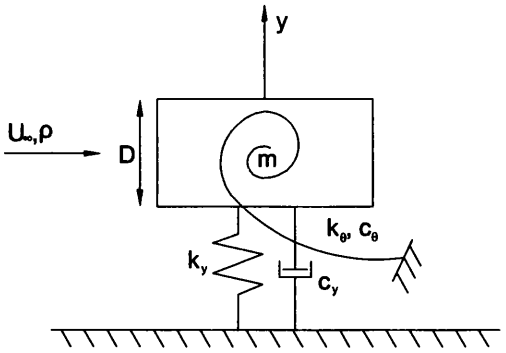

Figure 2.3: 2-DOF damped mass-spring system.

By applying equilibrium to this system we obtain the following set of stongly coupled equations of motion:

$$m\ddot{y} + zm\ddot{\theta} + c_y\dot{y} + k_y y = -\frac{1}{2}\rho U_\infty^2 D C_L(\alpha(\theta, \dot{\theta}, \dot{y}))$$

$$I_p\ddot{\theta} + zm\ddot{y} + c_\theta\dot{\theta} + k_\theta\theta = \frac{1}{2}\rho U_\infty^2 D^2 C_M(\alpha(\theta, \dot{\theta}, \dot{y}))$$

$$\alpha = \alpha_0 + \theta + \frac{\dot{y}}{U_\infty} + \frac{\dot{\theta}R}{U_\infty} \tag{2.9}$$

For the coefficients of lift and torque a linear relationship to the angle of attack was chosen, based on the data presented in Dettmer and Perić [19].

$$C_L(\alpha) = 2.5 + 0.11\alpha$$

$$C_M(\alpha) = -0.15 + 0.004\alpha \tag{2.10}$$

where α is the angle of attack in radians.

2.2.2 Discretisation: Trapezoidal Rule

The displacement, velocity, and acceleration of the rigid body in twist and plunge were discretised using the trapezoidal rule as in 2.1. The system was then solved at each time step by employing a numerical method within an iterative loop. The intermediate values of the system variables were discretised using the trapezoidal rule for the half step as follows.

$$\mathbf{u}_{n+\frac{1}{2}} = \frac{\mathbf{u}_{n+1} + \mathbf{u}_n}{2} = \frac{2\mathbf{u}_n + \Delta\mathbf{u}_n}{2}$$

$$\dot{\mathbf{u}}_{n+\frac{1}{2}} = \frac{\mathbf{u}_{n+1} - \mathbf{u}_n}{\Delta t} = \frac{\Delta\mathbf{u}_n}{\Delta t}$$

$$\ddot{\mathbf{u}}_{n+\frac{1}{2}} = \frac{2(\mathbf{u}_{n+1} - \mathbf{u}_n)}{\Delta t^2} - \frac{2\dot{\mathbf{u}}_n}{\Delta t} = \frac{2\Delta\mathbf{u}_n}{\Delta t^2} - \frac{2\dot{\mathbf{u}}_n}{\Delta t} \quad \text{where} \quad \mathbf{u}_n = \begin{bmatrix} y_n \\ \theta_n \end{bmatrix} \tag{2.11}$$

The coupled governing equations were then rewritten in the discrete residual form.

$$R_1 = m(\frac{2\Delta y_n}{\Delta t^2} - \frac{2\dot{y}_n}{\Delta t}) + zm(\frac{2\Delta\theta_n}{\Delta t^2} - \frac{2\dot{\theta}_n}{\Delta t}) + c_y(\frac{\Delta y_n}{\Delta t}) + k_y(\frac{2y_n + \Delta y_n}{2}) + \frac{1}{2}\rho U_\infty^2 D(2.5 + 0.11(\alpha_0 + \frac{2\theta_n + \Delta\theta_n}{2} + \frac{\Delta y_n}{\Delta t U_\infty} + \frac{\Delta\theta_n R}{\Delta t U_\infty}))$$

$$R_2 = Ip(\frac{2\Delta\theta_n}{\Delta t^2} - \frac{2\dot{\theta}_n}{\Delta t}) + zm(\frac{2\Delta y_n}{\Delta t^2} - \frac{2\dot{y}_n}{\Delta t}) + c_\theta(\frac{\Delta\theta_n}{\Delta t}) + k_\theta(\frac{2\theta_n + \Delta\theta_n}{2}) - \frac{1}{2}\rho U_\infty^2 D^2(-0.15 - 0.004(\alpha_0 + \frac{2\theta_n + \Delta\theta_n}{2} + \frac{\Delta y_n}{\Delta t U_\infty} + \frac{\Delta\theta_n R}{\Delta t U_\infty})) \quad (2.12)$$

2.2.3 Solving the System Numerically

In the interest of comparing rates of convergence and stability, the system was solved using both the Newton-Raphson and Gauss-Seidel methods.

The Newton-Raphson Method

The Newton-Raphson method is based on the principle that at the solution:

$$\mathbf{R(u)} + \mathbf{K}\Delta\mathbf{u} = 0 \quad \text{where} \quad \mathbf{K} = \frac{\partial \mathbf{R}}{\partial \Delta \mathbf{u}} = \begin{bmatrix} \frac{\partial R_1}{\partial \Delta y} & \frac{\partial R_1}{\partial \Delta \theta} \\ \frac{\partial R_2}{\partial \Delta y} & \frac{\partial R_2}{\partial \Delta \theta} \end{bmatrix} \quad (2.13)$$

Therefore the system can be rearranged to provide updated values of displacement iteratively converging on the solution using:

$$\Delta\mathbf{u} = -\frac{\mathbf{R(u)}}{\mathbf{K}} \quad (2.14)$$

By first inserting the values:

$$\mathbf{K} = \begin{bmatrix} \frac{2m}{\Delta t^2} + \frac{c_y}{\Delta t} + \frac{k_y}{2} + \frac{1}{2}\rho U_\infty^2 D(0.11(\frac{1}{dtU_\infty})) & \frac{2zm}{\Delta t^2} + \frac{1}{2}\rho U_\infty^2 D(0.11(\frac{1}{2} + \frac{R}{dtU_\infty})) \\ \frac{2zm}{\Delta t^2} - \frac{1}{2}\rho U_\infty^2 D^2(0.004(\frac{1}{dtU_\infty})) & \frac{2I_p}{\Delta t^2} + \frac{c_\theta}{\Delta t} + \frac{k_\theta}{2} - \frac{1}{2}\rho U_\infty^2 D^2(0.004(\frac{1}{2} + \frac{R}{dtU_\infty})) \end{bmatrix} \quad (2.15)$$

The calculated values for the changes of displacement are then used to update the system for each step in time. Applying this numerical method to the system of equations being considered for a variety of time step sizes resulted in the solutions displayed in figures 2.4 and 2.5.

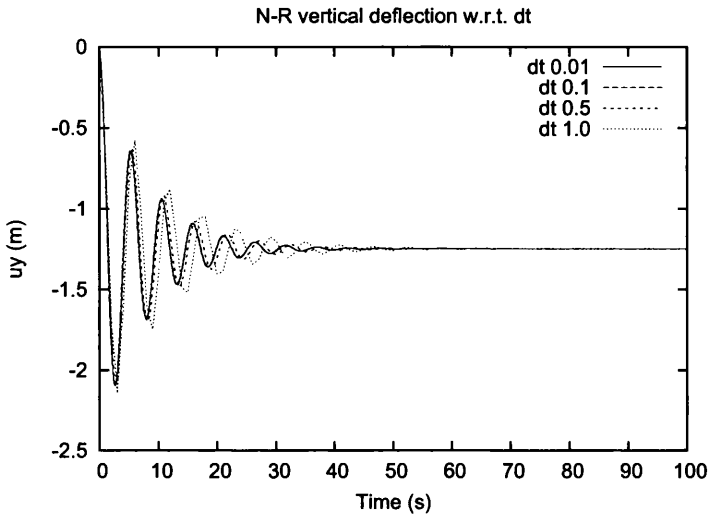

Figure 2.4: Comparison of u_y with dt

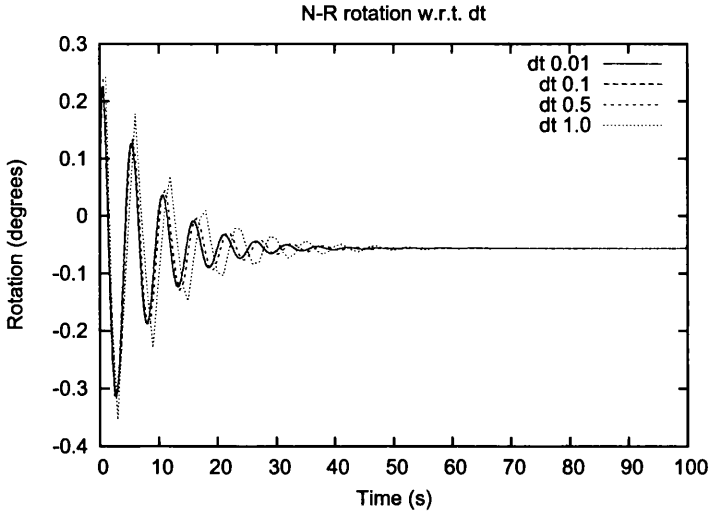

Figure 2.5: Comparison of u_θ with dt

The Gauss-Seidel Method

The Gauss-Seidel iterative method is based on the principle that a discrete system of equations in the form:

$$\mathbf{A}\Delta\mathbf{u} = \mathbf{b}, \tag{2.16}$$

with the matrix $\mathbf{A}$ consisting of the coefficients of the variables represented by the vector $\mathbf{u}$ and the vector $\mathbf{b}$ consisting of the system constants, may be solved for the unknown values of $\Delta\mathbf{u}$ provided that the matrix $\mathbf{A}$ may be decomposed into a diagonal matrix $\mathbf{D}$ and an off-diagonal matrix $\mathbf{N}$ such that:

$$\mathbf{A} = \mathbf{D} + \mathbf{N} \tag{2.17}$$

$$\mathbf{A} = \begin{bmatrix} A_{11} & 0 \\ 0 & A_{22} \end{bmatrix} + \begin{bmatrix} 0 & A_{12} \\ A_{21} & 0 \end{bmatrix} \tag{2.18}$$

This gives us:

$$\begin{aligned} (\mathbf{D} + \mathbf{N})\Delta\mathbf{u} &= \mathbf{b} \\ \mathbf{D}\Delta\mathbf{u} &= \mathbf{b} - \mathbf{N}\Delta\mathbf{u} \end{aligned} \tag{2.19}$$

Which allows the iterative calculation of the changes in the system variables in the form:

$$\Delta\mathbf{u}_{i+1} = \mathbf{D}^{-1}(\mathbf{b} - \mathbf{N}\Delta\mathbf{u}_i) \tag{2.20}$$

Rewriting the system of equations to be solved in this form gave:

$$\mathbf{A} = \begin{bmatrix} \frac{2m}{\Delta t^2} + \frac{c_y}{\Delta t} + \frac{k_y}{2} + \frac{1}{2}\rho U_\infty^2 D(0.11(\frac{1}{dtU_\infty})) & \frac{2zm}{\Delta t^2} + \frac{1}{2}\rho U_\infty^2 D(0.11(\frac{1}{2} + \frac{R}{dtU_\infty})) \\ \frac{2zm}{\Delta t^2} - \frac{1}{2}\rho U_\infty^2 D^2(0.004(\frac{1}{dtU_\infty})) & \frac{2I_p}{\Delta t^2} + \frac{c_\theta}{\Delta t} + \frac{k_\theta}{2} - \frac{1}{2}\rho U_\infty^2 D^2(0.004(\frac{1}{2} + \frac{R}{dtU_\infty})) \end{bmatrix} \tag{2.21}$$

$$\Delta\mathbf{u} = \begin{bmatrix} \Delta y \\ \Delta\theta \end{bmatrix} \tag{2.22}$$

$$\mathbf{b} = \begin{bmatrix} -\frac{1}{2}\rho U_\infty^2 D(2.5 + 0.11(\alpha_0 + \theta_n)) + \frac{2m}{\Delta t}(\dot{y}_n + z\dot{\theta}_n) - k_y y_n \\ \\ \frac{1}{2}\rho U_\infty^2 D^2(-0.15 - 0.004(\alpha_0 + \theta_n)) + \frac{2}{\Delta t}(Ip\dot{\theta}_n + zm\dot{y}_n) - k_\theta \theta_n \end{bmatrix} \tag{2.23}$$

Which were then solved for a variety of time step sizes to obtain the solutions displayed in figures 2.6 and 2.7.

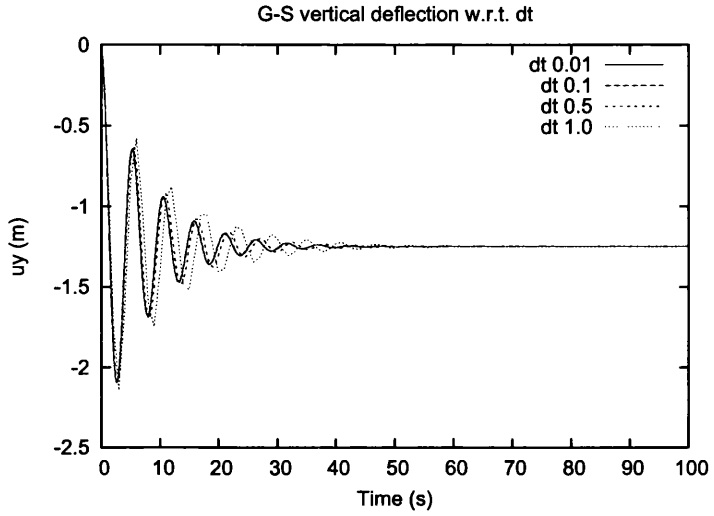

Figure 2.6: Comparison of u_y with dt

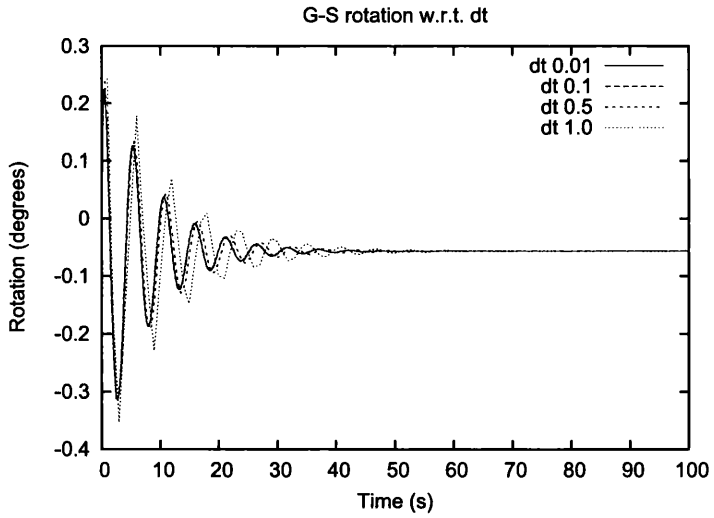

Figure 2.7: Comparison of u_θ with dt

2.2.4 Comparison of Numerical Solution Methods

While both the Newton-Raphson and Gauss-Seidel methods converge on the same solutions, the number of iterations required for convergence and the stability of the different methods vary. By analyzing and comparing these criteria, it is possible to determine the conditions under which a particular solution would be more appropriate. In the case of the model problem considered, with the trapezoidal method employed for time integration, the Newton-Raphson method achieved a significantly greater rate of convergence, as shown in table 2.1, figure 2.8 and figure 2.9.

Table 2.1: Comparison of Convergence

Numerical Method	Iterations to Achieve Tolerance			
	δt 1.0s	0.5s	0.1s	0.01s
Newton-Raphson	3	3	3	3
Gauss-Seidel	18	30	100	218

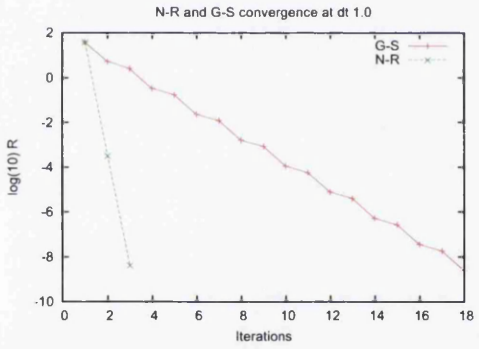

Figure 2.8: Convergence at δt = 1.0 s.

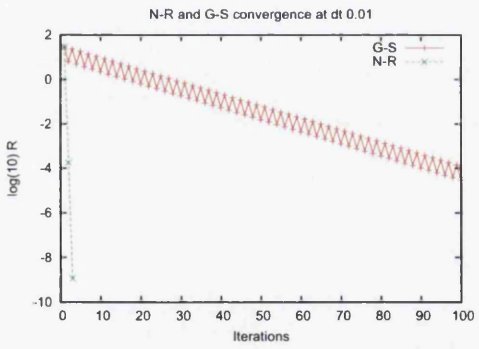

Figure 2.9: Convergence at δt = 0.01 s.

Chapter 3

Mathematical Problem Description

3.1 Discussion of Strong Coupling in Fluid-Structure Interaction

In the previous chapter some simplified models for the behavior of galloping and flutter were presented, however the focus was on the behavior of the solid with the behavior of the fluid simply present in the traction forcing terms. In reality fluid-structure interaction displays strong coupling between the fluid and solid behavior due to the fluid forces acting on the solid causing a deformation of solid geometry, which in turn results in new boundary conditions for the fluid and thus altered fluid behavior. The following chapter presents the mathematical formulation of governing equations which may be considered to express this behavior.

3.2 Mechanics of Fluids

3.2.1 Moving Reference Frame

In order to achieve a suitable mathematical model for solving fluid-structure interactions, a method of applying the finite element method to a fluid body with moving boundary conditions must first be considered. The geometry of the fluid mesh must be allowed to deform as the boundary conditions dictate while the particles of the fluid body flow through

the domain. One possible solution to satisfying these conditions is the formulation of a moving reference frame.

First, we may consider the fluid body ($\mathbf{B}$), the reference domain ($\mathbf{\Omega}$), and their respective initial configurations ($\mathbf{B}_0, \mathbf{\Omega}_0$). We may then further define the relevant coordinate systems $\mathbf{x} \in \mathbf{B}$, $\mathbf{x}_0 \in \mathbf{B}_0$, $\hat{\mathbf{x}} \in \mathbf{\Omega}$, $\hat{\mathbf{x}}_0 \in \mathbf{\Omega}_0$, related by the unique mappings:

$$\mathbf{x} = \phi(\mathbf{x}_0, t), \qquad \hat{\mathbf{x}} = \lambda(\hat{\mathbf{x}}_0, t). \tag{3.1}$$

Note that for each $\mathbf{x} = \hat{\mathbf{x}}$ there will exist the unique mapping

$$\hat{\mathbf{x}}_0 = \psi(\mathbf{x}_0, t) = \lambda^{-1}(\phi(\mathbf{x}_0, t), t). \tag{3.2}$$

With these three relationships, each $\mathbf{x} = \hat{\mathbf{x}} \in (\mathbf{B} \cap \mathbf{\Omega})$ is therefore associated with a material point ($\mathbf{x}_0$) and a reference point ($\hat{\mathbf{x}}_0$) illustrated by figure 3.1:

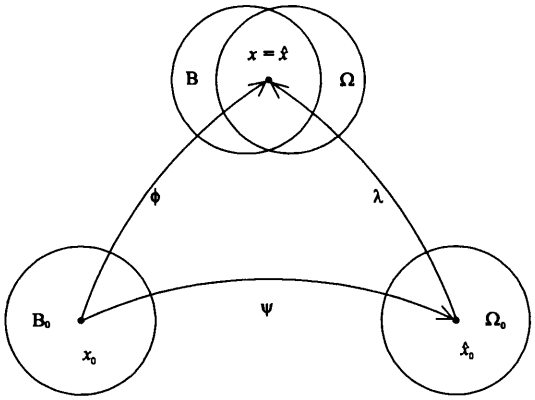

Figure 3.1: Mappings between the different regions of the moving reference frame.

It may then be written that

$$\mathbf{x} = \phi(\mathbf{x}_0, t) = \lambda(\hat{\mathbf{x}}_0, t) = \lambda(\psi(\mathbf{x}_0, t), t) = \hat{\mathbf{x}}. \tag{3.3}$$

Now it is possible to define an expression for the velocity ($\mathbf{u}$) of a material particle ($\mathbf{x}_0$) passing through a position ($\hat{\mathbf{x}}$) at time (t), known as *the material time derivative* of $\mathbf{u}$, by first differentiating equation (3.3) with respect to time and a constant material reference point $\mathbf{x}_0$ which gives

$$\frac{\partial \phi(\mathbf{x}_0, t)}{\partial t} = \frac{\partial \lambda(\hat{\mathbf{x}}_0, t)}{\partial t} + \frac{\partial \lambda(\hat{\mathbf{x}}_0, t)}{\partial \hat{\mathbf{x}}_0} \frac{\partial \psi(\mathbf{x}_0, t)}{\partial t} \tag{3.4}$$

From here we can see that the LHS of equation (3.4) is an expression for the current velocity $\mathbf{u}$ of material particle $\mathbf{x}_0$, and the first term of the RHS is an expression for the current velocity $\hat{\mathbf{v}}$ of reference point $\hat{\mathbf{x}}_0$, which allows us to rearrange this equation to the form

$$\frac{\partial \lambda(\hat{\mathbf{x}}_0, t)}{\partial \hat{\mathbf{x}}_0} \frac{\partial \psi(\mathbf{x}_0, t)}{\partial t} = \mathbf{u} - \hat{\mathbf{v}} \tag{3.5}$$

It should be noted that $\mathbf{u}$ may be given in terms of $\hat{\mathbf{x}}_0$ or $\hat{\mathbf{x}}$.

$$\mathbf{u} = \hat{\mathbf{u}}(\hat{\mathbf{x}}_0, t) = \tilde{\mathbf{u}}(\hat{\mathbf{x}}, t) \tag{3.6}$$

From this, we may formulate an expression for the material time derivative of $\mathbf{u}$ as

$$\frac{D\mathbf{u}}{Dt} = \frac{\partial \hat{\mathbf{u}}(\hat{\mathbf{x}}_0, t)}{\partial \hat{\mathbf{x}}_0} \frac{\partial \psi(\mathbf{x}_0, t)}{\partial t} + \frac{\partial \tilde{\mathbf{u}}(\hat{\mathbf{x}}_0, t)}{\partial t} \tag{3.7}$$

$$= \frac{\partial \tilde{\mathbf{u}}(\hat{\mathbf{x}}, t)}{\partial \hat{\mathbf{x}}} \frac{\partial \lambda(\hat{\mathbf{x}}_0, t)}{\partial \hat{\mathbf{x}}_0} \frac{\partial \psi(\mathbf{x}_0, t)}{\partial t} + \frac{\partial \hat{\mathbf{u}}(\hat{\mathbf{x}}_0, t)}{\partial t}. \tag{3.8}$$

Now, by inserting equation (3.5) into equation (3.8) and defining $\dot{\mathbf{u}} = \dfrac{\partial \mathbf{u}(\hat{\mathbf{x}}_0, t)}{\partial t}$ one obtains

$$\frac{D\mathbf{u}}{Dt} = \nabla_{\hat{\mathbf{x}}} \mathbf{u}(\mathbf{u} - \hat{\mathbf{v}}) + \dot{\mathbf{u}}, \tag{3.9}$$

known as *the fundamental Arbitrary Lagrangian-Eulerian Equation* (ALE). Note that $\nabla_{\hat{\mathbf{x}}}(\bullet)$ denotes the derivatives to the current referential coordinates $\hat{\mathbf{x}}$. Throughout this work, $\nabla(\bullet)$ without a subscript refers to the derivatives with respect to the coordinates of the domain the expression is formulated within. For cases where this may be ambiguous, subscripts will be used.

In equation (3.9) $\dot{\mathbf{u}}$ refers to the change of material particle velocity relative to the referential coordinate $\hat{\mathbf{x}}_0$.

The term ALE stems from the combination of:

- *Lagrangian* refers to the condition of the reference frame being fixed to the fluid particles, i.e. $\mathbf{u} = \hat{\mathbf{v}}$, causing the convective velocity term $(\mathbf{u} - \hat{\mathbf{v}})$ to be zero, resulting in the relation

$$\frac{D\mathbf{u}}{Dt} = \dot{\mathbf{u}}, \tag{3.10}$$

  which is the basis of Lagrangian solid mechanics.

- *Eulerian* refers to the condition of having a reference frame fixed in space, i.e. $\hat{\mathbf{v}} = 0$, resulting in the relation

$$\frac{D\mathbf{u}}{Dt} = (\nabla_{\hat{\mathbf{x}}}\mathbf{u})\mathbf{u} + \dot{\mathbf{u}}, \tag{3.11}$$

  which is employed in standard Eulerian fluid flow analyses. For more information on coordinate mapping and the derivation of the fundamental ALE equation see *e.g.* [61, 25, 56, 7, 4].

3.2.2 Formulation of Governing Equations

Conservation of mass: Consider an arbitrary subregion Ω' within Ω, consisting of a fixed set of reference points and filled with fluid. Given the assumed incompressibility of the fluid, the principle of conservation of mass states that the volume of fluid particles leaving or entering Ω' must equal the change in volume of Ω'. This can be expressed as

$$\int_{\Gamma'} (\mathbf{u} - \hat{\mathbf{v}}) \cdot \hat{\mathbf{n}}\, da = \int_{\Gamma'} -\hat{\mathbf{v}} \cdot \hat{\mathbf{n}}\, da, \tag{3.12}$$

where Γ' represents the boundary of Ω', and the vector $\hat{\mathbf{n}}$ represents the outward normal unit vector of Γ'. By applying the divergence theorem to this we obtain

$$\int_{\Omega'} \nabla \cdot \mathbf{u}\, dv = 0. \tag{3.13}$$

Since conservation of mass applies to any Ω' at any time $t \in I$, the local form of the mass conservation law is obtained as

$$\nabla \cdot \mathbf{u} = 0, \quad \forall (\hat{\mathbf{x}}, t) \in \Omega \times I, \tag{3.14}$$

where $I = [0, T_{end}]$ denotes the time interval of interest. This relation may be referred to as *the continuity equation.*

Conservation of Momentum: To apply the law of conservation of momentum we must first consider the forces acting on the fluid particles within Ω' at time $t \in I$. Namely, the body forces as a function of mass, and the surface forces acting on the boundary Γ' resulting from the fluid internal stress. Newton's second law balances these forces with the fluid intertia, resulting in the relation

$$\int_{\Omega'} \rho \mathbf{f} \, dv + \int_{\Gamma'} \boldsymbol{\sigma} \hat{\mathbf{n}} \, da = \int_{\Omega'} \rho (\nabla \mathbf{u} (\mathbf{u} - \hat{\mathbf{v}}) + \dot{\mathbf{u}}) \, dv, \tag{3.15}$$

where $\boldsymbol{\sigma}$ is the Cauchy stress tensor, $\mathbf{f}$ the body force vector per unit mass and ρ the scalar fluid density. The application of the divergence theorem on the second integral renders the entire relation in terms of the volume of any region Ω', resulting in the local form of the conservation of momentum,

$$\rho (\nabla \mathbf{u} (\mathbf{u} - \hat{\mathbf{v}}) + \dot{\mathbf{u}} - \mathbf{f}) - \nabla \cdot \boldsymbol{\sigma} = 0, \quad \forall (\hat{\mathbf{x}}, t) \in \Omega \times I. \tag{3.16}$$

The equations (3.14) and (3.16), along with the constitutive equation for Newtonion fluids

$$\boldsymbol{\sigma} = -pI + 2\mu \nabla^s \mathbf{u}, \tag{3.17}$$

are commonly referred to as *the Navier-Stokes equations for incompressible fluid flow.* Here p denotes pressure, I the identity tensor, μ the fluid viscosity, and $\nabla^s(\bullet)$ represents the symmetric part of the gradient, *i.e.* $\nabla^s \mathbf{u} = \frac{1}{2}(\nabla \mathbf{u} + \nabla^T \mathbf{u})$.

3.2.3 Flow Behavior and Incompressibility

Flow Behavior: The behavior of fluid flow may be simplified into the categories of *Laminar* and *Turbulent* flow based on the ratio of inertial forces to the fluid viscosity,

$$Re = \frac{\rho U_\infty D}{\mu} \tag{3.18}$$

known as the *Reynolds number* , where ρ, U_∞, and μ denote the fluid density, flow velocity, and viscosity respectively, and D the characteristic length.

Turbulent flow behavior generally consists of high frequency vortex shedding and fluid rotation in such a way as for the movement of fluid particles to appear chaotic. Fluid flow will generally be considered turbulent when the Reynolds number describing the flow is above a certain critical value specific to the system being considered; however, this value is generally of the order $Re_{cr} \approx 10^3$. While the formulation of a suitable approach to the numerical modelling of turbulent flow continues to be an area of intense focus, a detailed review of which is provided by Ferziger and Perić [26] , the focus of the examples analyzed in this work is instead on laminar flow which occurs at Reynolds numbers lower than those of turbulent flow and thus $Re < Re_{cr} \approx 10^3$ is observed throughout.

Incompressibility: Real fluids are compressible, however the degree of compressibility may be considered negligible under specific circumstances. In general, a fluid may be regarded as incompressible if the ratio of characteristic flow velocity to the speed of sound in the fluid, known as *the Mach number* , is of the value $Ma = \frac{U_\infty}{c} < 0.3$. Due to the fact that this condition is satisfied by most naturally occurring examples of fluid flow, in particular those of natural wind flows interacting with civil engineering structures, all fluid flow modelled in this work is considered incompressible.

3.2.4 Introduction to Boundary Conditions and Time Integration

In the interest of computing the fluid flow within Ω_f for all times $t \in I$, steps towards the solution may begin at such points where some or all components of the fluid flow are known. These regions of the domain generally occur at the internal and external boundaries, and may be described as detailed in this section.

- *Inlet boundary condition* Γ_{in}: At the inlet to the fluid domain the velocity terms of the flow are generally known due to the application of a prescribed value, and as such Γ_{in} may be described as

$$\mathbf{u} - \mathbf{u_{in}} = \mathbf{0} \quad \forall(\hat{\mathbf{x}}, t) \in \Gamma_{in} \times I. \tag{3.19}$$

- *Outlet boundary condition* Γ_{out}: At the outlet to the fluid domain the velocity terms of the flow are generally unknown, however the traction forces may be set to $\mathbf{0}$. It must also be noted that for the solution to be formed to satisfaction, at least a single point in Ω_f must be fixed in pressure, and this point is generally chosen at the centre of the outlet $\hat{\mathbf{x}}_{\mathbf{co}}$. Therefore, Γ_{out} may be described by

$$\begin{aligned} \boldsymbol{\sigma}\hat{\mathbf{n}} &= \mathbf{0} \quad \forall(\hat{\mathbf{x}}, t) \in \Gamma_{out} \times I, \\ p &= 0 \quad \text{for} \quad (\hat{\mathbf{x}}_{\mathbf{co}}, t) \in \Gamma_{out} \times I. \end{aligned} \tag{3.20}$$

- *Slip boundary condition* Γ_{slip}: Throughout this work slip boundary conditions are generally employed to describe the outer fluid domain boundaries running parallel to the direction of the flow. This boundary condition is such that the flow velocity components normal to the boundary are fixed at $\mathbf{0}$, while all tangential terms are free, *i.e.*

$$\mathbf{u} \cdot \hat{\mathbf{n}} = \mathbf{0}, \quad (\boldsymbol{\sigma}\hat{\mathbf{n}}) \cdot \hat{\mathbf{m}} = \mathbf{0} \quad \forall(\hat{\mathbf{x}}, t) \in \Gamma_{slip} \times I, \tag{3.21}$$

  with $\hat{\mathbf{n}}$ and $\hat{\mathbf{m}}$ representing the normal and tangential unit vectors of Γ_{slip}.

- *No-slip boundary condition* $\Gamma_{no-slip}$: Similar to the slip boundary condition, $\Gamma_{no-slip}$ fixes the velocity terms normal to the boundary at $\mathbf{0}$, however all other velocity terms at the boundary are also fixed, resulting in the description

$$\mathbf{u} = \mathbf{0} \quad \forall(\hat{\mathbf{x}}, t) \in \Gamma_{no-slip} \times I. \tag{3.22}$$

- *Fluid-solid interface* Γ_{f-s}: Similar to the static boundary conditions detailed above, it is possible to describe the interface of the fluid and solid domains by slip and no-slip conditions. Due to the primary focus of this work being the numerical modelling of fluid-structure interactions at low Reynold's numbers, which are primarily driven by vortex shedding, no-slip conditions are employed throughout due to being more

accurate in approximating the physics involved. It is also necessary when describing this boundary to account for the geometrical response of the interface resulting from the displacement and deformation of the solid domain, thus the no-slip condition may be described by

$$\mathbf{u} = \dot{\mathbf{d}} \quad \forall(\hat{\mathbf{x}}, t) \in \Gamma_{f-s} \times I, \tag{3.23}$$

where $\mathbf{d}$ is a vector describing the displacement of the solid domain. Additionally, the normal component of the reference frame velocity $\hat{\mathbf{v}}$ must equal the normal component of the fluid velocity $\mathbf{u}$ along the boundary, thus

$$(\mathbf{u} - \hat{\mathbf{v}}) \cdot \hat{\mathbf{n}} = \mathbf{0} \quad \forall(\hat{\mathbf{x}}, t) \in \Gamma_{f-s} \times I \tag{3.24}$$

must be satisfied for all $t \in I$. In the application of Γ_{f-s} detailed in section 5.2, this is done by setting $\hat{\mathbf{v}} = \mathbf{u}$. Finally, the equilibrium of stresses in the interface may be described by

$$(\boldsymbol{\sigma}\hat{\mathbf{n}})_f = -(\boldsymbol{\sigma}\hat{\mathbf{n}})_s \quad \forall(\hat{\mathbf{x}}, t) \in \Gamma_{f-s} \times I, \tag{3.25}$$

where $(\boldsymbol{\sigma}\hat{\mathbf{n}})_f$ and $(\boldsymbol{\sigma}\hat{\mathbf{n}})_s$ indicate the traction forces exerted on the interface by the fluid and solid respectively.

- *Free surface boundary condition* Γ_{free}: Though not employed within this work, it must be mentioned that when simulating fluid flow it may at times be necessary to describe boundary conditions associated with a free surface of the fluid body. This set of conditions requires the detailing of such terms as the surface tension of the fluid body and the geometrical displacement of the boundary. A detailed description of the formation and application of this boundary condition may be found in the works presented by Dettmer [16].

3.3 Mechanics of Flexible Solids

Due to the Lagrangian manner in which the kinematics of flexible solids is commonly described it is unnecessary to formulate a moving reference frame as was done in section

3.2.1. The configuration of the solid body is therefore directly represented by the computational domain Ω_s, with the current position of the solid particles being represented by $\mathbf{x} = \mathbf{x_0} + \mathbf{d}$, where $\mathbf{x_0}$ represents the initial set of solid coordinates at $t = 0$, and the vector $\mathbf{d}$ represents the solid displacement by $\mathbf{d} = \hat{\mathbf{d}}(\mathbf{x_0}, t)$. The material velocity and acceleration are therefore obtained as

$$\begin{aligned} \frac{\partial \hat{\mathbf{d}}(\mathbf{x_0}, t)}{\partial t} &= \dot{\mathbf{d}}, \\ \frac{D^2\mathbf{d}}{Dt^2} = \frac{\partial^2 \hat{\mathbf{d}}(\mathbf{x_0}, t)}{\partial t^2} &= \ddot{\mathbf{d}}, \end{aligned} \tag{3.26}$$

in a similar fashion to obtaining $\dot{\mathbf{u}}$ in equation (3.10).

Conservation of Momentum: Applying the law of conservation of momentum to the system results in the expression

$$\rho(\ddot{\mathbf{d}} - \mathbf{f}) - \nabla \cdot \boldsymbol{\sigma} = \mathbf{0} \quad \forall (\mathbf{x}, t) \in \Omega_s \times I. \tag{3.27}$$

Note that in this study solid elements may experience volumetric deformation, and therefore adjustments must be made to equation (3.27) to account for the separate densities of the undeformed (ρ_0) and deformed (ρ) solid elements. Bonet and Wood [6] account for this volumetric deformation by rearranging (3.27) in terms of the initial configuration $\Omega_{s,0}$ and modifying the stress term accordingly. It can therefore be noted that for small displacements $\mathbf{d}$, Ω_s may be approximated by $\Omega_{s,0}$, enabling the application of classical small strain analysis.

Application of Material Properties: Throughout this work, all solid materials are assumed to exibit *Neo-Hookean elastic* behavior. The constitutive equation employed is therefore

$$\boldsymbol{\sigma} = GJ^{-\frac{5}{3}}(\mathbf{B} - \frac{1}{3}\mathrm{tr}(\mathbf{B})\mathbf{I}) + K\frac{J^2 - 1}{2J}\mathbf{I}, \tag{3.28}$$

where the scalars G and K represent the solid shear and bulk moduli, $\mathbf{B}$ the *left Caughy-Green tensor* , and the scalar J the determinant of the deformation gradient $\mathbf{F}$, related to $\mathbf{B}$ by

$$\mathbf{B} = \mathbf{F}\mathbf{F}^T, \qquad J = \det(\mathbf{F}),$$

where

$$\mathbf{F} = \frac{\partial \mathbf{x}}{\partial \mathbf{x}_0} = \mathbf{I} + \frac{\partial \mathbf{d}}{\partial \mathbf{x}_0}. \tag{3.29}$$

For small strain elasticity, equation (3.28) may be reduced to

$$\boldsymbol{\sigma} = 2G(\nabla^s \mathbf{d} - \frac{1}{3}(\nabla \cdot \mathbf{d})\mathbf{I}) + K(\nabla \cdot \mathbf{d})\mathbf{I}. \tag{3.30}$$

3.3.1 Solid Boundary Conditions

Similar to the boundary conditions of Ω_f described in section 3.2.4, the boundary of Ω_s may be described using the following conditions:

- *Fixed boundary condition* Γ_{fixed}: used to represent a boundary joined to a support resulting in displacement being fixed in one or more axes, Γ_{fixed} may be described by

$$\mathbf{d} = \mathbf{0} \quad \forall (\mathbf{x}, t) \in \Gamma_{fixed} \times I. \tag{3.31}$$

- *Free boundary condition* Γ_{free}: this condition is applied throughout this work to describe any boundary of Ω_s not fixed to a support, and thus allowed to deform

$$\boldsymbol{\sigma}\mathbf{n} = \mathbf{0} \quad \forall (\mathbf{x}, t) \in \Gamma_{free} \times I. \tag{3.32}$$

- *Fluid-solid interface* Γ_{f-s}: being directly related to the Ω_f boundary described in equations (3.23) and (3.25), this boundary condition is described by

$$\dot{\mathbf{d}} = \mathbf{u}, \quad (\boldsymbol{\sigma}\mathbf{n})_s = -(\boldsymbol{\sigma}\hat{\mathbf{n}})_f \quad \forall (\mathbf{x}, t) \in \Gamma_{f-s} \times I. \tag{3.33}$$

- *Symmetry Boundary Condition* Γ_{sym}: While this boundary condition is not implemented in this work, it must be mentioned that in the case of an axisymmetric model

problem, computational cost may be reduced by applying Γ_{sym} along the axis of symmetry and omitting the symmetrical duplicate components of the model. Similar to the boundary condition described in equation (3.21), Γ_{sym} may be described by

$$(\boldsymbol{\sigma}\mathbf{n}) \cdot \mathbf{m} = 0, \quad \mathbf{d} \cdot \mathbf{n} = 0 \quad \forall (\mathbf{x}, t) \in \Gamma_{sym} \times I, \tag{3.34}$$

where $\mathbf{n}$ and $\mathbf{m}$ describe the unit vectors normal and tangential to the boundary respectively.

Chapter 4

Introduction to Finite Element Modelling

4.1 Solution Procedure

In the decades since the finite element method was first applied in the context of computer-aided engineering, a wide variety of techniques for its application have been developed. Each of these applications, however, follows a common general method consisting of:

- The subdivision of a complex system into smaller regions known as *finite elements* .
- The approximation to solution values of the complex governing equations being applied over each element, the sum of which form an approximate solution to the entire domain.
- The application of constraints to these approximations, designed to restrict the error of approximation to within acceptable levels.

In this chapter, the methods for the application of the finite element method to linear and non-linear governing equations employed within this work are described. Further information on the general formation of the finite element method may be found in text books such as, *e.g.* [32, 1, 62, 14, 11].

4.1.1 Forming an Approximate Solution: The Weak Form and The Classical Galerkin Method

Consider a set of governing equations, such that they may be described by

$$\mathcal{L}(u) = -f \quad \forall \mathbf{x} \in \Omega, \tag{4.1}$$

where $\mathcal{L}(\cdot)$ describes the linear differential operator, u the unknown dependent variable, and Ω the domain of the system. Arranging the equation in this manner is generally known as *the Strong Form* of the differential equation. The boundary of the domain of this system, Γ, may also be described by

$$u - g = 0 \quad \forall \mathbf{x} \in \Gamma_g \tag{4.2}$$

$$\mathbf{q}(u) \cdot \mathbf{n} - t = 0 \quad \forall \mathbf{x} \in \Gamma_t, \tag{4.3}$$

where $\mathbf{n}$ denotes the outward normal unit vector to the boundary Γ, the flux $\mathbf{q}(u)$ is a linear function of the first derivatives of u, and the conditions Γ_g and Γ_t describe the boundary such that $\Gamma = \Gamma_g \cup \Gamma_t$. By directly assigning a value to the unknown variable u, equation (4.2) describes a *Dirichlet boundary condition* . Likewise, by assigning a value to the derivatives of u, equation (4.3) describes a *Neumann boundary condition.*

In the interest of forming an approximate solution to this set of governing equations, it is possible to lower the order of the highest derivatives through first multiplying with an admissible virtual perturbation ω, known as a *test* or *weighting* function, and then integrating over the domain Ω. If we consider the set of values $H^1(\Omega)$ such that $u \in H^1(\Omega)$ then we may consider all $\omega \in \{\omega \in H^1(\Omega) \quad | \quad \omega = 0 \quad \forall \mathbf{x} \in \Gamma_g\}$ as admissible. Integrating this system by parts results in the *Weak Form* of the governing equation

$$a(\omega, u) = F(\omega), \tag{4.4}$$

where $a(\omega, u)$ and $F(\omega)$ represent a bilinear and linear form on Ω. The exact solution u of the strong form will satisfy the weak form for all admissible test function ω. The advantage of rewriting the equations in the weak form is that if we consider the space

$\mathcal{W} = \left\{\omega \in H^1(\Omega) | \omega_{|\Gamma_g} = 0\right\}$ and define $\mathcal{W}^h \subset \mathcal{W}$ as a finite dimensional subspace of $\mathcal{W}$, it can be shown that there exist solutions u^h in $\mathcal{W}^h \subset \mathcal{W}$ where $u \notin \mathcal{W}^h$, if $u \in \mathcal{W}^h$ simply means that $u = u^h$. By contrast, the strong form of the equation can only be satisfied by the exact solution u. This relaxation of constraints in the weak form creates the basis for the formation of an approximate solution. By establishing the relationship between the solutions $u^h \in \mathcal{W}^h$ and $u \in \mathcal{W}$ it can be shown that $u^h \to u$ as $\mathcal{W}^h \to \mathcal{W}$.

This process of obtaining an approximate solution $u^h \in \mathcal{W}^h$ such that

$$a(\omega^h, u^h) = F(\omega^h) \quad \forall \omega^h \in \mathcal{W}^h \tag{4.5}$$

is known as the *Classical Galerkin* or *Bubnov-Galerkin* method. It should be noted that this method satisfies the Dirichlet boundary condition exactly, however the Neumann boundary condition is only weakly satisfied. A detailed description of the mathematical foundation behind the Galerkin method may be found in, *e.g.* [49, 8, 13, 54].

4.1.2 Isoparametric Finite Elements

In the previous section it was shown that the classical Galerkin method may be employed to form an approximate solution u^h over a finite dimensional space $\mathcal{W}^h$. This section details how the *standard finite element method* uses this in a way that may be solved computationally.

The finite spaces $\mathcal{W}^h$ used to approximate Ω are commonly defined as spaces of continuous piecewise polynomials such that $\Omega = \cup \, _{e=1}^{n_{el}} \, \Omega^e$ describes the decomposition of domain Ω into n_{el} subdomains, known as *finite elements* , Ω^e. These finite elements consist of geometric shapes defined by *nodes* at the corners joined together by the *node connectivity* . Typically, in two dimensions these shapes are squares or triangles, and in three dimensions they are quadrilaterals or tetrahedrals. $\mathcal{W}^h$ may therefore be described by

$$\mathcal{W}^h = \left\{\omega^h \in H^1(\Omega) | \omega^h|_{x^h \in \Omega^e} \in P_k(\Omega^e), \quad \omega^h|_{x^h \in \Gamma_g} = 0\right\} \tag{4.6}$$

where $P_k(\Omega^e)$ denotes a space of polynomials of order k on domain Ω^e.

In order to interpolate the values of the approximate solution u^h over the domain of

each finite element Ω^e, a distribution of the nodal solution values is applied across the intermediate spaces. These distributions are known as *shape functions* and are commonly represented by $N_i(\xi_j)$ where $[i, j = 1, 2, ..., n_{node}]$ denotes which node the shape function and parametric coordinate system ξ refer to in such a way as $N_i(\xi_j) = 1$ for $i = j$ and 0 for $i \neq j$. The *finite element mesh* consists of finite elements connected together such that they share common nodes along their connected edges. The combination of all element shape functions N_i referring to a single node i allows the construction of a *global shape function* N_i^g. The set of all global shape functions forms the nodal representation of $\mathcal{W}^h$, with the number of nodes (excluding those on Γ_g) defining the dimension of $\mathcal{W}^h$. Any function $\omega^h \in \mathcal{W}^h$ may therefore be written as

$$\omega^h = \sum_{e=1}^{n_{el}} N_i^g(\boldsymbol{\xi}) \mathrm{w}_i \tag{4.7}$$

where w_i represents the value of ω^h at node i. Further information on the construction of finite element discretisations may be found in the previously mentioned [1, 62, 11, 49, 8].

4.2 Finite Elements in Solid Mechanics

In this section, an introduction to the application of the finite element method in solid mechanics is detailed. It must be noted that the computational framework employed in this work does not impose limitations on which solid finite elements may be used. As such, this section will provide a general introduction to solid discretisation as well as examples of some solid finite elements.

4.2.1 Linear Elasticity

As detailed in section 4.1.1 the governing equation of linear elastic behavior may be written as

$$\mathcal{L}(\mathbf{u}) = \nabla \cdot \boldsymbol{\sigma}(\mathbf{u}) = -\mathbf{f} \quad \forall \mathbf{x} \in \Omega \tag{4.8}$$

$$\boldsymbol{\sigma}(\mathbf{u}) = \Lambda(\nabla \cdot \mathbf{u})\mathbf{I} + 2\mu\nabla^s\mathbf{u} \tag{4.9}$$

$$\mathbf{u} - \mathbf{g} = \mathbf{0} \quad \forall \mathbf{x} \in \Gamma_\mathbf{g} \tag{4.10}$$

$$\boldsymbol{\sigma}(\mathbf{u})\mathbf{n} - \mathbf{t} = \mathbf{0} \quad \forall \mathbf{x} \in \Gamma_\mathbf{t} \tag{4.11}$$

where $\boldsymbol{\sigma}$ is a second order tensor introduced as a linear function of the displacement vector field $\mathbf{u}$. The scalars Λ and μ represent the Lamé constants, $\mathbf{f}$ the body forces and $\mathbf{t}$ the prescribed boundary traction forces. Applying a weighting function to obtain the weak form of the linear elastic governing equations is known as *the principle of virtual work* and results in the equation

$$\int_\Omega \nabla\boldsymbol{\omega} : \boldsymbol{\sigma}(\mathbf{u})\, dv = \int_{\Gamma_t} \boldsymbol{\omega} \cdot \mathbf{t}\, da + \int_\Omega \boldsymbol{\omega} \cdot \mathbf{f}\, dv \tag{4.12}$$

with

$$\int_\Omega \nabla\boldsymbol{\omega} : \boldsymbol{\sigma}(\mathbf{u})\, dv = \int_\Omega \Lambda(\nabla \cdot \mathbf{u}) + 2\mu\nabla\boldsymbol{\omega} : \nabla^s\mathbf{u}\, dv. \tag{4.13}$$

These expressions may then be rewritten in the form $a(\omega, u) = F(\omega)$ as will be detailed in the next section.

Example: Continuum Elements

In two dimensions, this work represents continuum elements with nine-noded fully integrated finite elements. For use in three dimensions these may be extrapolated to form twenty-noded quadratic elements. Due to the tendency of continuum elements to exhibit volumetric locking near the incompressibility limit, their application in this work is restricted to very slender structures. For all other solid structures in this work, eight-noded linear brick elements with suitable modifications to account for incompressible deformation are employed.

The local form of equilibrium excluding body forces may be represented by

$$\rho\ddot{\mathbf{d}} - \nabla \cdot \boldsymbol{\sigma} = 0 \quad \forall (\mathbf{x}, t) \in \Omega \times I \tag{4.14}$$

where Ω denotes the current configuration of the solid domain and $\mathbf{d}$ the displacement vector field. Assuming pure Neumann Γ_t and Dirichlet $\Gamma_\mathbf{g}$ boundary conditions, the weak form of this equation may be written as

$$\int_\Omega \rho\ddot{\mathbf{d}} \cdot \boldsymbol{\omega}\, dv + \int_\Omega \boldsymbol{\sigma} : \nabla\boldsymbol{\omega}\, dv = \int_{\Gamma_t} \mathbf{t} \cdot \boldsymbol{\omega}\, da. \tag{4.15}$$

For small strains and deformations it is possible to integrate this equation over the initial configuration of Ω, and assume the relation

$$\boldsymbol{\sigma} = 2\mu\left(\nabla^s\mathbf{d} - \frac{1}{3}(\nabla\cdot\mathbf{d})\mathbf{I}\right) + K(\nabla\cdot\mathbf{d})\mathbf{I} \tag{4.16}$$

where μ and K represent the shear and bulk moduli of the solid. Discretising the vector fields $\mathbf{d}$ and $\boldsymbol{\omega}$ over each element results in the equations

$$\mathbf{d}^h = N_i\mathbf{d}_i, \quad \boldsymbol{\omega}^h = N_j\mathbf{w}_j, \quad i,j = 1,2,...,n_{node} \tag{4.17}$$

where the shape functions N_i, N_j are specific to the element type. Using these equations to discretise the weak form in equation (4.15) with arbitrary virtual displacements gives rise to the matrix equation

$$\mathbf{M}\ddot{\mathbf{d}} + \mathbf{K}\mathbf{d} = \mathbf{P} \tag{4.18}$$

where the *stiffness matrix* $\mathbf{K}$, *external force vector* $\mathbf{P}$ and *mass matrix* $\mathbf{M}$ are formed by the assembly of elemental contributing factors $\mathbf{k}^e$, $\mathbf{p}^e$ and $\mathbf{m}^e$ respectively. This may be expressed by

$$\mathbf{K} = \mathbf{A}_{e=1}^{n_e}\mathbf{k}^e, \quad \mathbf{k}_{ij}^e = \int_{\Omega^e} \Lambda\nabla N_i \otimes \nabla N_j + \mu(\nabla N_i \cdot N_j\mathbf{I} + \nabla N_j \otimes \nabla N_i)\, dv \tag{4.19}$$

$$\mathbf{P} = \mathbf{A}_{e=1}^{n_e}\mathbf{p}^e, \quad \mathbf{p}_i^e = \int_{\Gamma_t\cap\Gamma_g} N_i\mathbf{t}\, da + \int_{\Omega^e} N_i\mathbf{f}\, dv \tag{4.20}$$

$$\mathbf{M} = \mathbf{A}_{e=1}^{n_e}\mathbf{m}^e, \quad \mathbf{m}_{ij}^e = \int_{\Omega^e} \rho N_i N_j\mathbf{I}\, dv \tag{4.21}$$

In order to model large strains and displacements which require taking geometrical deformation into account, this work employs the Neo-Hooke elastic material model. As such, the Cauchy stress tensor employed is

$$\boldsymbol{\sigma} = \mu J^{\frac{5}{3}} \left(\mathbf{B} - \frac{1}{3} \mathrm{tr}\,(\mathbf{B})\, \mathbf{I} \right) + K \frac{J^2 - 1}{2J} \mathbf{I}. \tag{4.22}$$

By integrating the weak form over the current spacial domain Ω and discretising the elemental domains as done with small strains, the complete matrix equation for large strains is obtained as

$$\mathbf{M}\ddot{\mathbf{d}} + \mathbf{F}(\mathbf{d}) = \mathbf{P} \tag{4.23}$$

where $\mathbf{F}(\mathbf{d})$ represents the nodal internal force vector which is nonlinear in terms of the displacements $\mathbf{d}$. It must be noted that whether the weak form is discretised with respect to the initial ($\mathbf{x}_0$) or material ($\mathbf{x}$) coordinate systems, the finite element assembly results in the same matrix equation (4.23). Once the matrix equation has been assembled, the application of a time discretisation method allows for the formation of the approximate solution via an appropriate numerical iteration scheme. In this work the *Generalised-α method* is employed for time discretisation in both solid and fluid domains. A detailed description of this method is provided in section 4.3.2.

Additional information on the finite element modelling of elastic continua at small and large strains may be found in such texts as *e.g.* [6, 32, 1, 62, 14, 15].

4.3 Finite Elements in Fluid Mechanics

In order to introduce the formulation of the weak form of the incompressible Navier-Stokes equations in a simple manner, this section will focus on steady state flow over fixed domains. The extension of this method to unsteady flow over moving domains will be covered in Chapter 5. For fixed domains, $\hat{\mathbf{v}} = \mathbf{0}\ \forall (\hat{\mathbf{x}}, t) \in \Omega \times I$, which results in the Navier-Stokes equations (3.14)-(3.17) with standard Neumann and Dirichlet boundary conditions being reduced to

$$\rho((\nabla \mathbf{u})\mathbf{u} - \mathbf{f}) - \nabla \cdot \boldsymbol{\sigma} = \mathbf{0} \quad \forall \quad \hat{\mathbf{x}} \in \Omega \tag{4.24}$$

$$\nabla \cdot \mathbf{u} = 0 \quad \forall \quad \hat{\mathbf{x}} \in \Omega \tag{4.25}$$

$$\mathbf{u} - \mathbf{g} = \mathbf{0} \quad \forall \quad \hat{\mathbf{x}} \in \Gamma_{\mathbf{g}} \tag{4.26}$$

$$\boldsymbol{\sigma}\mathbf{n} - \mathbf{t} = \mathbf{0} \quad \forall \quad \hat{\mathbf{x}} \in \Gamma_{\mathbf{t}} \tag{4.27}$$

with

$$\boldsymbol{\sigma} = -p\mathbf{I} + 2\mu\nabla^s\mathbf{u} \tag{4.28}$$

Applying virtual terms for velocity $\boldsymbol{\omega}$ and pressure q results in the weak form

$$\int_\Omega [\boldsymbol{\omega} \cdot \rho((\nabla \mathbf{u})\mathbf{u} - \mathbf{f}) - (\nabla \cdot \boldsymbol{\omega})p + 2\mu\nabla\boldsymbol{\omega} : \nabla^s\mathbf{u} + q(\nabla \cdot \mathbf{u})]\, dv - \int_{\Gamma_t} \boldsymbol{\omega} \cdot \mathbf{t}\, da = 0 \tag{4.29}$$

Using a standard Galerkin formulation results in the approximate solution: find $\mathbf{u}^h \in \mathcal{U}^h$ and $p^h \in \mathcal{P}^h$ such that for all $\boldsymbol{\omega}^h \in \mathcal{W}^h$ and $q^h \in \mathcal{P}^h$

$$\int_\Omega \left[\boldsymbol{\omega}^h \cdot \rho\left((\nabla \mathbf{u}^h)\mathbf{u}^h - \mathbf{f}\right) - (\nabla \cdot \boldsymbol{\omega}^h)p^h + 2\mu\nabla\boldsymbol{\omega}^h : \nabla^s\mathbf{u}^h + q^h(\nabla \cdot \mathbf{u}^h)\right] dv - \int_{\Gamma_t} \boldsymbol{\omega}^h \cdot \mathbf{t}^h\, da = 0 \tag{4.30}$$

with

$$\begin{aligned}
\mathcal{U}^h &= \left\{\mathbf{u}^h \in (H^1(\Omega))^{n_{sd}} | \mathbf{u}^h|_{\hat{\mathbf{x}}^h \in \Omega^e} \in (P_k(\Omega^e))^{n_{sd}}, \quad \mathbf{u}^h|_{\hat{\mathbf{x}}^h \in \Gamma_{\mathbf{g}}} = \mathbf{g}\right\} \\
\mathcal{W}^h &= \left\{\boldsymbol{\omega}^h \in (H^1(\Omega))^{n_{sd}} | \boldsymbol{\omega}^h|_{\hat{\mathbf{x}}^h \in \Omega^e} \in (P_k(\Omega^e))^{n_{sd}}, \quad \boldsymbol{\omega}^h|_{\hat{\mathbf{x}}^h \in \Gamma_{\mathbf{g}}} = \mathbf{0}\right\} \\
\mathcal{P}^h &= \left\{p^h \in (H^1(\Omega)) | p^h|_{\hat{\mathbf{x}}^h \in \Omega^e} \in (P_k(\Omega^e))\right\}
\end{aligned} \tag{4.31}$$

where $n_{sd} = 2, 3$ indicates the dimension of the space.

While the standard Galerkin method is generally adequate in modelling solid mechanics, equal order velocity-pressure Galerkin formulation has been shown to exhibit spurious oscillations in velocity and pressure and thus is not considered suitable for formulating the incompressible Navier-Stokes equations. Detailed investigation into the origin of these

instabilities may be found in Dettmer [16] and references therein. This work solves this issue with the implementation of the *streamline-upwind/* and *pressure-stabilising/Petrov-Galerkin methods* (SUPG/PSPG).

4.3.1 SUPG/PSPG Stabilisation Techniques

SUPG - Velocity Stabilisation

The simplest technique for stabilizing velocity is to add an artificial diffusion term μ_{art} to the existing physical diffusion μ. The ideal value of μ_{art} is dependent on the vector of local properties $\boldsymbol{\alpha}^e = \{|\mathbf{a}^e|, \mu, h^e\}$ where $\mathbf{a}^e$ is the local divergence free velocity field and h^e is the local characteristic length. Using this technique alone, however, may exhibit diffusion perpendicular to the streamlines known as *crosswind diffusion.* In order to prevent this undesirable behavior the artificial diffusion may be restricted to the direction $\mathbf{a}$ of the flow. This restricted artificial diffusion $\tau(\boldsymbol{\alpha}^e)$ may then be expressed in the finite element formulation as

$$\sum_{e=1}^{n_{el}} \int_{\Omega^e} \omega^h \mathbf{a} \cdot \nabla u^h + \mu \nabla \omega^h \cdot \nabla u^h + \tau(\boldsymbol{\alpha}^e)(\mathbf{a} \cdot \nabla \omega^h)(\mathbf{a} \cdot \nabla u^h)\, dv = 0, \tag{4.32}$$

known as the *streamline diffusion method.* It should be noted that $\tau(\boldsymbol{\alpha}^e)$ has the dimension of time and approaches zero as $h^e \to 0$. In the case of linear finite element interpolations this element formulation may be written as

$$\int_{\Omega} \omega^h \mathbf{a} \cdot \nabla u^h + \mu \nabla \omega^h \cdot \nabla u^h\, dv + \sum_{e=1}^{n_{el}} \int_{\Omega^e} \tau(\boldsymbol{\alpha}^e)(\mathbf{a} \cdot \nabla \omega^h)(\mathbf{a} \cdot \nabla u^h - \mu \Delta u^h)\, dv = 0. \tag{4.33}$$

This may also be written as

$$\sum_{e=1}^{n_{el}} \int_{\Omega^e} \widetilde{\omega}^h (\mathbf{a} \cdot \nabla u^h - \mu \Delta u^h)\, dv = 0, \tag{4.34}$$

where $\widetilde{\omega}^h$ is a modified weighting function defined as

$$\widetilde{\omega}^h = \omega^h + \tau(\boldsymbol{\alpha}^e)(\mathbf{a} \cdot \nabla \omega^h). \tag{4.35}$$

This application of different trial spaces $\omega^h \neq \tilde{\omega}^h$ is known as the *Petrov-Galerkin* method, resulting in equation (4.34) being identified as the *streamline-upwind/Petrov-Galerkin* (SUPG) method. It should be noted that the SUPG method defines the weighting functions ω^h, $\tilde{\omega}^h$ such that within an element the upstream nodes are weighted more heavily than the downstream nodes. Additionally, in order for equation (4.34) to agree with the strong form of the problem, the finite element interpolation is required to be quadratic or higher. In the case of linear finite element interpolation the SUPG method may be called *weakly consistent* .

Credit for being the first researchers to present the streamline diffusion method strictly in the format of a Petrov-Galerkin formulation goes to Brooks and Hughes [10]. Additional information on the fomulation and accuracy of the SUPG method has been presented by Johnson *et al* [36, 37].

PSPG - Pressure Stabilisation

Similar to the application of the SUPG method for velocity stabilisation, this work employs the *pressure-stabilised/Petrov-Galerkin* (PSPG) method for pressure stability. First introduced by Hughes *et al* [33] this method was based on work done by Brezzi and Pitkäranta [9], and Johnson and Saranen [38]. The PSPG method is defined as follows: Find $\mathbf{u}^h \in \mathcal{U}^h$ and $p^h \in \mathcal{P}^h$, such that for all $\boldsymbol{\omega}^h \in \mathcal{W}^h$ and $q^h \in \mathcal{P}^h$

$$\sum_{e=1}^{n_{el}} \int_{\Omega^e} \tilde{\boldsymbol{\omega}}^h \cdot (\nabla p^h \; - \; 2\mu \nabla \cdot \nabla^s \mathbf{u}^h) \; + \; q^h (\nabla \cdot \mathbf{u}^h) \, dv = 0, \tag{4.36}$$

where

$$\tilde{\boldsymbol{\omega}}^h = \boldsymbol{\omega}^h \; + \; \tau(h^e, \mu) \nabla q^h. \tag{4.37}$$

Using integration by parts results in equation (4.36) being rewritten as

$$\int_\Omega -(\nabla\cdot\boldsymbol{\omega}^h)p^h + 2\mu\nabla\boldsymbol{\omega}^h:\nabla^s\mathbf{u}^h + q^h(\nabla\cdot\mathbf{u}^h)\,dv + \sum_{e=1}^{n_{el}}\int_{\Omega^e}\tau(h^e,\mu)\nabla q^h\cdot(\nabla p^h - 2\mu\nabla\cdot\nabla^s\mathbf{u}^h)\,dv = 0, \tag{4.38}$$

which displays the PSPG method as a standard Galerkin formulation combined with an additional stabilisation term. In the case of piecewise linear interpolation the diffusion part of the second term of equation (4.38) disappears. The parameter τ would then be required to tend to zero as $h^e \to 0$ in order to remain consistent with the strong form of the problem. It should be noted that, similar to the SUPG method, linear finite element interpolation results in the PSPG method being *weakly consistent.* Additionally, a priori error estimate presented by Hughes *et al* [33] indicates that the method is stable, and achieves optimal convergence if $\tau(h,\mu)$ is of $\mathcal{O}(h^2)$.

SUPG/PSPG Formulation

Tezduyar *et al* [60] suggests the combination of both the SUPG and PSPG methods in order to obtain a stable finite element formulation of the incompressible steady state Navier-Stokes equations (3.14)-(3.17). This combination, referred to as the SUPG/PSPG method reads: Find $\mathbf{u}^h \in \mathcal{U}^h$ and $p^h \in \mathcal{P}^h$ such that for any $\boldsymbol{\omega}^h \in \mathcal{W}^h$ and $q^h \in \mathcal{P}^h$

$$\int_\Omega \Big[\boldsymbol{\omega}^h\cdot\rho\Big((\nabla\mathbf{u}^h)\mathbf{u}^h - \mathbf{f}\Big) - \Big(\nabla\cdot\boldsymbol{\omega}^h\Big)p^h + 2\mu\nabla\boldsymbol{\omega}^h:\nabla^s\mathbf{u}^h + (\nabla\cdot\mathbf{u}^h)q^h\Big]\,dv - \int_{\Gamma_t}\boldsymbol{\omega}^h\cdot\mathbf{t}^h\,da + \sum_{e=1}^{n_{el}}\int_{\Omega^e}\Big[\tau_{\mathbf{u}}\rho(\nabla\boldsymbol{\omega}^h)\mathbf{u}^h + \tau_p\nabla q^h\Big]\cdot\Big[\rho\Big((\nabla\mathbf{u}^h)\mathbf{u}^h - \mathbf{f}\Big) + \nabla p^h\Big]\,dv = 0, \tag{4.39}$$

where $\mathcal{U}^h$, $\mathcal{W}^h$ and $\mathcal{P}^h$ are identified by inserting $k=1$ to equation (4.31)

$$\begin{aligned}
\mathcal{U}^h &= \left\{ \mathbf{u}^h \in (H^1(\Omega))^{n_{sd}} | \mathbf{u}^h|_{\hat{\mathbf{x}}^h \in \Omega^e} \in (P_1(\Omega^e))^{n_{sd}}, \quad \mathbf{u}^h|_{\hat{\mathbf{x}}^h \in \Gamma_{\mathbf{g}}} = \mathbf{g} \right\} \\
\mathcal{W}^h &= \left\{ \boldsymbol{\omega}^h \in (H^1(\Omega))^{n_{sd}} | \boldsymbol{\omega}^h|_{\hat{\mathbf{x}}^h \in \Omega^e} \in (P_1(\Omega^e))^{n_{sd}}, \quad \boldsymbol{\omega}^h|_{\hat{\mathbf{x}}^h \in \Gamma_{\mathbf{g}}} = \mathbf{0} \right\} \\
\mathcal{P}^h &= \left\{ p^h \in (H^1(\Omega)) | p^h|_{\hat{\mathbf{x}}^h \in \Omega^e} \in (P_1(\Omega^e)) \right\}.
\end{aligned} \tag{4.40}$$

It should be mentioned that while there exist versions of (4.40) based on higher order polynomials (*i.e.* $k > 1$), they are not necessarily more efficient. As such in this work the focus is restricted to $k = 1$. It should also be noted that the employment of two stabilisation parameters $\tau_{\mathbf{u}}$ and τ_p allows the velocity (SUPG) and pressure (PSPG) stabilisations to be controlled independently. Due to both the convection term and the dependence of $\tau_{\mathbf{u}}$ and τ_p on $\mathbf{u}^h$ the SUPG/PSPG formulation is non-linear and thus requires the use of a numerical iteration scheme to solve for the nodal values.

While the numerical methods employed in this work are detailed in Chapter 6, the application of numerical iteration schemes to solve unsteady, incompressible flow is a subject of great academic interest. Publications on this subject include Dettmer and Perić [17, 18, 19, 20, 21, 23], Dettmer *et al* [24], Tezduyar *et al* [58, 59], Behr and Tezduyar [3], and Perić and Slijepčević [46, 55].

Stabilisation Parameters

The stabilisation parameters $\tau_{\mathbf{u}}$ and τ_p are both defined as

$$\tau = \frac{h^e}{2||\mathbf{u}^e||\rho}\xi, \quad \xi = \frac{\beta_1}{\sqrt{1 + \left(\frac{\beta_1}{\beta_2 Re^e}\right)^2}}, \quad Re^e = \frac{||\mathbf{u}^e|| h^e \rho}{2\mu}, \tag{4.41}$$

with different, independent scaling parameters β_1 and β_2, where h^e, $\mathbf{u}^e$ and Re^e represent the element characteristic size, the fluid velocity at the centroid of the element, and the element Reynolds number respectively. Throughout this work the values for β_1 and β_2 are as follows:

$$\begin{aligned}
\tau_{\mathbf{u}} &: \beta_1 = 1, \ \beta_2 = \frac{1}{3} \\
\tau_p &: \beta_1 = 30, \ \beta_2 = \frac{1}{10}.
\end{aligned} \tag{4.42}$$

Generally, the influence of β_1 and β_2 has been found to be small unless very large or very small values are chosen. The relatively large value of $\tau_p : \beta_1$ has been thought to be beneficial for very coarse meshes in a few cases. A detailed justification of the choice of stabilisation parameters employed may be found in Dettmer [16].

4.3.2 Time Integration Scheme: The Generalised-α Method

The Generalised-α Method is a discrete, single-step implicit time integration procedure that has been shown to possess both good accuracy and user controlled high-frequency damping. This method employs three variable time integration parameters (α_f, α_m, γ) which allows for a significant degree of flexibility when implemented in the solution algorithm. As such, this method was selected to discretise the numerical models employed throughout this work.

In this section an overview of the generalised-α method and its application in this work will be provided. Detailed justification for the method and proofs of its accuracy have been presented by Chung and Hulbert [12] and Jansen *et al* [35]. A comparison of the generalised-α method with other single-step implicit time integration methods in the context of unsteady flow governed by the Navier-Stokes equations has been presented by Dettmer and Perić [16, 17].

Overview

The generalised-α method is based on the relationships

$$u_{n+1} = u_n + \Delta t((1-\gamma)\dot{u}_n + \gamma\dot{u}_{n+1}) \tag{4.43}$$

$$u_{n+\alpha_f} = (1-\alpha_f)u_n + \alpha_f u_{n+1} \tag{4.44}$$

$$\dot{u}_{n+\alpha_m} = (1-\alpha_m)\dot{u}_n + \alpha_m\dot{u}_{n+1} \tag{4.45}$$

where u_n represents the value of the system solution u at time instant t_n such that $0 = t_0 < t_1 < ... < t_N = T_{end}$ is the partition of the time scale I to be considered. For example, consider the non-linear model problem

$$\dot{u}_n - \lambda(u_n)u_n = 0 \quad \forall t_n \in I \tag{4.46}$$

with known initial solution u_o. Applying the generalised-α method results in the discrete form

$$\dot{u}_{n+\alpha_m} - \lambda(u_{n+\alpha_f})u_{n+\alpha_f} = 0. \tag{4.47}$$

By rewriting equation (4.43) as

$$\dot{u}_{n+1} = \frac{1}{\gamma\Delta t}(u_{n+1} - u_n) - \frac{1-\gamma}{\gamma}\dot{u}_n \tag{4.48}$$

and inserting into (4.45), the expression

$$\dot{u}_{n+\alpha_m} = \left(1 - \frac{\alpha_m}{\gamma}\right)\dot{u}_n + \frac{\alpha_m}{\gamma\Delta t}(u_{n+1} - u_n) \tag{4.49}$$

is obtained. Equations (4.49) and (4.44) may then be inserted into (4.47), resulting in an equation with u_{n+1} as the only unknown.

$$r(u_{n+1}, u_n, \dot{u}_n) = 0 \tag{4.50}$$

Thus equations (4.50) and (4.48) may be used to compute the unknown solution values u_{n+1}, $\dot{u}_{n+1}$ for each time step. In summary, the computer implementation of the solution procedure is

1. Solve (4.50) and (4.48) for u_{n+1} and $\dot{u}_{n+1}$
2. $(u_n, \dot{u}_n) \longleftarrow (u_{n+1}, \dot{u}_{n+1})$
3. Goto 1.

Finally, it should be noted that the parameters α_f, α_m and γ have been shown to reduce to a single free integration parameter provided the conditions for second order accuracy and user controlled high-frequency damping are met. The condition for second order accuracy has been shown to be

$$\gamma = \frac{1}{2} + \alpha_m - \alpha_f, \tag{4.51}$$

and the control for the higher frequency damping has been shown to read

$$\alpha_m = \frac{1}{2}\frac{3-\rho_\infty^h}{1+\rho_\infty^h}, \quad \alpha_f = \frac{1}{1+\rho_\infty^h} \tag{4.52}$$

where $0 \leq \rho_\infty^h \leq 1$ is the only remaining time integration parameter, and represents the spectral radius, defined as the modulus of the amplification factor

$$\rho_\infty^h = lim_{\Delta t \to \infty} \rho^h, \quad \rho^h = |\frac{u_{n+1}}{u_n}|. \tag{4.53}$$

It is this parameter that provides the flexibility of the generalised-α method. For example, if $\rho_\infty^h = 1$, the method becomes identical to the trapezoidal rule. Details of the formation of equations (4.51) and (4.52) are provided in Dettmer and Perić [16, 17] and Jansen *et al* [35].

Incompressible Navier-Stokes Equations

In section (SUPG/PSPG) the spatial finite element discretisation of the incompressible Navier-Stokes equations is presented in equations (4.39) and (4.40). Combining these with the discrete generalised-α time integration method is known as a *semi-discrete* solution procedure, and results in the introduction of the time derivatives $\mathbf{u}_\alpha^h$ and $\dot{\mathbf{u}}_\beta^h$,

$$\begin{aligned}\int_\Omega \Big[\boldsymbol{\omega}^h \cdot \rho\left(\dot{\mathbf{u}}_\beta^h + (\nabla \mathbf{u}_\alpha^h)\mathbf{u}_\alpha^h - \mathbf{f}\right) - \left(\nabla \cdot \boldsymbol{\omega}^h\right) p_\alpha^h \\ + 2\mu \nabla \boldsymbol{\omega}^h : \nabla^s \mathbf{u}_\alpha^h + (\nabla \cdot \mathbf{u}_\alpha^h) q^h\Big]\, dv - \int_{\Gamma_\mathbf{t}} \boldsymbol{\omega}^h \cdot \mathbf{t}_\alpha^h \, da \\ + \sum_{e=1}^{n_{el}} \int_{\Omega^e} \left[\tau_\mathbf{u} \rho (\nabla \boldsymbol{\omega}^h)\mathbf{u}_\alpha^h + \tau_p \nabla q^h\right] \cdot \left[\rho\left(\dot{\mathbf{u}}_\beta^h + (\nabla \mathbf{u}_\alpha^h)\mathbf{u}_\alpha^h - \mathbf{f}\right) + \nabla p_\alpha^h\right] dv = 0,\end{aligned} \tag{4.54}$$

where $\tau_\mathbf{u}$ and τ_p are evaluated based on $\mathbf{u}_\alpha^h$, and

$$
\begin{aligned}
\mathbf{u}_{\alpha}^{h} &= \alpha_f \mathbf{u}_{n+1}^{h} + (1-\alpha_f)\mathbf{u}_{n}^{h} \\
\dot{\mathbf{u}}_{\beta}^{h} &= \frac{\alpha_m}{\gamma \Delta t}\mathbf{u}_{n+1}^{h} - \frac{\alpha_m}{\gamma \Delta t}\mathbf{u}_{n}^{h} + (1-\frac{\alpha_m}{\gamma})\dot{\mathbf{u}}_{n}^{h} \\
\mathbf{t}_{\alpha}^{h} &= \alpha_f \mathbf{t}_{n+1}^{h} + (1-\alpha_f)\mathbf{t}_{n}^{h} \\
\dot{\mathbf{u}}_{n+1}^{h} &= \frac{1}{\gamma \Delta t}\mathbf{u}_{n+1}^{h} - \frac{1}{\gamma \Delta t}\mathbf{u}_{n}^{h} - \frac{1-\gamma}{\gamma}\dot{\mathbf{u}}_{n}^{h},
\end{aligned}
\tag{4.55}
$$

are the time discretised values of the system variables. It should be noted that the pressure serves as a Lagrangian multiplier ensuring incompressibility, and thus does not need to be discretised in time. Instead, the term p_{α}^{h} denotes the pressure associated with the same time instant as $\mathbf{u}_{\alpha}^{h}$ and $\dot{\mathbf{u}}_{\beta}^{h}$. The final combined semi-discrete formulation reads: For a given $\mathbf{u}_{n}^{h}$ and $\dot{\mathbf{u}}_{n}^{h}$, find $\mathbf{u}_{n+1}^{h} \in \mathcal{U}_{n+1}^{h}$ and $p_{\alpha}^{h} \in \mathcal{P}^{h}$ such that for any $\boldsymbol{\omega}^{h} \in \mathcal{W}^{h}$ and $q^{h} \in \mathcal{P}^{h}$ equation (4.54) is satisfied, where

$$
\begin{aligned}
\mathcal{U}_{n}^{h} &= \left\{ \mathbf{u}_{n}^{h} \in (H^1(\Omega))^{n_{sd}} | \mathbf{u}_{n}^{h}|_{\hat{\mathbf{x}}^h \in \Omega^e} \in (P_1(\Omega^e))^{n_{sd}},\ \mathbf{u}_{n}^{h}|_{\hat{\mathbf{x}}^h \in \Gamma_{\mathbf{g}}} = \mathbf{g}_n \right\} \\
\mathcal{W}^{h} &= \left\{ \boldsymbol{\omega}^{h} \in (H^1(\Omega))^{n_{sd}} | \boldsymbol{\omega}^{h}|_{\hat{\mathbf{x}}^h \in \Omega^e} \in (P_1(\Omega^e))^{n_{sd}},\ \boldsymbol{\omega}^{h}|_{\hat{\mathbf{x}}^h \in \Gamma_{\mathbf{g}}} = \mathbf{0} \right\} \\
\mathcal{P}^{h} &= \left\{ q^{h} \in (H^1(\Omega)) | q^{h}|_{\hat{\mathbf{x}}^h \in \Omega^e} \in (P_1(\Omega^e)) \right\}.
\end{aligned}
\tag{4.56}
$$

4.3.3 2-D Fluid Flow Examples

Example 1: Square Profile

In this section, a two dimensional finite element solver is used to predict the variation of aerodynamic forces acting on a body of square cross section with various angles of attack (α). A 1m square cross section was chosen as the profile to be modeled in the finite element solver, and a 2-D incompressible viscous fluid-only mesh was generated, centred on the square within an 80m by 60m domain. Element sizes ranged from having 0.05m sides along the solid boundary to having 10m sides at the outer range boundaries, and the overall mesh consisted of 7662 triangular elements. The material properties of the fluid domain were chosen as being $\rho = 1.0$ kg m^{-3}, $\mu = 0.01$ N s m^{-2} and $\mathrm{u}_{\infty} = 2.5$ m s^{-1}, leading to a Reynolds number of $\mathrm{Re} = \frac{\rho D u_{\infty}}{\mu} = 250$. The square profile was represented as a fully fixed, rigid boundary condition. By rotating the geometry of the square profile and

maintaining a constant, horizontal fluid flow, the lift and drag reaction forces at each node on the surface of the profile were obtained for varying α. This data was then interpolated for values of α ranging from 0 to 8 degrees in order to calculate the aerodynamic coefficients of the profile, and thus plot the relationship of Cy with α.

$$C_D = \frac{2F_D}{\rho D u_\infty^2}, \quad C_L = \frac{2F_L}{\rho D u_\infty^2}, \quad C_M = \frac{2F_M}{\rho D b u_\infty^2} \tag{4.57}$$

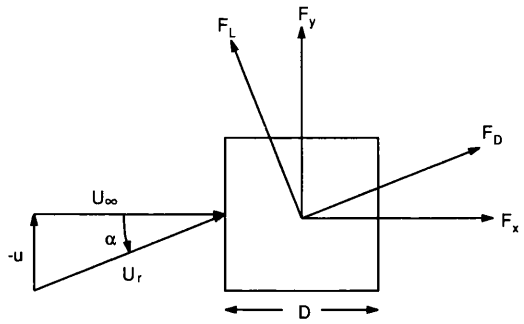

Figure 4.1: Angle of attack on a square profile

Figure 4.1 displays the orientation of the local forces acting on the rotated square with reference to the global forces of the domain. The aerodynamic coefficient C_y can thus be determined by calculating the resultant vector of C_D and C_L as:

$$C_y = C_L cos(\alpha) + C_D sin(\alpha) \tag{4.58}$$

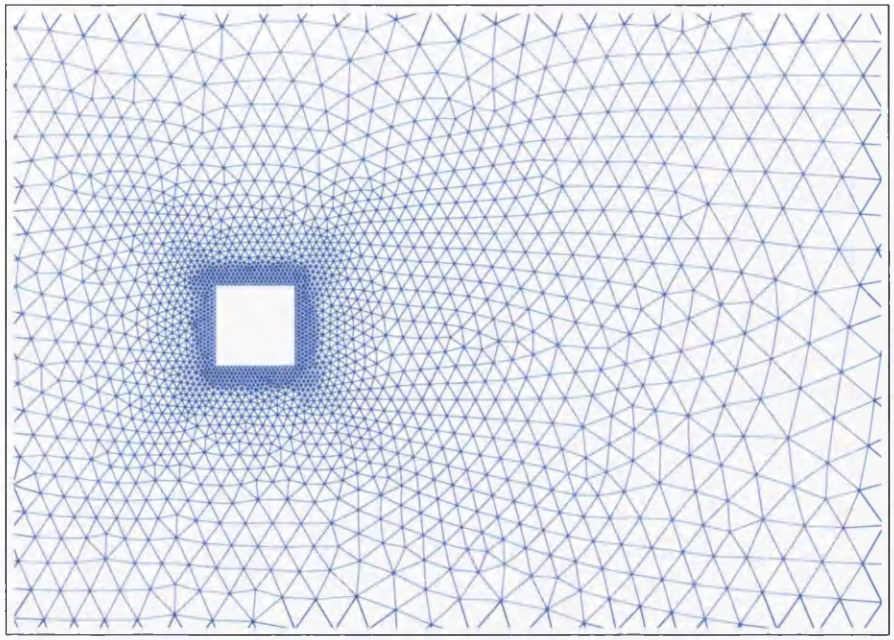

Figure 4.2: Detail of the fluid-only mesh

Figure 4.2 shows the fluid-only mesh employed in this example. It should be noted that the regions of higher mesh density near the sharp edges of the internal boundary are necessary to capture the shear separation of the fluid from the boundary. Likewise the wake region downstream of the internal boundaries requires a higher mesh density than the surrounding fluid region in order to accurately capture the behavior of the vortices that shed off of the internal boundaries. By isolating the areas of high mesh density to the regions in which they are necessary it is possible to significantly reduce the total number of degrees of freedom to be solved, and thus the computational cost of the simulation.

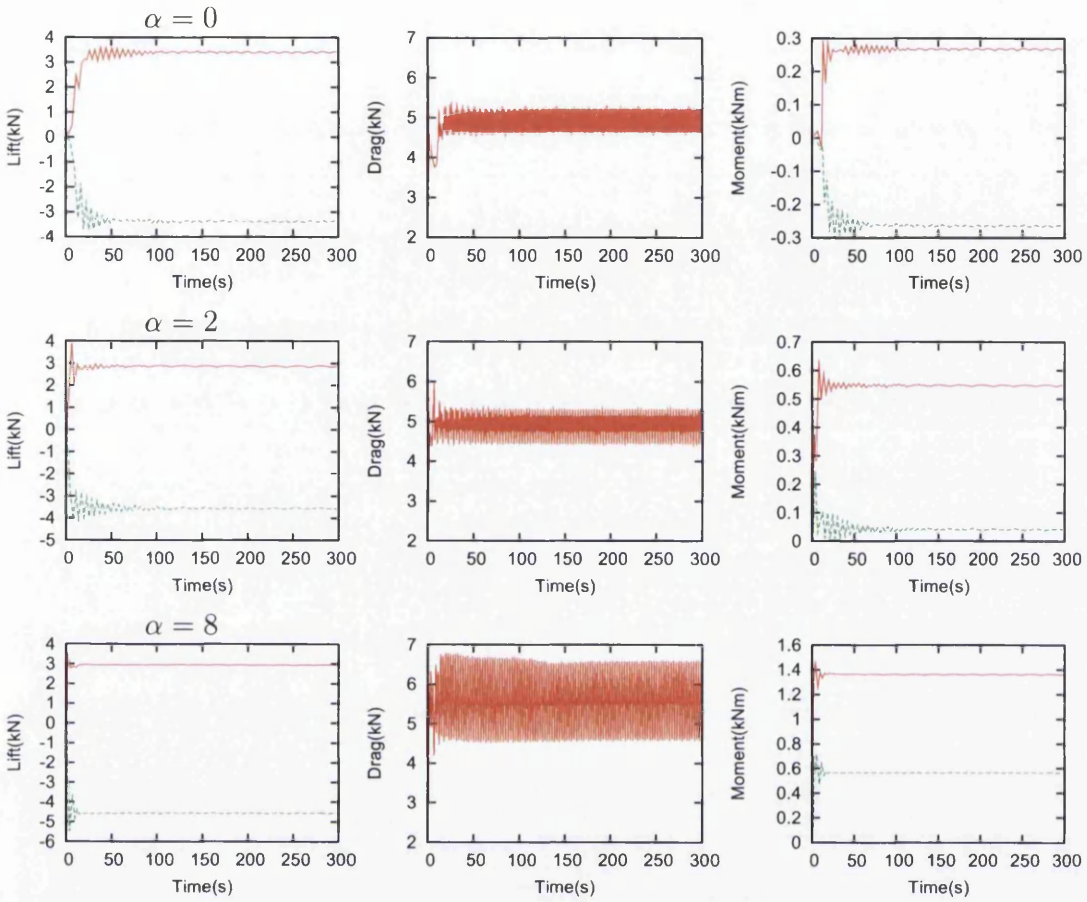

Figure 4.3: Lift, drag, and moment amplitudes for varying α. In the interest of simplicity, some plots have been represented by maximum (red) and minimum (green) amplitude only.

In figure 4.3 each column relates to the lift, drag and moment forces acting on the square profile respectively. The first and third columns display only the maximum and minimum values of the amplitude oscillation for clarity. It can be seen from the above graphs that vortex shedding occuring at a frequency of $\approx 1.6\ s^{-1}$ is causing a significant fluctuation of the forces acting on the square profile. In the case of $\alpha = 8$ a fluctuation of $\pm 18\%$ is observed.

By taking the average of the forces acting on the square profile it is possible to determine the relationship of the aerodynamic coefficients with the rotation of the square geometry as displayed in figure 4.4.

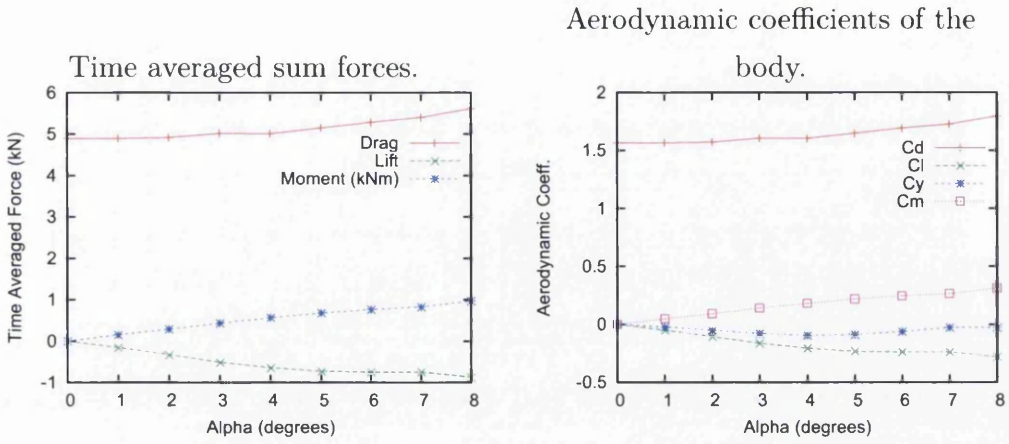

Figure 4.4: Variation of time averaged forces and derived aerodynamic coefficients of square profile with rotation α

Example 2.1: Bridge Cross-Section

In this section, the same method used in section 4.3.3 was used to predict the forces acting on a simplified cross-section of a typical bridge deck. In this case, an 80m by 80m domain was centred on a 12m x 2.4m x 0.3m "H Beam" profile representing the bridge deck, based on work presented by Dettmer [16], and Hübner *et al* [30]. Element sizes of the incompressible, viscous fluid-only mesh ranged from having 0.01m sides along sections of the solid boundary to having 10m sides at the outer range boundaries, and the overall mesh consisted of $\approx$ 7000 triangular elements, depending on the orientation of the bridge deck, as shown in figure 4.5. The material properties of the fluid domain were chosen as being $\rho = 1.0$ kg m^{-3}, $\mu = 0.01$ N s m^{-2} and $u_\infty = 1.0$ m s^{-1}, leading to a Reynolds number of $\mathrm{Re} = \frac{\rho D u_\infty}{\mu} = 1200$. In this case the range of rotation considered was $\alpha = 0 : 5 : 45$ degrees. Given the relatively more complicated geometry of the solid boundary compared to the previous section, a more refined mesh was necessary in order to ensure stability under large rotations. This was achieved by concentrating high mesh density around the sharp corners of the H profile, as well as the inclusion of a higher density wake region region downstream of the deck. Results of this analysis are shown in figures 4.6 and 4.7.

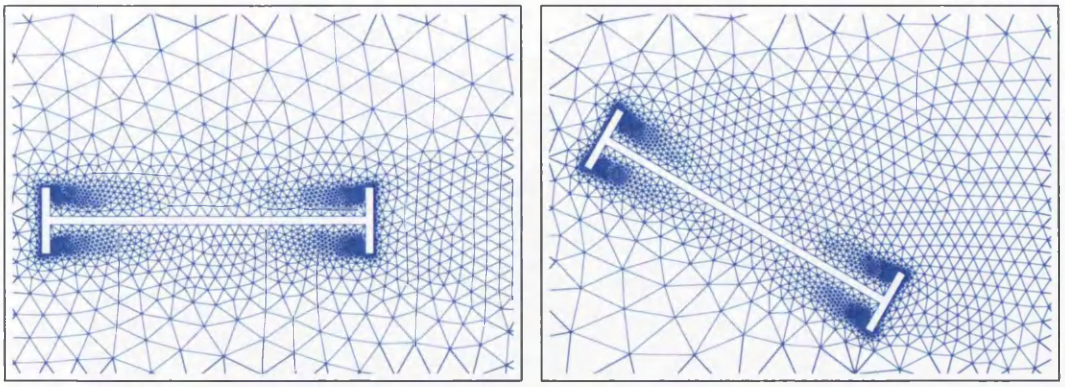

$\alpha = 0$ $\alpha = 30$

Figure 4.5: Detail of the fluid-only mesh

Example 2.2: 2-DOF Simulation of Rigid Bridge Deck Flutter

By using a Fourier curve fitting tool to plot the variation of the bridge deck aerodynamic coefficients with α (shown in figures 4.8 and 4.9), and including the Fourier series obtained into the Newton Raphson solver described in section 2.2.3 it is possible to construct a simple simulation in order to predict the critical velocity U_{cr} above which the deck will undergo flutter. The curve fitting tool used for this purpose was the least squares method package included in the open source program *gnuplot*. Due to the physical nature of the structure being modeled, the range of α considered in section 2.2.3 was $\pm$ 45°, however in order to ensure numerical stability for large deformations above the expected physical range, the data set obtained from the 2-D solver was extrapolated by a simple linear relationship of C_y and $C_\theta \rightarrow 0$ as $\alpha > 45° \rightarrow 90°$. Results obtained are shown in figures 4.10 and 4.11.

The material parameters of the bridge deck were based on work presented by Dettmer [16] and Hübner *et al* [30]; however, the stiffness of the bridge was increased and a value for structural damping included due to the simplified nature of the model problem. The geometry remains the same as in section 4.3.3 with the bridge profile being 12.0m x 2.4m x 0.3m considered over a unit span. The fluid properties are set to $\mu = 0.1$ N s m^{-2} and $\rho = 1.25$ kg m^{-3} and a range of inflow velocities from 0.01 m s^{-1} to 15.0 m s^{-1} leading to a range of Reynolds numbers considered Re $= \frac{u_\infty b \rho}{\mu} = 1.5 : 2250$. The rigid body properties were set to $k_y = 4000$ N m^{-1}, m = 3000 kg, $c_y = 200$ N s m^{-1}, $k_\theta = 40000$ N m, $c_\theta = 200$ N m s, and $I_\theta = 25300$ kg m^2.

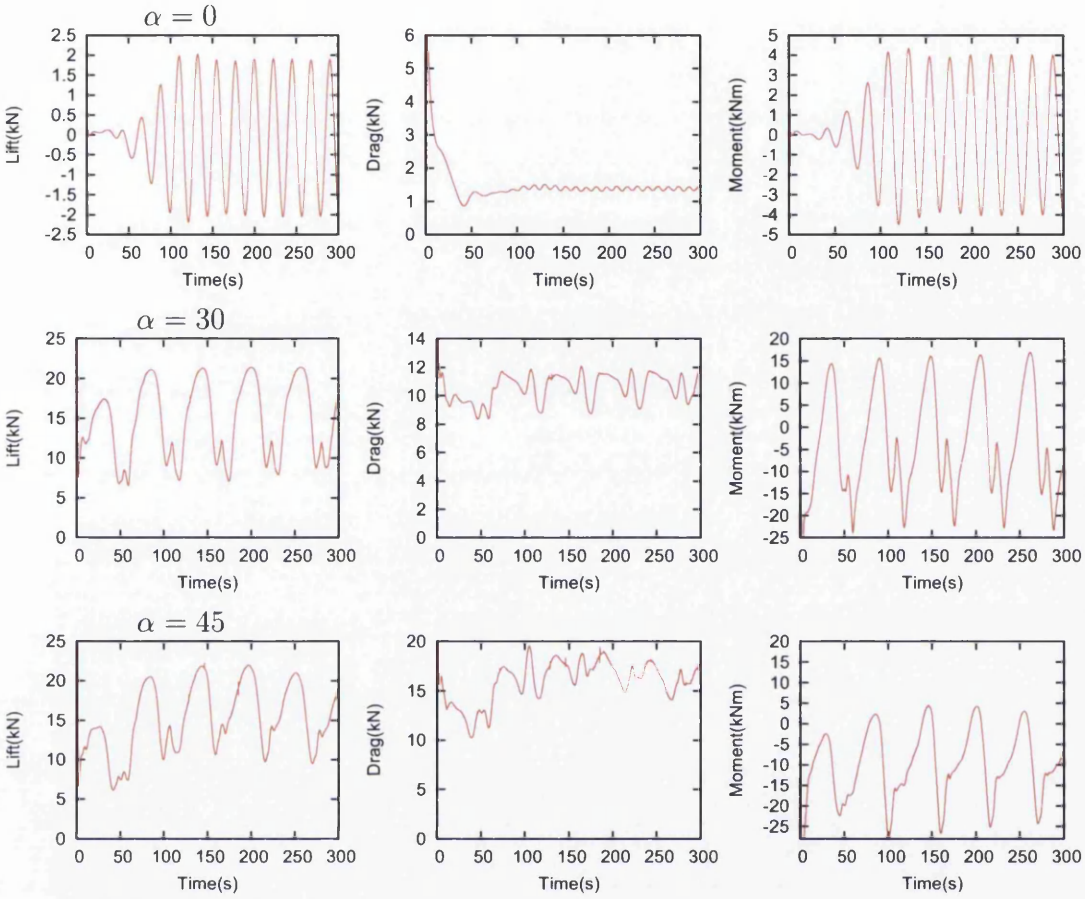

Figure 4.6: Lift, drag, and moment forces for varying α

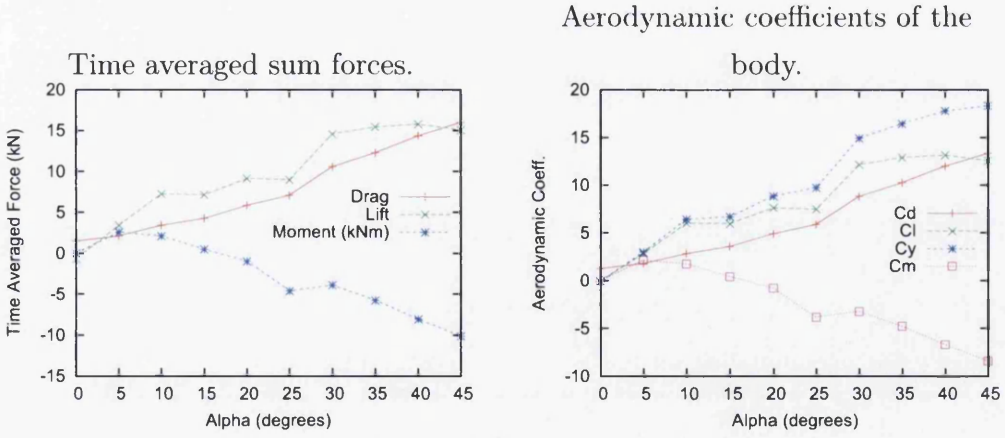

Figure 4.7: Variation of time averaged forces and derived aerodynamic coefficients of bridge deck with rotation α

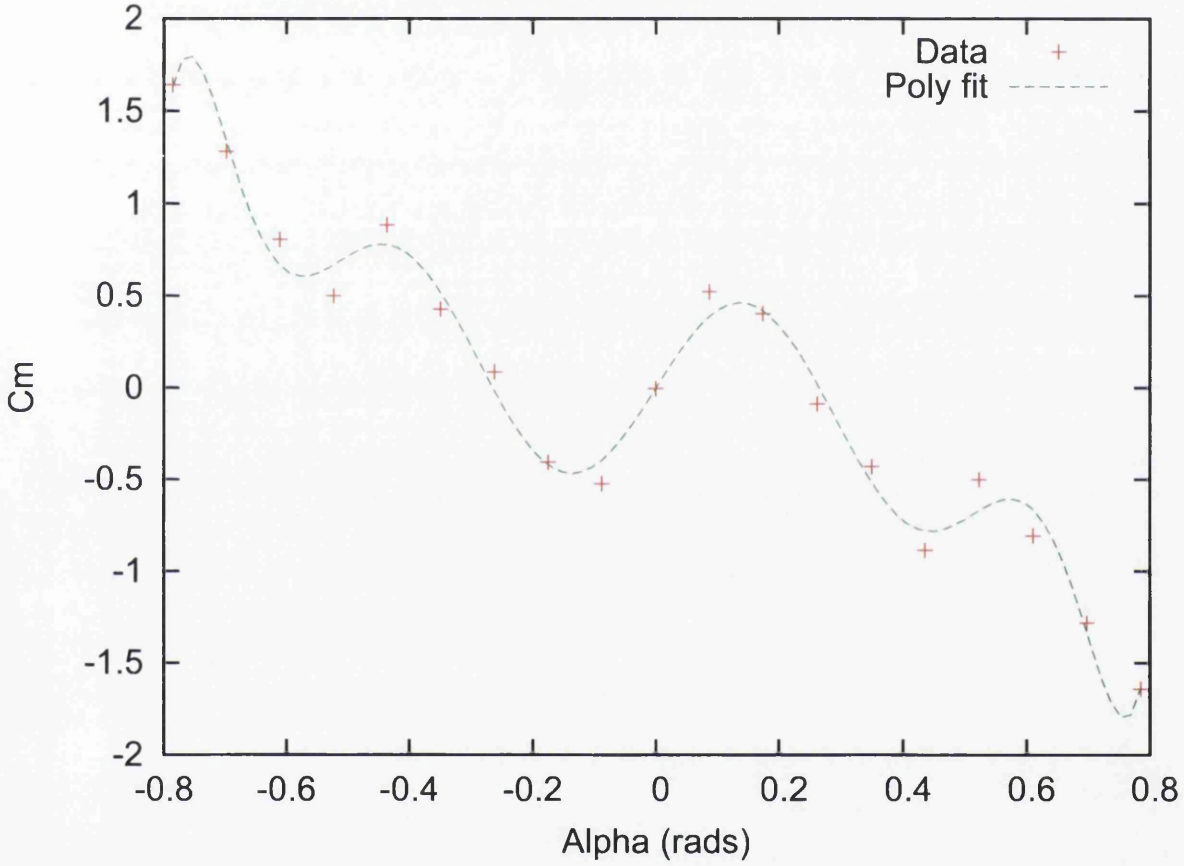

Figure 4.8: Variation of derived C_m of bridge deck with rotation α

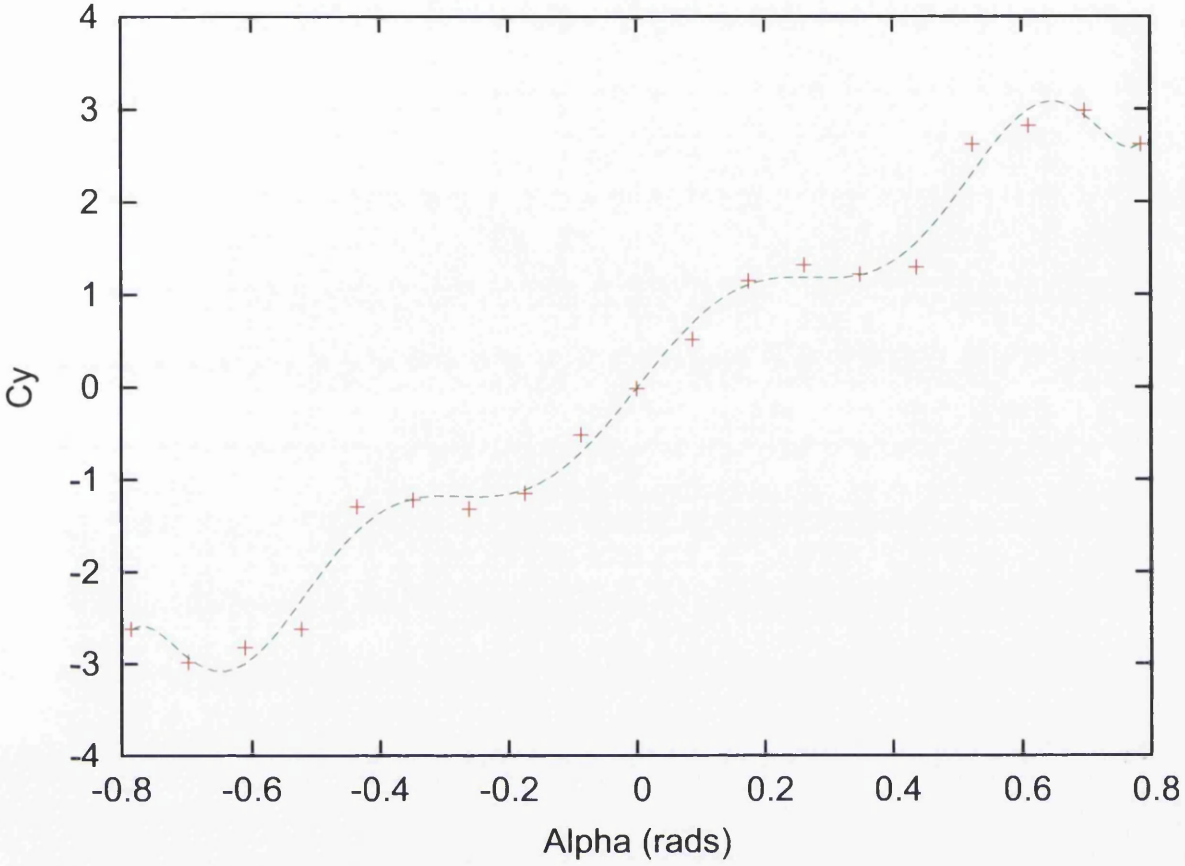

Figure 4.9: Variation of derived C_y of bridge deck with rotation α

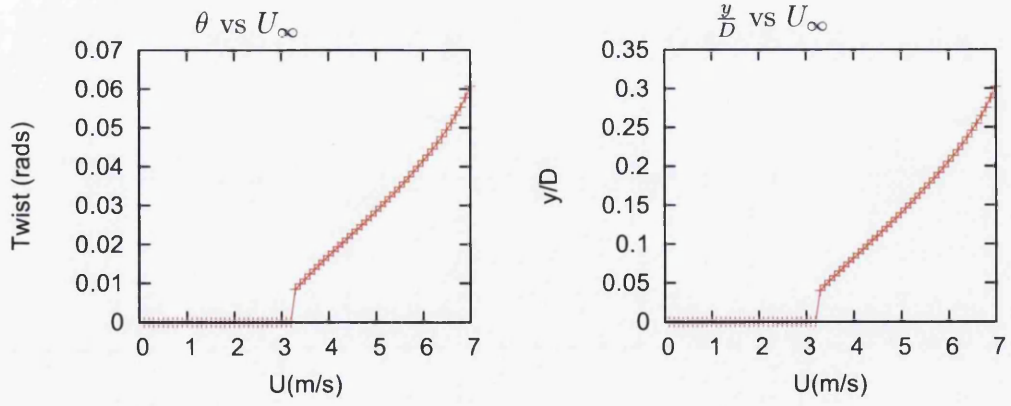

Figure 4.10: Variation of maximum displacement of bridge deck with fluid velocity U_∞

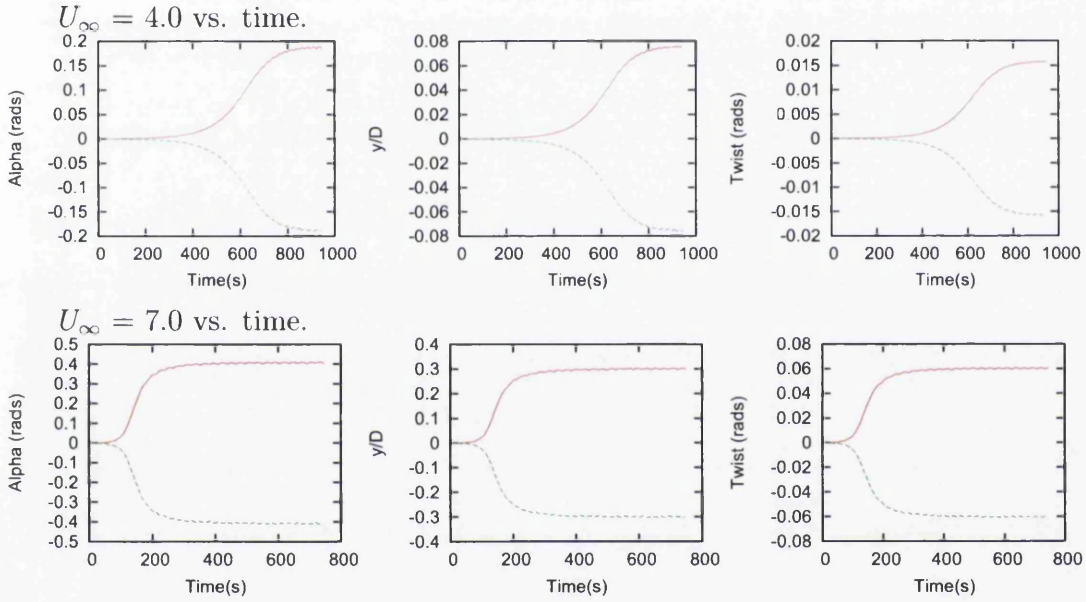

Figure 4.11: Variation of displacement over time for specified inflow velocities. For simplicity, displacement is presented as maximum (red) and minimum (green) amplitude.

Chapter 5

FE Modelling for FSI

5.1 The Arbitrary Lagrangian-Eulerian Description of Fluid Flow

As described in section 3.2.1 the numerical modelling of fluid-structure interaction necessitates the employment of numerical techiniques capable of adapting to moving fluid boundaries. The *arbitrary Lagrangian-Eulerian* (ALE) description of fluid flow consists of a compromise between a reference frame fixed in space (Eulerian) and a reference frame fixed to the motion of the fluid particle (Lagrangian). This compromise results in a reference frame allowed to move independently of the fluid flow, thus enabling the fluid mesh to deform along moving boundaries such as the fluid-solid interface. It should be noted that the regions of the fluid mesh that do not need to deform to accomodate the moving boundary conditions may be restricted to a purely Eulerian flow, resulting in a significant increase in computational efficiency. Publications presenting the application of the ALE scheme include: Hirt *et al* [28], Hughes *et al* [34], Donea [25], Ramaswamy and Kawahara [47, 48], Huerta and Liu [31], Soulaimani *et al* [56], Tezduyar *et al* [58, 59], Nomura and Hughes [44], Sackinger *et al* [50], Masud and Hughes [45], Soulaimani and Saad [57], Behr and Tezduyar [3], Braess and Wriggers [7], Belytschko *et al* [4], Hübner *et al* [30], Sarrate *et al* [52], and Dettmer and Perić [16, 18, 19, 20, 21].

5.1.1 Fluid Finite Element Formulation on a Moving Domain

Replacing the Eulerian finite element formulation presented in equation (4.54) with the ALE framework results in the mesh coordinates $\hat{\mathbf{x}}$ being free to deform. Similarly, the velocity field $\hat{\mathbf{v}}$ now denotes the current mesh motion. The newly defined unknowns $\hat{\mathbf{x}}$ and $\hat{\mathbf{v}}$ are then discretised using the same piecewise linear finite element method used to obtain (4.54). The governing equations for a moving reference frame described in section 3.2.1 result in the fluid velocity term $\mathbf{u}_\alpha^h$ being replaced by the relative velocity term $\mathbf{u}_\alpha^h - \hat{\mathbf{v}}_{\hat{\alpha}}^h$, integrated over the deformed spatial domain $\Omega_{\tilde{\alpha}}$ given by $\hat{\mathbf{x}}_{\tilde{\alpha}}^h$. The subscripts $_{\tilde{\alpha}}$ and $_{\hat{\alpha}}$ denote time discretised parameters which will later be defined. The final fomulation of the stabilised finite element method for a moving domain reads: For a given $\mathbf{u}_n^h$ and $\dot{\mathbf{u}}_n^h$, find $\mathbf{u}_{n+1}^h \in \mathcal{U}_{n+1}^h$ and $p_\alpha^h \in \mathcal{P}^h$ such that for any $\boldsymbol{\omega}^h \in \mathcal{W}^h$ and $q^h \in \mathcal{P}^h$

$$\begin{aligned}\int_{\Omega_{\tilde{\alpha}}} \Big[\boldsymbol{\omega}^h \cdot \rho\left(\dot{\mathbf{u}}_\beta^h + (\nabla \mathbf{u}_\alpha^h)(\mathbf{u}_\alpha^h - \hat{\mathbf{v}}_{\hat{\alpha}}^h) - \mathbf{f}\right) - \left(\nabla \cdot \boldsymbol{\omega}^h\right) p_\alpha^h \\ + 2\mu \nabla \boldsymbol{\omega}^h : \nabla^s \mathbf{u}_\alpha^h + (\nabla \cdot \mathbf{u}_\alpha^h) q^h\Big]\, dv - \int_{\Gamma_\mathbf{t}} \boldsymbol{\omega}^h \cdot \mathbf{t}_\alpha^h \, da \\ + \sum_{e=1}^{n_{el}} \int_{\Omega_{\tilde{\alpha}}^e} \left[\tau_\mathbf{u} \rho (\nabla \boldsymbol{\omega}^h)(\mathbf{u}_\alpha^h - \hat{\mathbf{v}}_{\hat{\alpha}}^h) + \tau_p \nabla q^h\right] \\ \cdot \left[\rho\left(\dot{\mathbf{u}}_\beta^h + (\nabla \mathbf{u}_\alpha^h)(\mathbf{u}_\alpha^h - \hat{\mathbf{v}}_{\hat{\alpha}}^h) - \mathbf{f}\right) + \nabla p_\alpha^h\right] dv = 0, \quad (5.1)\end{aligned}$$

where the finite element spaces are defined

$$\begin{aligned}\mathcal{U}_{n+1}^h &= \left\{\mathbf{u}_{n+1}^h \in (H^1(\Omega_{\tilde{\alpha}}))^{n_{sd}} | \mathbf{u}_{n+1}^h|_{\hat{\mathbf{x}}^h \in \Omega_{\tilde{\alpha}}^e} \in (P_1(\Omega_{\tilde{\alpha}}^e))^{n_{sd}},\ \mathbf{u}_{n+1}^h|_{\hat{\mathbf{x}}^h \in \Gamma_{\mathbf{g},\tilde{\alpha}}} = \mathbf{g}_n\right\} \\ \mathcal{W}^h &= \left\{\boldsymbol{\omega}^h \in (H^1(\Omega_{\tilde{\alpha}}))^{n_{sd}} | \boldsymbol{\omega}^h|_{\hat{\mathbf{x}}^h \in \Omega_{\tilde{\alpha}}^e} \in (P_1(\Omega_{\tilde{\alpha}}^e))^{n_{sd}},\ \boldsymbol{\omega}^h|_{\hat{\mathbf{x}}^h \in \Gamma_{\mathbf{g},\tilde{\alpha}}} = \mathbf{0}\right\} \quad (5.2) \\ \mathcal{P}^h &= \left\{q^h \in (H^1(\Omega_{\tilde{\alpha}})) | q^h|_{\hat{\mathbf{x}}^h \in \Omega_{\tilde{\alpha}}^e} \in (P_1(\Omega_{\tilde{\alpha}}^e))\right\}.\end{aligned}$$

The stabilisation parameters are likewise now based on the relative velocity term $\mathbf{u}_\alpha^e - \hat{\mathbf{v}}_{\hat{\alpha}}^e$

$$\tau = \frac{h^e}{2||(\mathbf{u}_\alpha^e - \hat{\mathbf{v}}_{\hat{\alpha}}^e)||\rho}\xi, \quad \xi = \frac{\beta_1}{\sqrt{1 + \left(\frac{\beta_1}{\beta_2 Re^e}\right)^2}}, \quad Re^e = \frac{||(\mathbf{u}_\alpha^e - \hat{\mathbf{v}}_{\hat{\alpha}}^e)||h^e \rho}{2\mu}, \quad (5.3)$$

As discussed in Chapter 4 the generalised-α method is employed to discretise all but the moving reference frame parameters $\hat{\mathbf{x}}_{\tilde{\alpha}}^h$ and $\hat{\mathbf{v}}_{\hat{\alpha}}^h$, therefore equations (4.51), (4.52) and (4.55)

remain unchanged. A simple generalised midpoint scheme is used to discretise $\hat{\mathbf{x}}^h_{\hat{\alpha}}$ and $\hat{\mathbf{v}}^h_{\hat{\alpha}}$, resulting in the relation

$$\begin{aligned}
\hat{\mathbf{x}}^h_{\hat{\alpha}} &= \alpha_f \hat{\mathbf{x}}^h_{n+1} + (1-\alpha_f)\hat{\mathbf{x}}^h_n \\
\hat{\mathbf{v}}^h_{\hat{\alpha}} &= \alpha_f \hat{\mathbf{v}}^h_{n+1} + (1-\alpha_f)\hat{\mathbf{v}}^h_n \\
\hat{\mathbf{v}}^h_{n+1} &= \frac{1}{\hat{\gamma}\Delta t}\hat{\mathbf{x}}^h_{n+1} - \frac{1}{\hat{\gamma}\Delta t}\hat{\mathbf{x}}^h_n - \frac{1-\hat{\gamma}}{\hat{\gamma}}\hat{\mathbf{v}}^h_n,
\end{aligned} \tag{5.4}$$

where $\hat{\gamma}$ is an integration parameter $\frac{1}{2} \leq \hat{\gamma} \leq 1$ which is set to $\hat{\gamma} = \gamma$ allowing the choice of ρ^h_∞ to define all time integration parameters. Assuming the nodal mesh positions defining the current mesh configuration $\hat{\mathbf{x}}_n$ are known, this system may be solved for the unknowns $\mathbf{u}^h_{n+1}$ and ρ^h_∞ using an appropriate numerical iteration technique such as the Newton-Raphson method.

5.1.2 Mesh Update Method: Non-Linear Pseudo-Elasticity

In the interest of obtaining a robust and efficient overall solution procedure, the method of updating the nodal positions of the mesh to account for moving boundary conditions is required to:

- have low computational cost
- maintain optimal mesh quality to avoid severe distortion of elements
- work on both structured and unstructured meshes
- be able to adapt the finite element mesh to accomodate severely distorted geometries
- allow for linearisation in order to be solved using the Newton-Raphson method. For example: by taking the derivative of the internal node positions with respect to the boundary nodes $d\hat{\mathbf{x}}_{int}/d\hat{\mathbf{x}}_{boun}$.

In this work, these criteria are met by the application of the *non-linear pseudo-elastic* method. This method treats the mesh as an elastic body, allowing for the movement of the mesh to be discretised using a standard Lagrangian finite element formulation, as

described in section 4.2. By employing a straightforward linear finite element fomulation, only one Gauss point is required to integrate over each element. The behavior of the mesh is described by hyper-elastic Neo-Hookean properties with the pseudo-material properties of the mesh described by the shear and bulk moduli, μ_{mesh} and K_{mesh} respectively. This behavior is then linearised and solved using a Newton-Raphson procedure. It should be noted that in this context, any volumetric locking that may result from finite element elasticity may be considered irrelevant.

This method may be better adapted to repeated oscillating solid deformation by retaining a 'stress-free' reference mesh configuration, typically obtained from $\hat{\mathbf{x}}$ at $t = 0$. Alternatively, large-scale deformations have been shown to be better accounted for by using the previous mesh configuration $\hat{\mathbf{x}}_{t-1}$ as the 'stress-free' reference configuration to obtain $\hat{\mathbf{x}}_t$.

5.2 Interface Modelling Strategy: Fluid-Solid Interface

This section describes the approach taken to the numerical description of the boundary between a fluid finite element mesh and a moving flexible body employed within this work.

5.2.1 Non-Matching Meshes: Nodal Interpolation

Generally in a fluid-structure interaction simulation, the fluid mesh will require a higher level of spatial discretisation, or *mesh density* , than that of the solid mesh. Increasing the solid mesh density to match is both tedious in the mesh generation stage and computationally expensive, as it increases the number of interface degrees of freedom which governs the overall computational cost of the solver. Instead, a means of interpolating between the fluid and solid meshes along the interface is employed, allowing for independent mesh density.

Due to the Lagrangian nature of the solid numerical model, the boundary nodes of the solid mesh provide an accurate description of the interface configuration, even for large deformations. The fluid interface nodes may therefore be considered as "glued" to the

surface of the solid, and the method described in section 5.1.2 may then be employed to adjust the position of the internal fluid nodes to the updated configuration of the interface. The no-slip boundary condition described by equation (3.22) shows that the fluid particles adjacent to the interface will also stick to the solid surface, resulting in the fluid particle velocity matching the fluid mesh velocity at the interface.

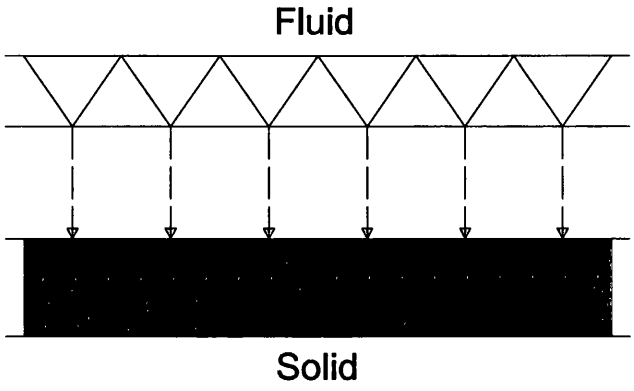

Figure 5.1: Diagram of interpolation of fluid nodes on the interface.

The behavior of the fluid and solid particles matching that of the fluid and solid meshes at the interface allows for the kinematic data of the fluid to be expressed in terms of the solid through the finite element interpolation method displayed in figure 5.1. This results in the fluid behavior being expressed as

$$\hat{\mathbf{x}}_A = \mathsf{c}_{B,A}\,(\mathbf{x}_{B,0} + \mathbf{d}_B) \tag{5.5}$$

$$\mathbf{u}_A = \hat{\mathbf{v}}_A = \mathsf{c}_{B,A}\,\dot{\mathbf{d}}_B \tag{5.6}$$

$$\dot{\mathbf{u}}_A = \mathsf{c}_{B,A}\,\ddot{\mathbf{d}}_B, \tag{5.7}$$

where $\hat{\mathbf{x}}_A$, $\mathbf{u}_A$, $\dot{\mathbf{u}}_A$, $\hat{\mathbf{v}}_A$ are vectors representing the interface nodal values of $\hat{\mathbf{x}}^h$, $\mathbf{u}^h$, $\dot{\mathbf{u}}^h$, and $\hat{\mathbf{v}}^h$. Likewise, $\mathbf{x}_{B,0}$, $\mathbf{d}_B$, $\dot{\mathbf{x}}_B$, and $\ddot{\mathbf{x}}_B$ represent the interface nodal values of the solid initial configuration, displacement, velocity and acceleration. Finally, the interpolation coefficient $\mathsf{c}_{B,A} = N^s_B(\xi_A)$ represents the value of the structural shape function of point B at the location of fluid node A. The enforcement of equations (5.5) - (5.7) ensures that kinematic consistency is maintained along the interface.

Similar to the kinematics of the interface, the equilibrium of forces at the interface is calculated using the finite element interpolation method and the principle of virtual work. Expressing a virtual displacement of the interface as

$$\delta \mathbf{d} = N_B^s \delta \mathbf{d}_B, \tag{5.8}$$

allows the sum work of the fluid and solid forces done over the virtual displacement to be written as

$$\delta \mathcal{W} = \mathbf{g}_A^f N_B^s(\xi_A) \delta \mathbf{d}_B \; + \; \mathbf{g}_B^s \delta \mathbf{d}_B = 0, \tag{5.9}$$

where the vectors $\mathbf{g}_A^f$ and $\mathbf{g}_B^s$ denote the residual nodal forces in fluid node A and solid node B respectively. The sum over all nodes A and B along the interface therefore reads

$$\mathbf{g}_A^f \mathsf{c}_{B,A} \; + \; \mathbf{g}_B^s = \mathbf{0}. \tag{5.10}$$

On the topic of computational implementation it should be noted that the values of $\mathsf{c}_{B,A}$ remain constant throughout the simulation, and the computational effort associated with the transfer of kinematics and forces at the interface is negligible. In the case of rotational degrees of freedom found in some structural elements such as beams or shells, as well as pressure in the fluid, transfer across the interface is not needed. In the case of two dimensional beam, plate, or membrane elements that are "wet" on both sides, the kinematics and forces of the solid are simply transferred to the fluid nodes on both sides.

Enforcing the kinematic consistency conditions (5.5) - (5.7) at the discrete time instants $t_n, t_{n+1}, \ldots$ allows for the separate temporal discretisation of fluid and solid domains. In this work the generalised-α method is employed to discretise both domains, however different formulae for α_m and α_f, as well as different values of the user controlled free integration parameter ρ_∞^h are employed.

Chapter 6

Solvers

Having discussed the finer details of discretising numerical models of fluid-structure interaction in previous chapters, the focus of this chapter will be the general implementation of the computational solution strategies employed in this work. Section 6.1 details the general decomposition of the problem into separate fluid, interface and solid domains. This decomposition results in three strongly coupled sets of highly non-linear equations, as well as allows for a high degree of modularity in the solution algorithm. The final sections of this chapter detail the differences between the monolithic, weakly coupled and partitioned solution schemes employed. As mentioned in Chapter 1, the solvers employed in this work have been developed and presented by D. Perić and W. Dettmer. These publications include: the monolothic Newton method, see *e.g.* Dettmer and Perić [16, 19, 20, 21, 51, 22], the block Gauss-Seidel procedure, see *e.g.* Joosten *et al* [39, 40], and the novel staggered scheme, see *e.g.* Dettmer and Perić [23].

6.1 Domain Decomposition

In this work, the interface domain is discretised using isoparametric finite elements comprised of nodes and interpolated using shape functions in an approach similar to those employed in the fluid and solid phases, with the interface degrees of freedom detailing the current configuration of the interface and the transfer of information between the other two phases.

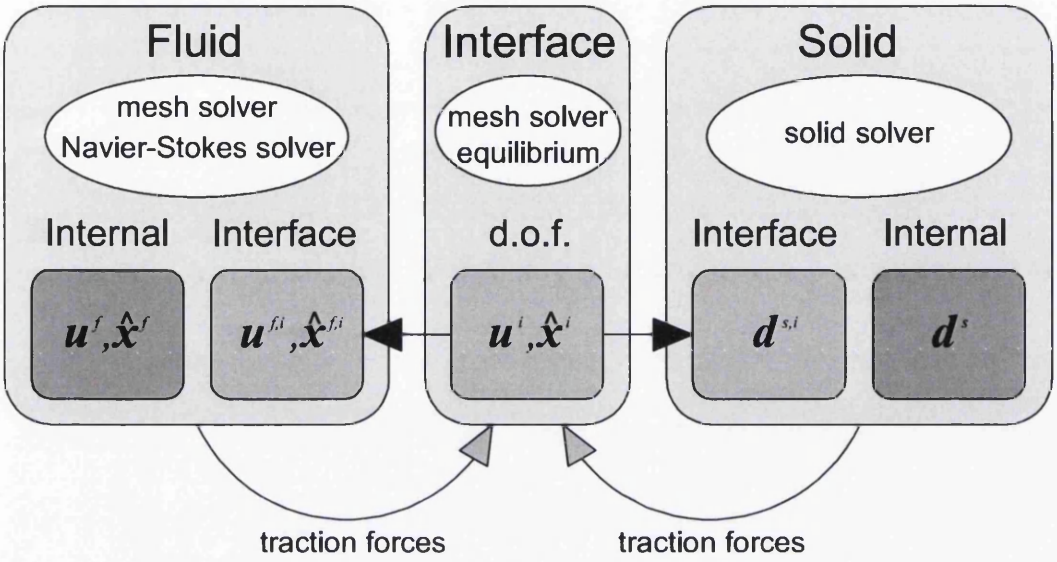

Figure 6.1: Decomposition of the system into separate domains.

Figure 6.1 details the decomposition and interaction of the three phases considered, while highlighting the modular separation of the solvers applied over each domain. The degrees of freedom of the fluid and solid phases associated with the interface ($\mathbf{u}^{f,i}$, $\hat{\mathbf{x}}^{f,i}$, $\mathbf{d}^{s,i}$) consist of the element nodal values in each phase located directly on the interface. As such, the governing equations of these phases may be written as

$$\mathbf{r}^f(\mathbf{u}_f, \mathbf{u}_i) = \mathbf{0} \quad \text{(Fluid Body)} \tag{6.1}$$

$$\mathbf{r}^m(\hat{\mathbf{x}}^f, \mathbf{u}^i) = \mathbf{0} \quad \text{(Fluid Mesh)} \tag{6.2}$$

$$\mathbf{g}^f(\mathbf{u}_f, \mathbf{u}_i) + \mathbf{g}^s(\mathbf{u}_i, \mathbf{d}_s) = \mathbf{0} \quad \text{(Interface)} \tag{6.3}$$

$$\mathbf{r}^s(\mathbf{u}_i, \mathbf{d}_s) = \mathbf{0} \quad \text{(Solid)} \tag{6.4}$$

where $\mathbf{u}_f = \{\mathbf{u}^f, \mathbf{u}^{f,i}\}$, $\hat{\mathbf{x}}^f = \{\hat{\mathbf{x}}^f, \hat{\mathbf{x}}^{f,i}\}$, $\mathbf{u}_i = \{\mathbf{u}^i, \hat{\mathbf{x}}^i\}$ and $\mathbf{d}_s = \{\mathbf{d}^{s,i}, \mathbf{d}^s\}$ are vectors representing the system unknowns to be calculated in the fluid, interface, and solid phases

respectively. The vectors $\mathbf{g}^f$ and $\mathbf{g}^s$ denote the traction forces exerted by the fluid and solid phases on the interface, while $\mathbf{r}^f$, $\mathbf{r}^m$, and $\mathbf{r}^s$ represent the fluid and solid phase solvers.

6.2 Monolithic Newton Method

This solution method consists of solving the entire fluid-structure interaction system simultaneously using the Netwon-Raphson method. In order to accomplish this the fluid, solid, and interface domains must first be combined to form a linearised monolithic system matrix as described by figure 6.2.

$$\begin{aligned} \mathbf{r}^f(\mathbf{u}_f, \mathbf{u}_i) &= \mathbf{0} \quad \text{(Fluid Body)} \\ \mathbf{r}^m(\hat{\mathbf{x}}^f, \mathbf{u}^i) &= \mathbf{0} \quad \text{(Fluid Mesh)} \\ \mathbf{r}^i(\mathbf{u}_f, \mathbf{u}_i, \mathbf{d}_s) &= \mathbf{0} \quad \text{(Interface)} \\ \mathbf{r}^s(\mathbf{u}_i, \mathbf{d}_s) &= \mathbf{0} \quad \text{(Solid)} \end{aligned}$$

$$\begin{bmatrix} \mathbf{K}_{ff} & \mathbf{K}_{fm} & \mathbf{K}_{fi} & \mathbf{0} \\ \mathbf{0} & \mathbf{K}_{mm} & \mathbf{K}_{mi} & \mathbf{0} \\ \mathbf{K}_{if} & \mathbf{K}_{im} & \mathbf{K}_{ii} & \mathbf{K}_{is} \\ \mathbf{0} & \mathbf{0} & \mathbf{K}_{si} & \mathbf{K}_{ss} \end{bmatrix} \cdot \begin{bmatrix} \Delta\mathbf{u}_f \\ \Delta\hat{\mathbf{x}}_f \\ \Delta\mathbf{u}_i \\ \Delta\mathbf{d}_s \end{bmatrix} = - \begin{bmatrix} \mathbf{r}^f \\ \mathbf{r}^m \\ \mathbf{r}^i \\ \mathbf{r}^s \end{bmatrix} \tag{6.5}$$

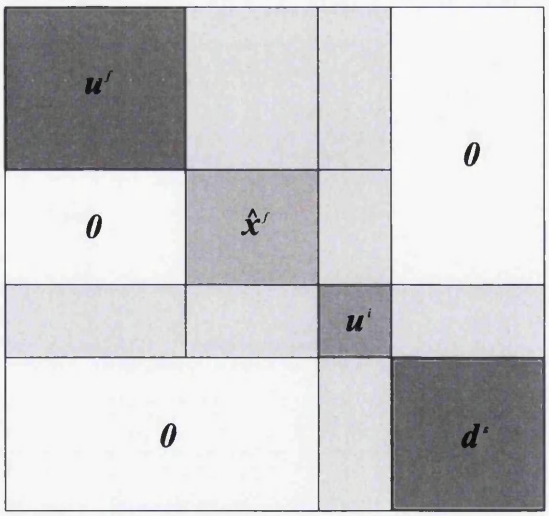

Figure 6.2: The monolithic system matrix.

System (6.5) is then solved by first guessing initial values for the system variables $\mathbf{U}_{n+1}$. Using these values the monolithic system matrix $\mathbf{K}$ is then solved iteratively using the Newton-Raphson method for the values of $\mathbf{U}_{n+1}$ that satisfy the governing equations $\mathbf{R}(\mathbf{U})$ to an acceptable level of accuracy. Once the desired level of accuracy has been met, the system variables are updated and the method may now move on to the next time step. A summary of this process is provided in box 6.1.

Box 6.1: Summary of Monolithic Newton Algorithm

1. Guess initial values of $\mathbf{U}^i_{n+1}$.
2. Insert initial values of $\mathbf{U}^i_{n+1}$ into equation 6.5 to determine if accuracy is within tolerable levels.
3. If tolerance is not met, calculate new estimate $\mathbf{U}^{i+1}_{n+1} = \mathbf{U}^i_{n+1} + \Delta\mathbf{U}$ where
$$\Delta\mathbf{U} = -\frac{\mathbf{R}(\mathbf{U}^i_{n+1})}{\mathbf{K}}$$
and return to step 2 using $\mathbf{U}^{i+1}_{n+1}$ as the new estimate. If tolerance has been met go to step 4.
4. Update system variables by setting $\mathbf{U}_n = \mathbf{U}_{n+1}$ and go to next time step.

6.3 Weakly Coupled Staggered Scheme

This solution method is based on the consideration of separate fluid and solid phases. First, a value for the traction forces exerted on the solid by the fluid is predicted and used to solve for the solid, and thus the interface, displacement. This updated interface configuration is then used to calculate new values for the fluid body behavior and traction forces. Finally, a weighted average of the predicted and calculated values of the traction forces is taken for use in the next time step. This method may sometimes result in a violation of equilibrium at the interface, particularly in the case of small solid over fluid mass ratios and is thus considered to be *weakly coupled* .

The application of this method requires the modification of equations (6.1) - (6.4) by the inclusion of an interface traction force vector $\mathbf{t}_i$, and the separation of the interface phase into fluid and solid interface terms. It should be noted that for simplicity of exposition solving for the mesh motion has been omitted throughout the remainder of this chapter.

$$\left.\begin{aligned} \mathbf{r}^f(\mathbf{u}_f, \mathbf{u}_i) &= \mathbf{0} \\ \mathbf{g}^f(\mathbf{u}_f, \mathbf{u}_i) &= \mathbf{t}_i \end{aligned}\right\} \quad \text{Fluid} \tag{6.6}$$

$$\left.\begin{aligned} \mathbf{r}^s(\mathbf{u}_i, \mathbf{d}_s) &= \mathbf{0} \\ \mathbf{g}^s(\mathbf{u}_i, \mathbf{d}_s) &= -\mathbf{t}_i \end{aligned}\right\} \quad \text{Solid} \tag{6.7}$$

Box 6.2 provides a summary of the novel staggered solution algorithm. Note that the structural displacement is calculated using the predicted traction vector $\mathbf{t}^p_{i,n+1}$. The difference, e, between the predicted traction vector and the calculated traction vector $\mathbf{t}^*_{i,n+1}$ quantifies the violation of equations (6.6) and (6.7).

$$\mathbf{t}^p_{i,n+1} - \mathbf{t}^*_{i,n+1} = e. \tag{6.8}$$

The weighted average parameter β employed in step 4 is chosen by the user and is typically set to 0.5. If β is set to 0, the traction force vector determined by the fluid is completely ignored. It must be noted that while reducing the value of β increases the ability of this solution method to accomodate smaller solid over fluid mass ratios, doing so results in a loss of accuracy which becomes more significant as β approaches zero.

Box 6.2: Summary of Staggered Scheme Algorithm

1. Predict traction force:

$$\mathbf{t}^{p}_{i,n+1} = 2\mathbf{t}_{i,n} - \mathbf{t}_{i,n-1}$$

2. Load solid with predicted traction force and solve for interface displacement:

$$\left.\begin{aligned} \mathbf{r}^{s}(\mathbf{u}_{i,n+1}, \mathbf{d}_{s,n+1}) &= \mathbf{0} \\ \mathbf{g}^{s}(\mathbf{u}_{i,n+1}, \mathbf{d}_{s,n+1}) &= -\mathbf{t}^{p}_{i,n+1} \end{aligned}\right\} \quad \text{Solve for } \mathbf{u}_{i,n+1}, \mathbf{d}_{s,n+1}$$

3. Update fluid mesh, then solve fluid body for calculated traction force:

$$\left.\begin{aligned} \mathbf{r}^{f}(\mathbf{u}_{f,n+1}, \mathbf{u}_{i,n+1}) &= \mathbf{0} \\ \mathbf{g}^{f}(\mathbf{u}_{f,n+1}, \mathbf{u}_{i,n+1}) &= -\mathbf{t}^{*}_{i,n+1} \end{aligned}\right\} \quad \text{Solve for } \mathbf{u}_{f,n+1}, \mathbf{t}^{*}_{i,n+1}$$

4. Calculate the average of the traction forces:

$$\mathbf{t}_{i,n+1} = \beta\mathbf{t}^{*}_{i,n+1} + (1-\beta)\mathbf{t}^{p}_{i,n+1}$$

5. Go to next time step.

6.4 Partitioned Block Gauss-Seidel

Similar to the approach taken in the staggered scheme, the *Block Gauss-Seidel* method separates the coupled FSI system into fluid and solid domains.

$$\left.\begin{aligned} \mathbf{R}^{F}_{1}(\mathbf{u}_f, \mathbf{u}_i) &= \mathbf{0} \\ \mathbf{R}^{F}_{2}(\mathbf{u}_f, \mathbf{u}_i) &= \mathbf{t}_i \end{aligned}\right\} \quad \text{Fluid} \tag{6.9}$$

$$\left.\begin{aligned} \mathbf{R}^{S}_{1}(\mathbf{u}_i, \mathbf{d}_s) &= \mathbf{0} \\ \mathbf{R}^{S}_{2}(\mathbf{u}_i, \mathbf{d}_s) &= -\mathbf{t}_i \end{aligned}\right\} \quad \text{Solid} \tag{6.10}$$

This method forms the solution at the next time step by first guessing an initial interface displacement, $\mathbf{u}^p_{i,n+1}$. This displacement is then used to solve the fluid domain for an updated interface traction force, $\mathbf{t}_{i,n+1}$, which is used in turn to solve the solid domain for a calculated interface displacement, $\mathbf{u}^*_{i,n+1}$. If the error quantified by the difference $\mathbf{u}^p_{i,n+1} - \mathbf{u}^*_{i,n+1}$ is larger than the desired tolerance, the calculated value of $\mathbf{u}^*_{i,n+1}$ is used as an updated prediction for $\mathbf{u}^p_{i,n+1}$ and the systems are solved again. Box 6.3 displays a summary of the solution algorithm.

Box 6.3: Summary of Block Gauss-Seidel Algorithm

1. Guess interface displacement $\mathbf{u}^p_{1,n+1}$

2. Use $\mathbf{u}^p_{1,n+1}$ to solve solid domain for $\mathbf{d}_{s,n+1}$ and $\mathbf{t}_{i,n+\gamma}$:

$$\left.\begin{aligned} \mathbf{R}^S_1(\mathbf{u}^p_{i,n+1}, \mathbf{d}_{s,n+1}) &= \mathbf{0} \\ \mathbf{R}^S_2(\mathbf{u}^p_{i,n+1}, \mathbf{d}_{s,n+1}) &= -\mathbf{t}_{i,n+\gamma} \end{aligned}\right\} \quad \text{Solve for } \mathbf{d}_{s,n+1}, \mathbf{t}_{i,n+\gamma}$$

3. Use $\mathbf{t}_{i,n+\gamma}$ to solve fluid domain for $\mathbf{u}_{f,n+1}$ and $\mathbf{u}^*_{i,n+1}$:

$$\left.\begin{aligned} \mathbf{R}^F_1(\mathbf{u}_{f,n+1}, \mathbf{u}^*_{i,n+1}) &= \mathbf{0} \\ \mathbf{R}^F_2(\mathbf{u}_{f,n+1}, \mathbf{u}^*_{i,n+1}) &= -\mathbf{t}_{i,n+\gamma} \end{aligned}\right\} \quad \text{Solve for } \mathbf{u}_{f,n+1}, \mathbf{u}^*_{i,n+1}$$

4. If $\mathbf{u}^p_{i,n+1} - \mathbf{u}^*_{i,n+1} > tol$, set $\mathbf{u}^p_{i,n+1} = \mathbf{u}^*_{i,n+1}$ and go to step 2.

5. If required accuracy is met, update system and go to next time step.

It should be noted that while this method solves the fluid and solid domains separately, the strong coupling of the integrated system is maintained via the iterative communication of the interface traction force and displacement.

Chapter 7

Flexible Beam

7.1 General Description of Problem

As an entry exercise into full 3D numerical FSI modelling, it was decided to begin with a simple external flow simulation. This was done by constructing a model problem consisting of a long slender beam, fully fixed at both ends and subjected to a steady uniform transverse fluid flow. This model was then solved using the monolithic Newton, block Gauss-Seidel and weakly coupled solvers in order to establish a comparison between the solution methods.

7.2 Formulation of Mesh and Boundary Conditions

As a starting point for this model problem, it was decided to take the geometrical properties of the rigid rectangular body from Dettmer and Perić [19] and extrapolate them into three dimensions. This resulted in a rectangular beam 4x1x30m long fully submerged in a fluid domain of 80x60x30m. The solid domain was discretised using 60 eight-noded brick elements, while the fluid mesh consisted of 146.5k four-noded tetrahedral elements. The material properties of the flexible beam were taken as $\rho_s = 70.588$, $I_p = 400$, $K_s = 1783.6$ and $G_s = 823.2$ equating to a Young's modulus of $E_s = 2140.32$ and a Poisson's ratio of $\nu_s = 0.3$, while the fluid properties were $\rho_f = 1.0$, $\mu_f = 0.01$ and inflow velocity $U_\infty = 2.5$ ramped up sinusoidally from 0 over the first 10 seconds of simulation and then

held constant. With a chord length of $D = 1.0$ this results in a Reynold's number of $Re = \frac{\rho_f U_\infty D}{\mu_f} = 250$.

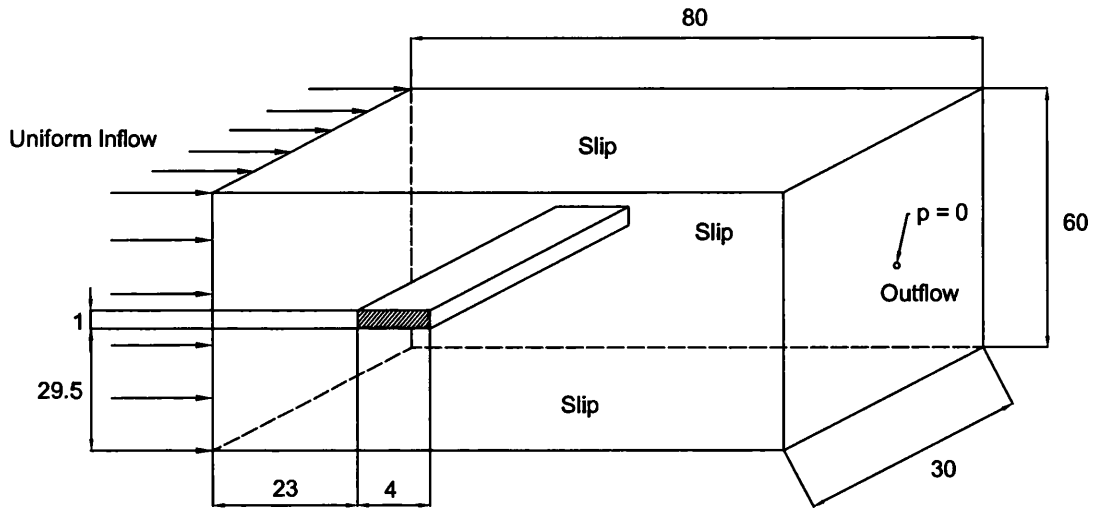

Figure 7.1: Diagram of boundary conditions and dimensions.

Figure 7.1 displays the boundary conditions and geometry of the model problem being considered, with the flexible beam fully fixed at both ends. The boundary conditions of the fluid domain were such that the fluid velocities were fixed at the inlet, one point at the outlet fixed in pressure, and all other outer boundaries slip. Figures 7.3 and 7.2 display the fluid and solid meshes employed in this simulation. It should be noted that a higher mesh density is required at certain critical areas of the fluid mesh, such as any sharp edges on the fluid-solid interface where shear separation may occur, as well as the wake region downstream of the solid in order to resolve the behavior of the fluid vortices.

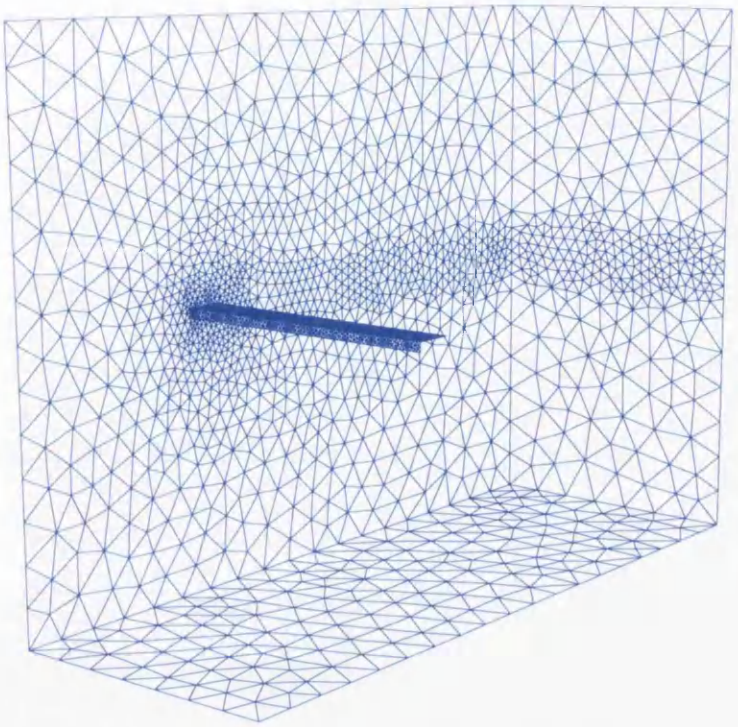

Figure 7.2: Image of the fluid mesh domain.

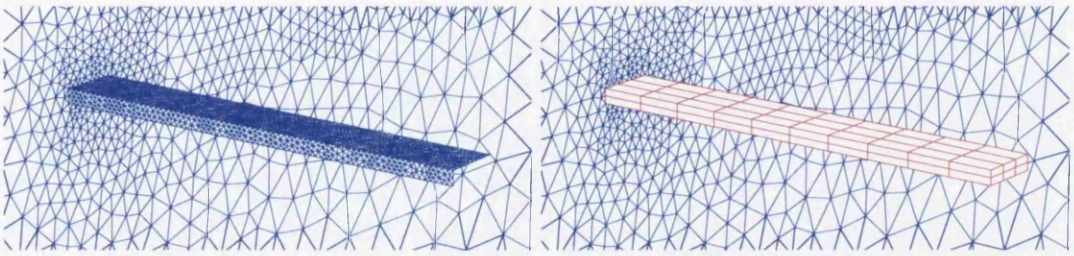

Figure 7.3: Images detailing the fluid mesh density on the interface, and the solid mesh.

7.3 Analysis of Simple Elastic Beam Bridge

Figures 7.4 - 7.6 display the solution results obtained by all three solvers, while Figure 7.7 displays contour plots of the pressure acting on the surface of the deformed solid mesh. The elastic beam displays flutter behavior when subjected to the constant uniform inflow, resulting in large-scale deformations suitable for displaying the capability of the solvers to handle severely deformed meshes. The results of all three solvers agree very strongly until approximately 500s of simulated time, where the novel staggered scheme begins to lose agreement. Over the course of this analysis the monolithic Newton and block Gauss-Seidel solvers displayed a similar computational cost while the novel staggered scheme required roughly one third of the cost of the other solvers. While the strongly coupled solvers display a higher level of accuracy, the significant difference in computational cost poses a strong argument for the employment of the novel staggered solution scheme.

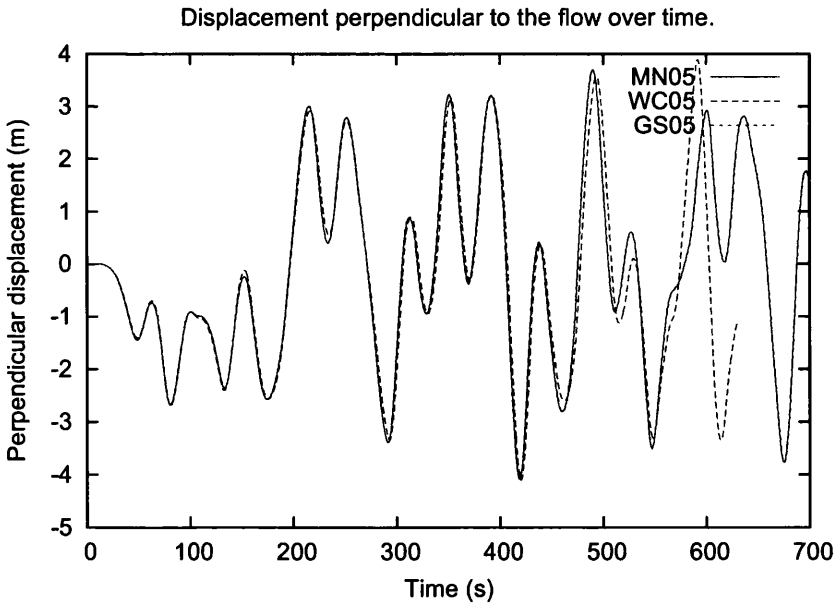

Figure 7.4: Vertical displacement of the central upstream point of the bridge. Legend denotes the Monolithic Newton, Weakly Coupled and Gauss Seidel solutions for $\Delta t = 0.5s$.

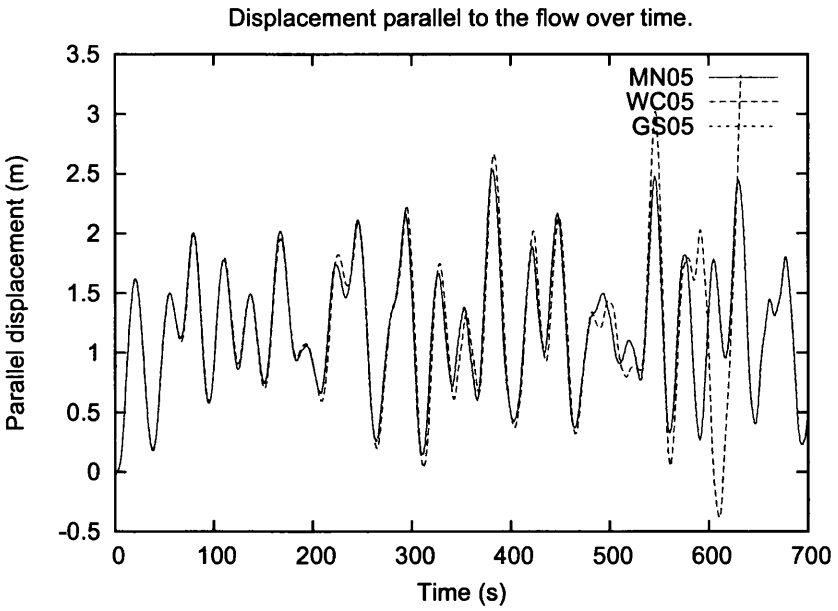

Figure 7.5: Horizontal displacement of the central upstream point of the bridge. Legend denotes the Monolithic Newton, Weakly Coupled and Gauss Seidel solutions for $\Delta t = 0.5s$.

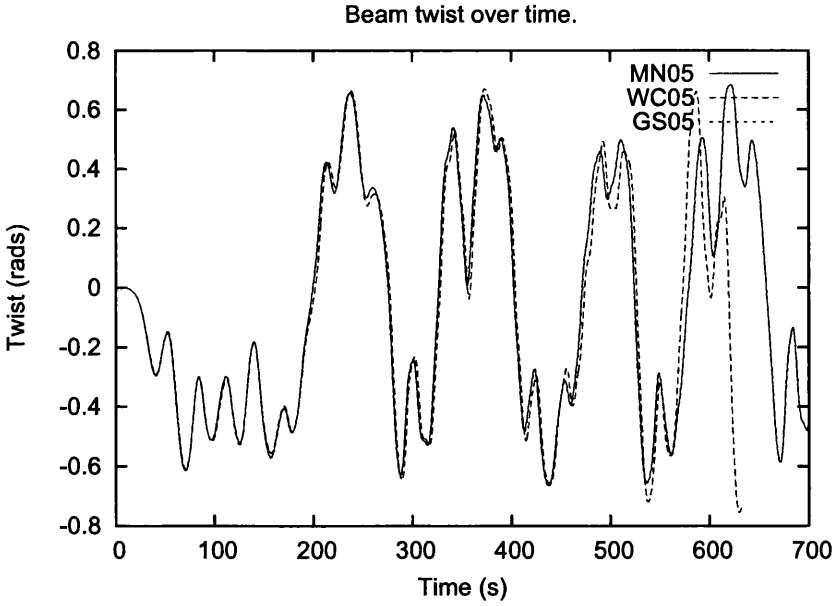

Figure 7.6: Rotation of the central cross-section of the bridge. Legend denotes the Monolithic Newton, Weakly Coupled and Gauss Seidel solutions for $\Delta t = 0.5s$.

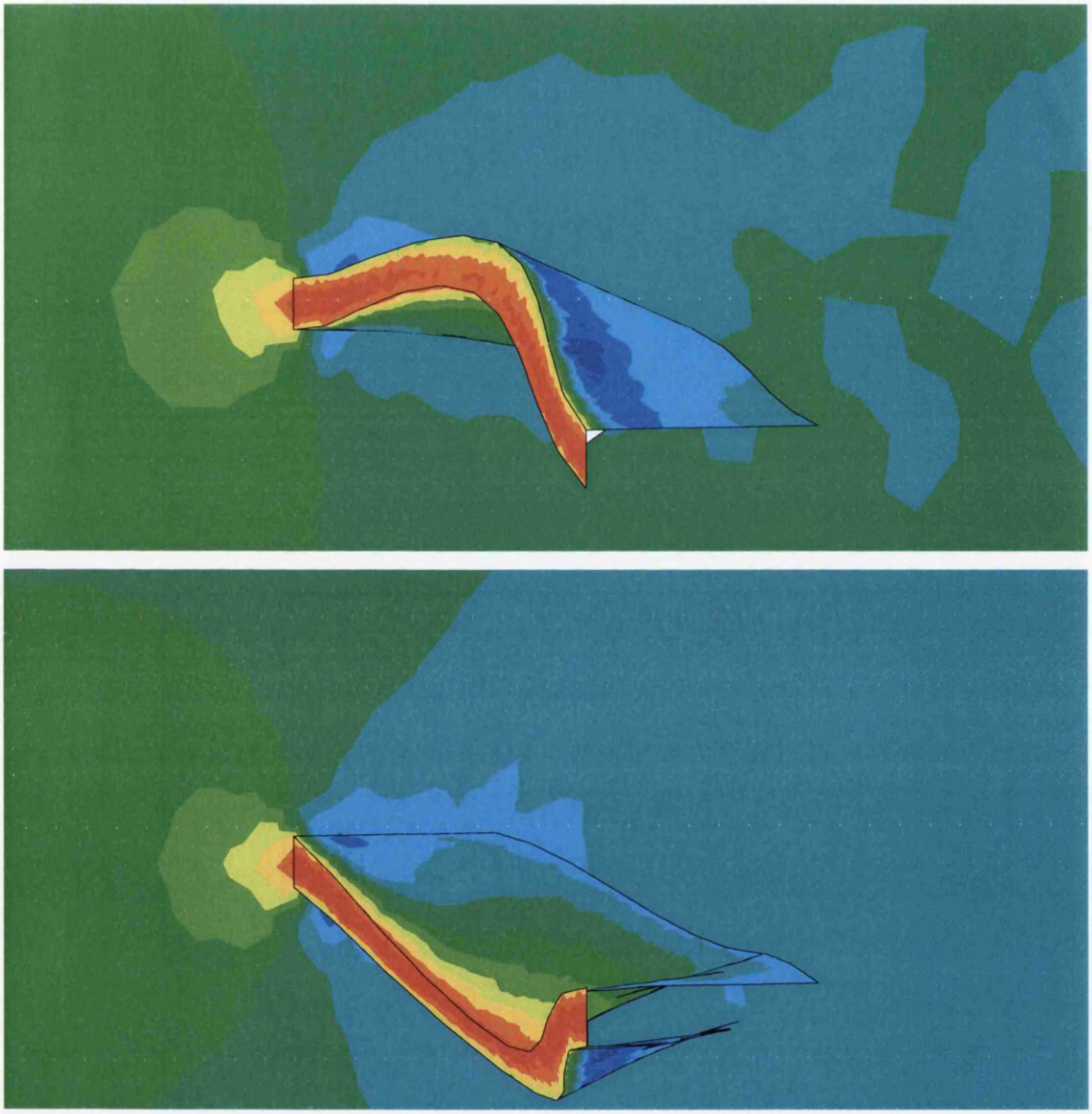

Figure 7.7: Contour plots displaying pressure on the surface of the deformed solid mesh.

Chapter 8

3-D Flexible Plate

8.1 Introduction

In the interest of modelling a more complex external flow example than the previous chapter, it was decided to construct a simulation of a thin flexible plate fixed to a rigid support. This system can be expected to behave in a very unstable manner, as the sharp angles of the rigid support should result in high levels of vorticity in the flow over the thin plate. Additionally, this example has been presented in two dimensions by Dettmer and Perić [16, 20], Wall and Ramm [61], Hübner *et al* [30] and later in three dimensions by von Scheven [53] and Kassiotis *et al* [41, 42] and as such was considered a suitable problem to test the capabilities of the 3-D solution methods employed in this study and compare to other published solution methods.

The problem itself consists of a thin, flexible solid material fully submerged in a fluid body, and fixed to a rigid rectangular beam. Far upstream from the body, a uniform inflow velocity U_∞ is applied gradually over a period of time, resulting in vortices forming on the rigid rectangular body causing the flexible plate to be displaced. In the interest of comparison with other presentations of this problem, as well as general exploration, two sets of material properties for the system were simulated using various meshes and solution methods.

8.2 Material Properties

8.2.1 Case 1: Light and Stiff

This case was based on the work presented by Dettmer and Perić [16, 20]. The fluid properties were set as having viscosity $\mu_f = 1.82 \times 10^{-4}$, density $\rho_f = 1.18 \times 10^{-3}$, and uniform flow $U_\infty = 51.3$ applied gradually from 0 over $t = [0.5 : 1.0]$, resulting in a Reynolds number of $Re = \frac{\rho_f D U_\infty}{\mu_f} = 333$. The solid parameters were set as having a density of $\rho_s = 0.1$, shear modulus $G_s = 9.92593 \times 10^5$ and bulk modulus $K_s = 2.78 \times 10^6$ corresponding to a Young's modulus $E_s = 2.5 \times 10^6$ and Poisson's ratio $\nu_s = 0.35$.

8.2.2 Case 2: Heavy

The second test case was based on the work presented by von Scheven [53] and Kassiotis *et al* [41, 42]. The fluid properties were set to $\mu_f = 1.82 \times 10^{-4}$, $\rho_f = 1.18 \times 10^{-3}$ and uniform inflow velocity $U_\infty = 100.0$ resulting in a Reynolds number of $Re = 650(648.35)$. The solid density was set to a much higher value than case 1 of $\rho_s = 2.0$. The solid bulk and shear moduli were set to $K_s = 2.223 \times 10^6$ and $G_s = 7.4074 \times 10^5$, corresponding to a Young's modulus of $E_s = 2.0 \times 10^6$ and Poisson's ratio of $\nu_s = 0.35$.

Table 8.1: Comparison of material properties

Benchmark	U_∞	Ramp	$\nu_f = \frac{\mu_f}{\rho_f}$	ρ_f	E_s	ν_s	ρ_s
Dettmer Bench	51.3	1.0	0.1542	1.18×10^{-3}	2.5×10^6	0.35	0.1
von Scheven/ Kassiotis Bench	100.0	2.0*	0.1542	1.18×10^{-3}	2.0×10^6	0.35	2.0

It should be noted that Kassiotis et. al. do not initiate the ALE strategy until $U = U_\infty$. This is done by beginning the ramp at -2s to reach full inflow at 0s.

8.3 Geometrical Properties

All of the cases investigated in this study share identical geometrical properties detailed in figures 8.1 and 8.2. The solid domain consists of a thin plate 4m long by 3m high, with a

thickness of 0.06m fixed at one end to a rigid support 3m high with width and thickness of 1m. Due to the rigid nature of the support, only the thin plate was chosen to interact with the fluid. The solid was then suspended in a fluid domain 20m by 11m by 11m.

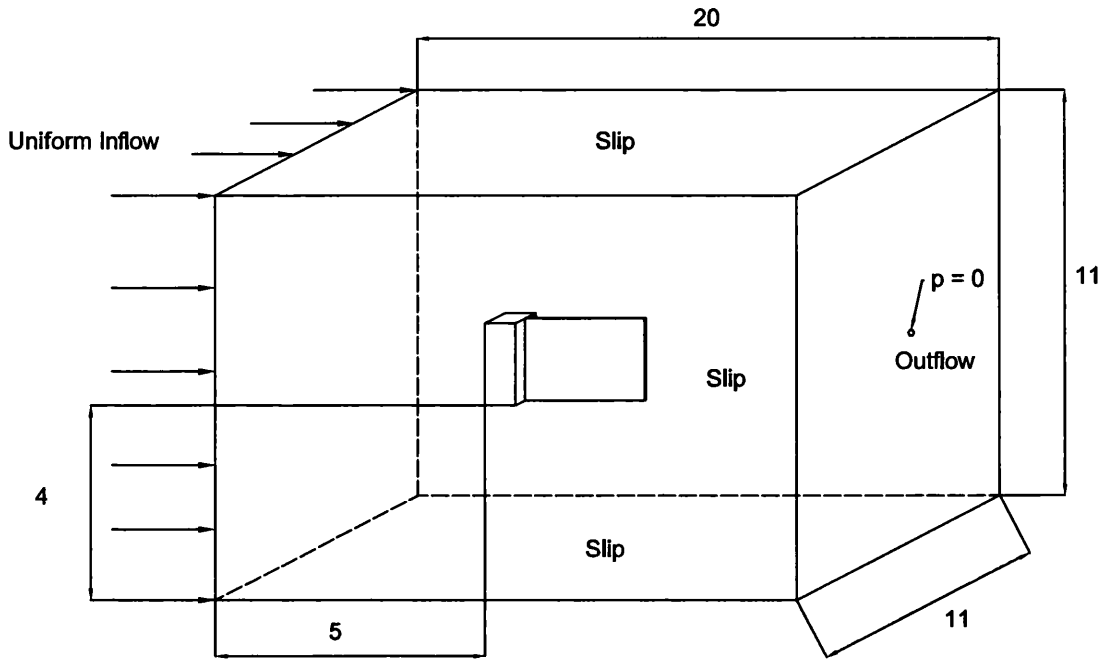

Figure 8.1: Diagram of domain boundary conditions and dimensions.

8.4 Formulation of Mesh and Boundary Conditions

The fluid body was represented numerically using both a coarse (88k elements) and a dense (166k elements) mesh of four-noded tetrahedral elements. Images of the 166k element fluid mesh are displayed in figures 8.3 and 8.4(a). In both meshes the boundary conditions applied were the same, with the inlet being fixed, one point of pressure in the outlet fixed, and all other outer boundaries slip. As mentioned previously, the rigid support was represented as fully fixed no-slip boundaries within the fluid domain, and the flexible plate chosen as the only part of the structure to be included in the FSI interface.

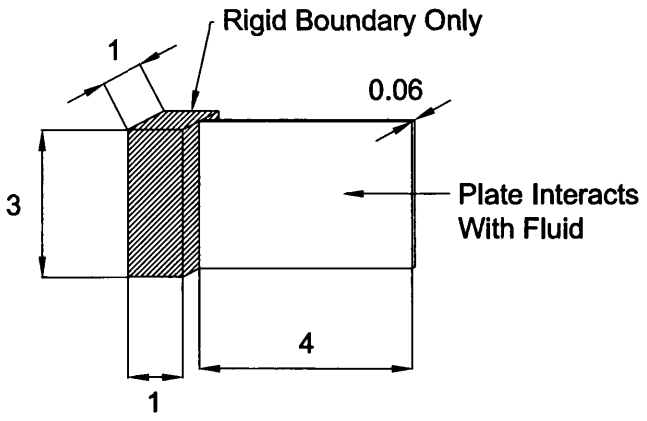

Figure 8.2: Diagram of structure boundary conditions and dimensions.

Table 8.2: Comparison of fluid mesh properties

Mesh	Incompressible Fluid Elements/Cells	D.o.f.	Solution Strategy	δt
Mpap[1]	166×10^3 Stable	751×10^3(total)	Finite Elements	0.005
Kassiotis et. al.	290×10^3	1159×10^3	Finite Volume	0.001
von Scheven	200×10^3	794×10^3 (total)	Finite Elements	0.01

Due to the slender nature of the solid geometry being considered, special care was taken in selecting which type of solid elements were to be used to represent the behavior of the plate. It was therefore decided to conduct a solid-only analysis of the undamped natural frequency of vibration of the plate represented by a variety of solid element types and compare the values obtained to the analytical solution for the natural frequency of a cantilever beam.

Three solid mesh configurations were analysed in this manner, consisting of: an 8-noded Fbar solid mesh of 600 elements, and two 20-noded quadratic solid element meshes of 300, and 2400 elements respectively. Both the 8-noded Fbar and the dense 20-noded quadratic meshes contain two layers of elements in the thickness of the plate, while the coarse 20-noded quadratic mesh consists of only one layer. Additionally, as mentioned previously,

[1]Note that "Mpap" is an abbreviation of "Multiphysics Analysis Program" used to denote the solvers employed in this work as a group for the sake of brevity.

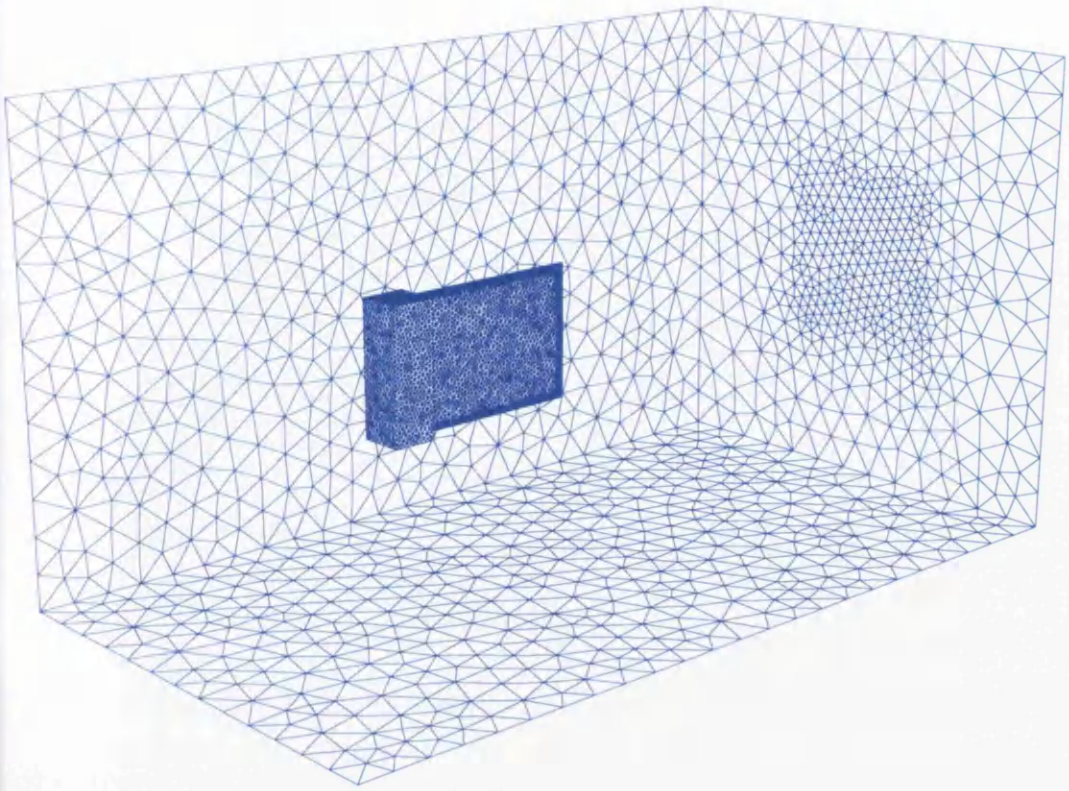

Figure 8.3: Image of the 166k element fluid mesh domain.

all solid elements considered employ the Neo-Hooke elastic behavior model.

Table 8.3: Comparison of results for solid only test case.

System	Frequency of Oscillation
Analytical Rayleigh calc. for solid only f_n	0.6057, 3.687
Mpap 8N FBar Solid Only 600 ele	1.2
Mpap 20N Solid Only 300 ele	0.62
Mpap 20N Solid Only 2400 ele	0.62

It can be seen from the results presented in table 8.3 that the 20-noded quadratic elements behave in a manner that compares favorably with the analytical solution for the first mode of vibration, resulting in a relative error of 2.36%. Due to the identical behavior of the two meshes using this element type and in the interest of reducing computational cost, the 300 quadratic element mesh was selected to be employed throughout the remainder

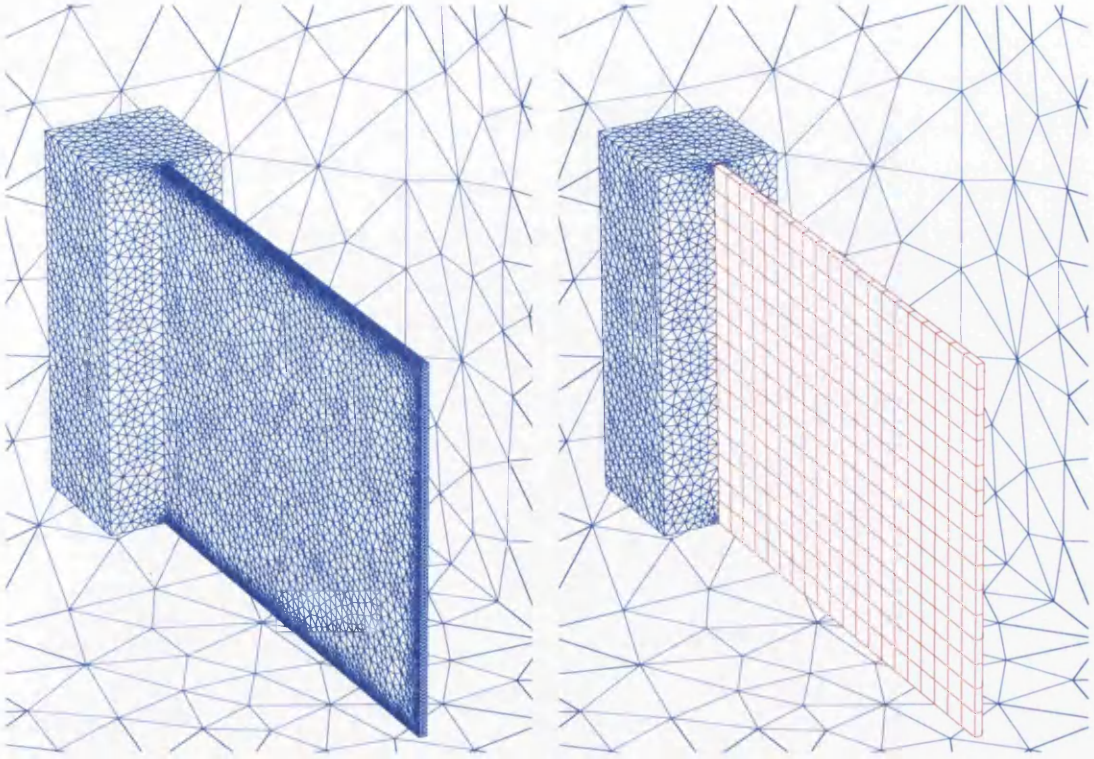

Figure 8.4: Images detailing the 166k element fluid mesh density on the interface, and the 300 element 20N solid mesh.

of this study. An image of this mesh is displayed in figure 8.4(b).

Table 8.4: Comparison of solid mesh properties

Mesh	Solid Elements	D.o.f.	Solution Strategy	Coupling Strategy
Mpap	300 20-Noded Quadratic	n/a	NeoHooke Elasticity	MN / GS / WC
Kassiotis et. al.	300 27-Noded Quadratic	7425	St.-Venant-Kirchhoff	DMFT-BGS with Aitken relaxation
von Scheven	432 7 Parameter Shell	n/a	St.-Venant-Kirchhoff	Block Gauss-Seidel with Aitken relaxation

8.5 Analysis of Simulations

It should be noted that all nodal deflections presented in this section are of the free end of the flexible plate. Where necessary, results relating to the top, middle, and bottom of the plate will be specified.

8.5.1 Case 1: $U_\infty = 51.3, E_s = 2.5 \times 10^6$

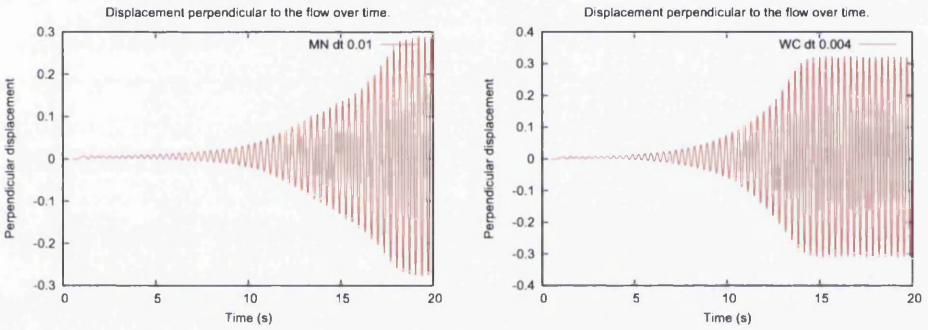

Figure 8.5: 88k fluid mesh with 20N quadratic solid elements. Legends identify Monolithic Newton and Weakly Coupled solutions as well as time step size.

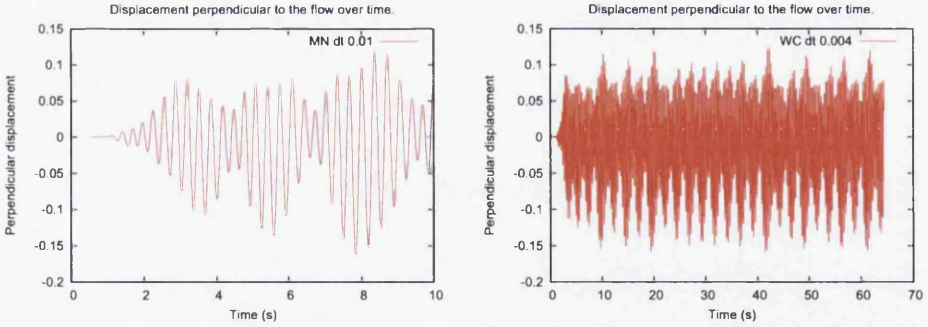

Figure 8.6: 166k fluid mesh with 20N quadratic solid elements. Legends identify Monolithic Newton and Weakly Coupled solutions as well as time step size.

In all simulations investigated in this case it can be seen that the steady flow parallel to the plate eventually results in a steady oscillating response in the solid, presenting behavior which agrees with the known phenomena of vortex induced vibration. Due to the high computational cost of the monolithic Newton and block Gauss-Seidel solvers,

simulations employing these solution techniques were limited to a lower simulation time interval than simulations employing the novel staggered solution method. Figure 8.6(b) shows that a steady-state response of the solid mesh is reached by approximately 10s of simulation time. It was therefore decided to restrict the interval considered for the analysis of the three solvers to 10s (2500 time steps at $\Delta t = 0.004$).

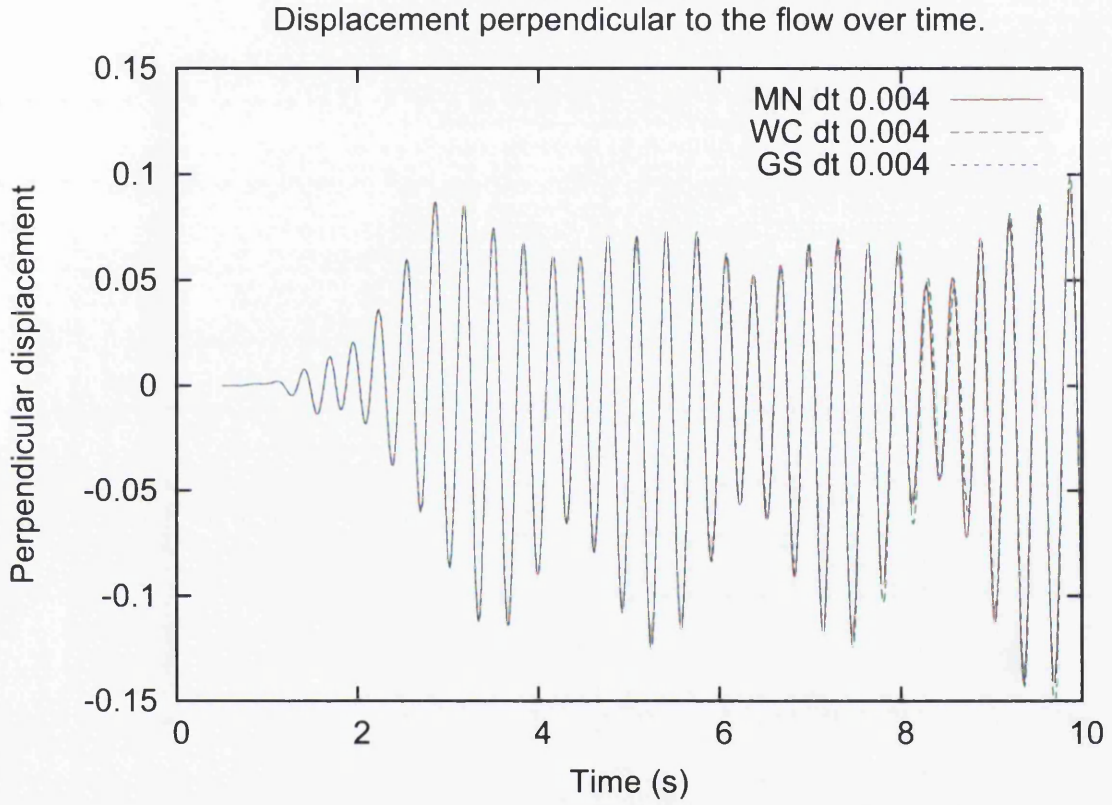

Figure 8.7: 166k fluid mesh with 20N quadratic solid elements. Legend identifies Monolithic Newton, Weakly Coupled, and Gauss Seidel solutions as well as time step size.

Figure 8.7 displays a strong agreement between the solution methods considered, which is consistent with the results obtained from the analysis presented in Chapter 7. Due to the consistency of the results obtained and in the interest of performing a higher number of simulations during the time interval of this work, the novel staggered scheme was selected as the primary solution technique employed for the remainder of this study, with the monolithic Newton solver employed to justify the accuracy of results.

Table 8.5: Comparison of solutions.

Analysis	Amplitude	Frequency
2D	2.8	1.6
3D Coarse 88k mesh	0.6	3.0
3D Dense 166k mesh	0.29	3.5

Table 8.5 highlights the differences of the two dimensional results presented in Dettmer and Perić [16, 20] with the three dimensional results obtained in this study. It is possible that this may be a result of the two dimensional model problem being an idealisation of the three dimensional case, requiring the length of the plate in the dimension not accounted for to be assumed as infinitely long. It is to be expected that the presence of steady flow above and below the flexible plate would have a significant impact on the behavior of both the fluid and solid bodies considered. As an additional supporting argument for the three dimensional results it should be noted that the frequency of oscillation presented by the 166k fluid mesh simulation (3.5) agrees quite strongly with the analytical result for the second mode of vibration for the cantilever plate (3.687). This second modal response of the solid mesh would account for a reduction in the maximum amplitude of oscillation of the free end of the plate.

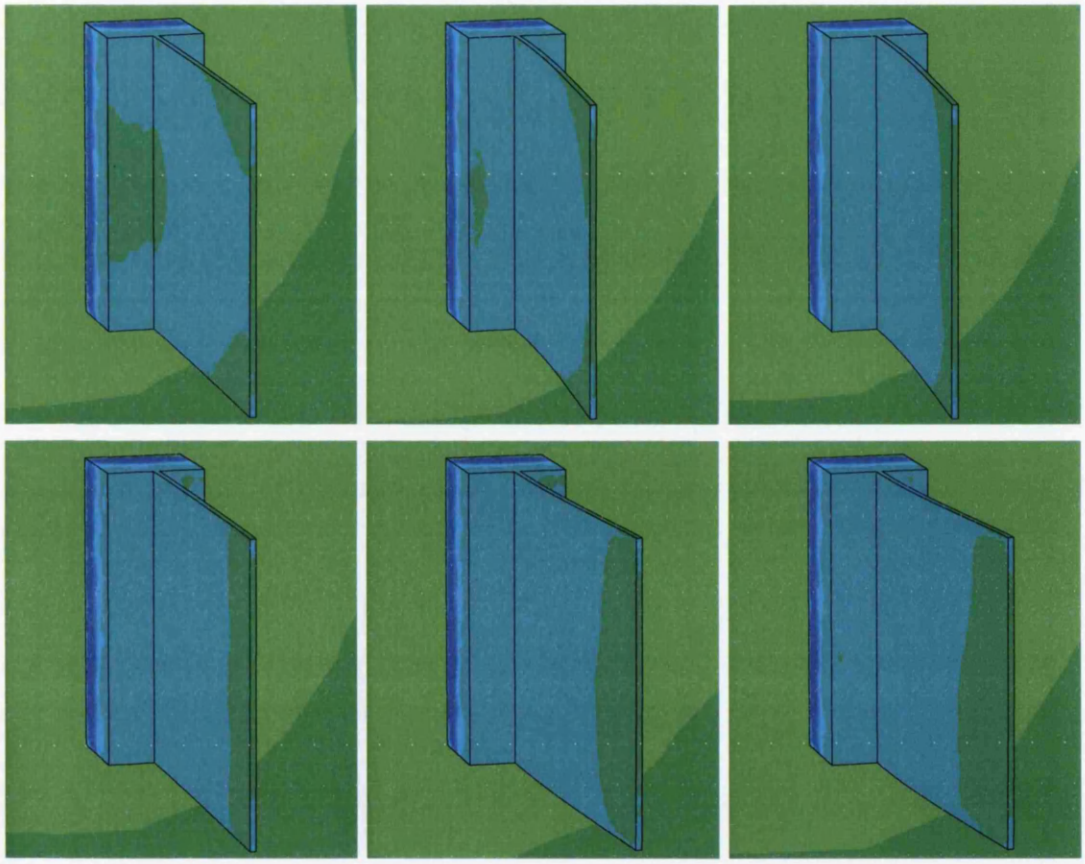

Figure 8.8: Images of countour plots detailing pressure acting on the surface of the deformed mesh.

8.5.2 Case 2: $U_\infty = 100.0, E_s = 2.0 \times 10^6$

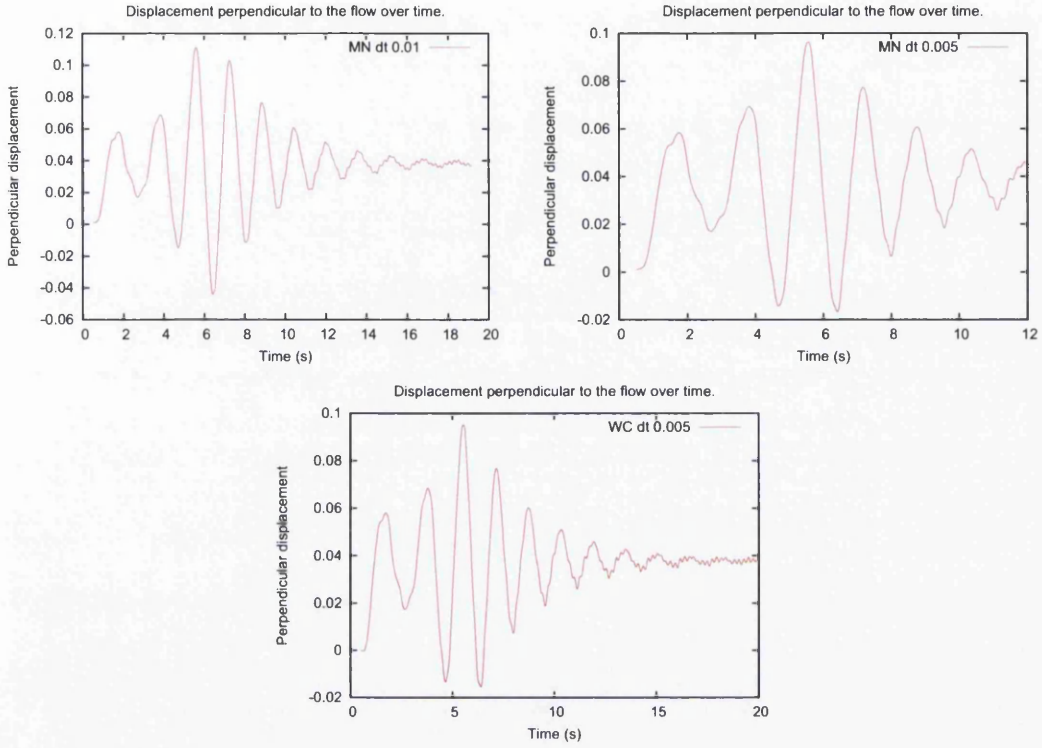

Figure 8.9: All figures above on 88k fluid mesh with 20N quadratic solid elements. Legends identify Monolithic Newton and Weakly Coupled solutions as well as time step size.

Figures 8.9 and 8.10 display the results obtained from the simulations performed on the coarse and dense fluid meshes respectively. On the coarse mesh the displacement of the flexible plate damps down to 0 after the initial disturbance with strong agreement between the monolithic Newton and novel staggered solutions, while on the dense mesh the plate responds both in lateral displacement and torsion. This behavior is indicative of the complex nature of the fluid flow being modelled, and it may therefore be observed that the coarse mesh is not capable of fully discretising the flow around the complex geometry of this model problem. Additionally, the multimodal response of the flexible plate is a clear indication of the unstable nature of the model problem with this set of system properties. As such, any difference in the model solution may be expected to result in a significant difference in solid response. This behavior is further highlighted by the disagreement of the 8-noded solid mesh and 20-noded solid mesh solutions presented in figure 8.10: col(a)

and col(b) respectively.

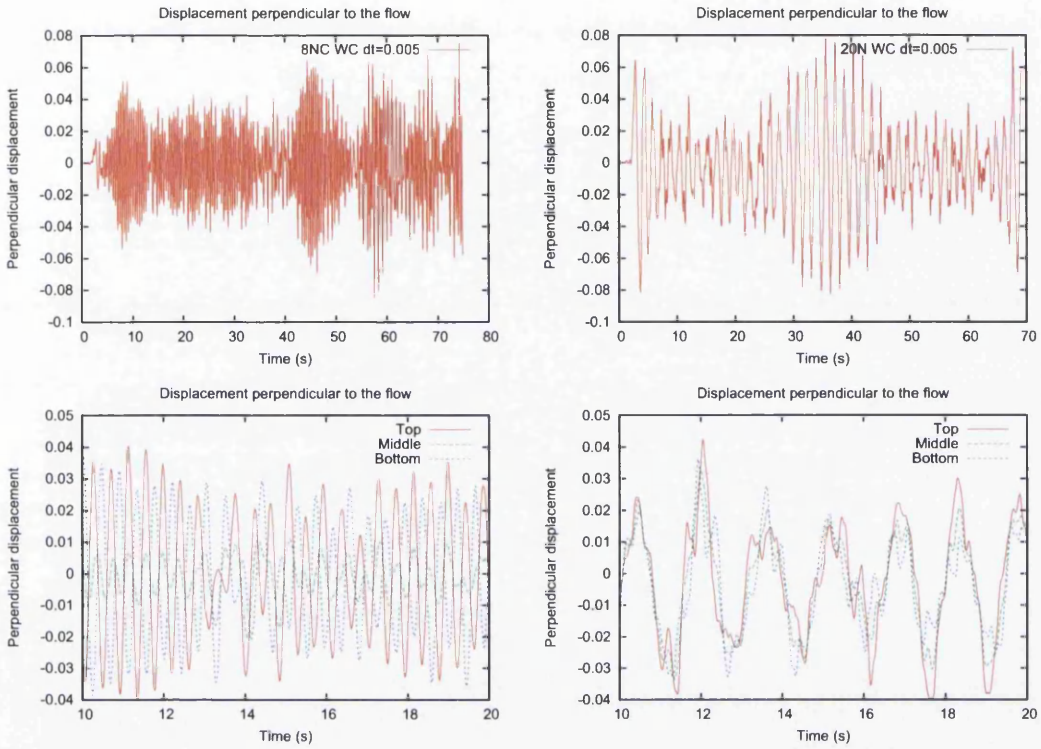

Figure 8.10: Figures above on 166k fluid mesh. First column: 8-noded solid mesh, second column: 20-noded solid mesh. Legends identify solid mesh density used to obtain the Weakly Coupled solution as well as time step size.

A summary of the results obtained for this test case, along with those presented by von Scheven [53] and Kassiotis *et al* [41, 42] is presented in table 8.6. It can be seen that full agreement is not present between any of the presentations of this model problem. However, it should be noted that the plate behavior presented by Kassiotis *et al* is of the second mode of translational displacement with no torsional rotation, while the results obtained in this work and those presented by von Scheven exhibit both translational and torsional responses in the solid. As was established previously in this section, the model problem being considered is highly unstable and is prone to transition between translational and torsional modes of response. As such, it is the belief of the author that the magnitude of the disagreement between the different presentations of this solution does not fully reflect the difference in accuracy of the various solution techniques employed. Additionally, it must

be mentioned that the time intervals considered in the solutions presented by von Scheven and Kassiotis *et al* may not be sufficient to describe the final fully-realised response of the system.

Table 8.6: Comparison of results for second test case.

System	Frequency of Oscillation	Amplitude of Oscillation	Time Interval
Kassiotis e. al. FSI	4.0	0.5	6s
von Scheven FSI	0.9 or 10 (2 modes)	0.1	12s
Mpap 88k Fluid, 20N Solid	1.1	0.05 (damped to 0)	20s
Mpap 166k Fluid, 8N Fbar Solid	2.1*	0.07	75s
Mpap 166k Fluid, 20N Solid	0.7*	0.08	70s

*In both cases for the 166k mesh, the vibration of the solid consists of both lateral displacement and torsional rotation. The linear solid mesh experiences more torsion than the quadratic solid and thus experiences both a smaller amplitude and higher frequency. It should also be noted that there is strong agreement between the monolithic Newton and weakly coupled solvers.

Chapter 9

3-D Tube FSI

9.1 General Description of Problem

In order to present a suitable internal flow FSI model problem, a simple 'flow through a flexible pipe' model was chosen. As discussed previously, there is currently a shortage of well established benchmarks in the area of three dimensional fluid-structure interaction, however, Dettmer and Perić [21] present this problem in two dimensions, and similar three dimensional internal flow simulations have been presented by Hron and Turek [29], and Bazilevs *et al* [2]. Setting up this problem posed some interesting challenges in several areas. Considering that this was effectively the first time this particular model was to be simulated, special care had to be taken when choosing the geometry, material properties, and boundary conditions.

9.2 Constructing the Model Problem

It was decided that the model problem would consist of a long slender elastic tube with a sinusiodal internal flow, parabolic at the inlet. In the interest of having a very slender pipe, the length of the tube was set to 50 times the internal radius. It was also decided that the ratio of external radius to internal radius would be $\sqrt{2}$, resulting in the fluid and solid domains having equal cross-sectional area. By choosing an internal radius of 1, an external radius of $\sqrt{2}$ and length of 50 were obtained.

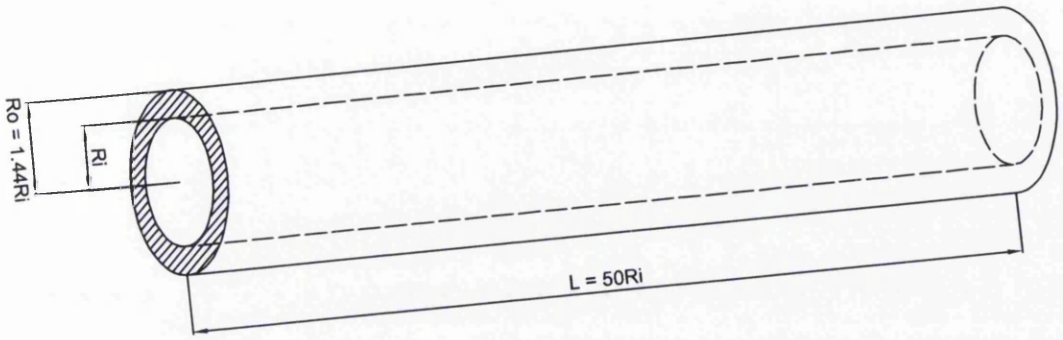

Figure 9.1: Diagram of geometrical ratios.

A fluid mesh was then constructed, consisting of unstructured four-noded tetrahedral elements with a higher mesh density towards the interface boundary on the outer edges of the fluid cylinder, and coarser elements towards the centre of the fluid domain, resulting in a mesh of $7.6 \cdot 10^4$ stabilised incompressible fluid elements, as displayed in figure 9.2.

The solid mesh consisted of structured eight-noded linear elements with three divisions on the radial length, twenty four along the circumference and one hundred along the length resulting in mesh consisting of 7200 NeoHooke Elastic solid elements, as displayed in figure 9.3.

Figure 9.2: Image of the fluid mesh domain.

The interface nodes were identified by interpolating between the internal surface nodes

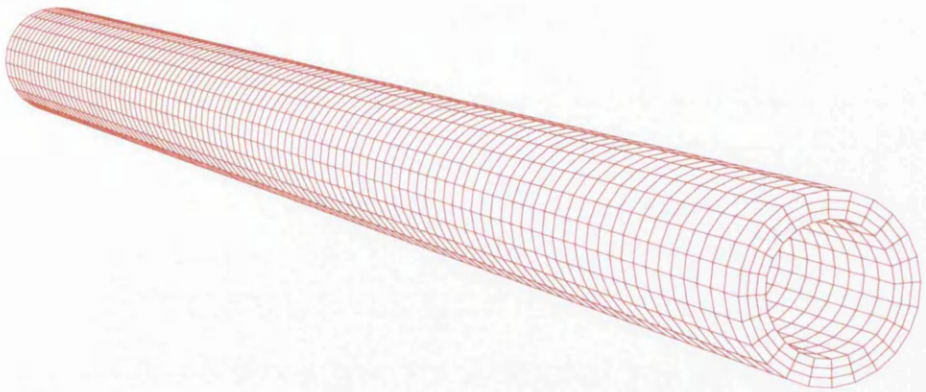

Figure 9.3: Image of solid mesh configuration.

of the solid mesh in order to identify all of the fluid nodes in contact with the solid boundary. Once this was completed, the final system was assembled with the fluid boundaries set as fixed at the inlet, joined to the solid mesh at the interface, and free at the outlet with one point fixed in pressure. The solid mesh was fixed at the inlet, and fixed in the axial direction at the outlet in the interest of negating any displacement in the axial direction. This was done in order to ensure that any solid deflection would be in the radial direction. Figures 9.4 and 9.5 detail the boundary conditions described.

9.2.1 Test Case 1

As an initial test of the solver's ability to handle internal flow, an arbitrary set of fluid material parameters were chosen as $\rho_f = 1.0$, $\mu_f = 0.01$, and parabolic inflow with maximum velocity $U_\infty = 2.0$. This inflow was applied sinusoidally, oscillating between 0 and U_∞ with a period of $t = 20s$. The solid material parameters were chosen as $K_s = 7.2 \cdot 10^4$, $G_s = 3.2 \cdot 10^4$ equating to a Young's modulus of $E_s = 8.36 \cdot 10^4$ and Poisson's ratio $\nu_s = 0.306$.

9.2.2 Test Case 2

The second test case consisted of the same fluid properties as Case 1, however the solid stiffness was reduced by a factor of roughly twenty, resulting in $K_s = 3600$, $G_s = 1800$

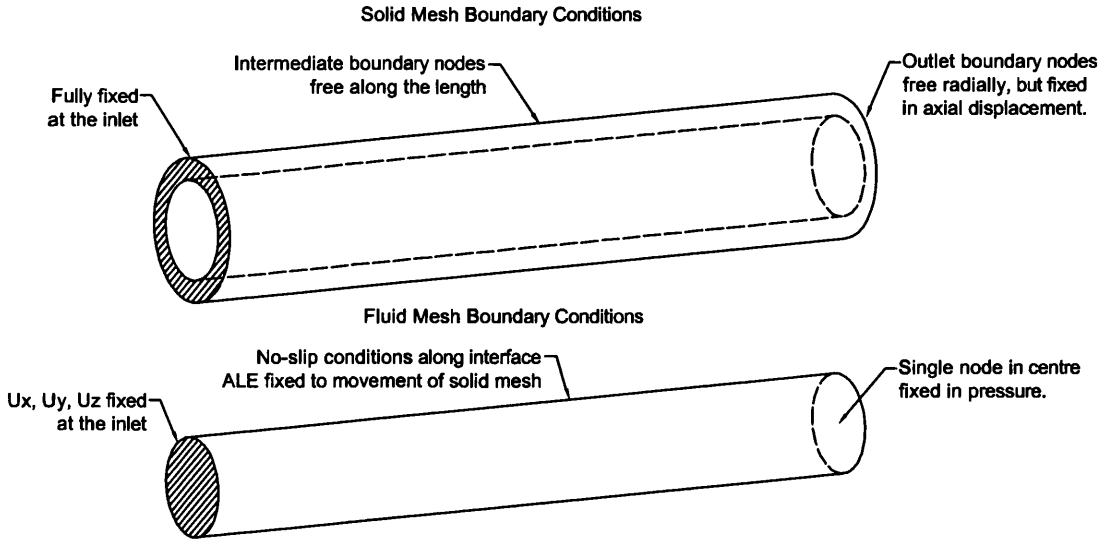

Figure 9.4: Diagram of boundary conditions.

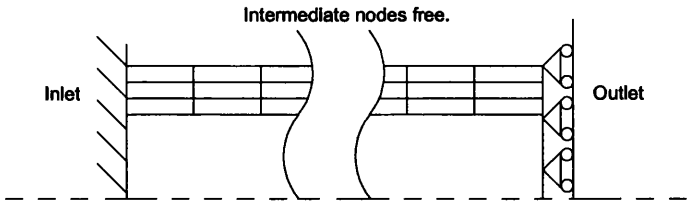

Figure 9.5: Details showing nodes fixed in axial deflection, but free to deform radially.

equating to a Young's modulus $E_s = 4628.5$ and Poisson's ratio $\nu = 0.286$. Additionally, the inflow was set to the same sinusoidal oscillation as Case 1, however the maximum inflow velocity U_∞ was set to increase by 2.0 every 80 seconds of simulation time, up to a maximum value of $U_\infty = 8.0$.

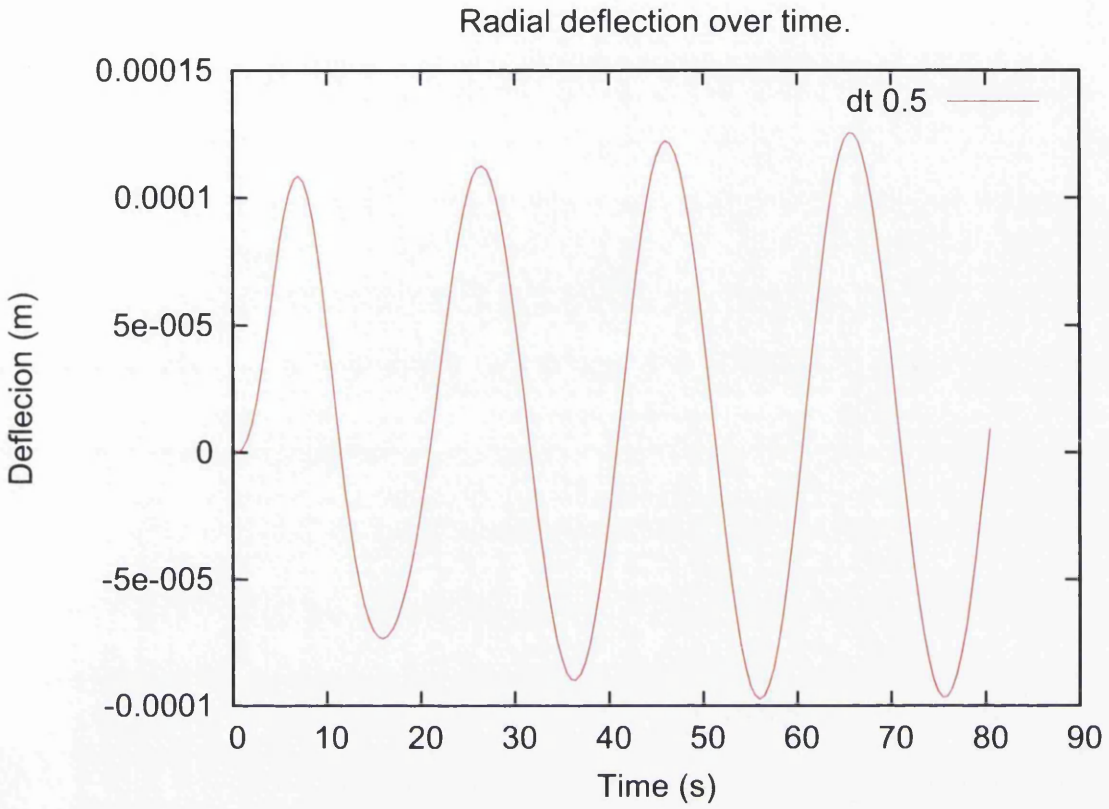

Figure 9.6: Radial deflection over time at outlet for Case 1. Legend indicates time step size employed in analysis.

9.3 Determining a Resonant Case

From the results obtained displayed in figures 9.6 and 9.7 it may be concluded that the system configurations of the test cases do not result in any significant response of the elastic pipe, and that greater care must be taken in forming a three dimensional model problem. Therefore, it was decided to first choose a set of fluid and solid material parameters $\rho_f = 1.0$, $\mu_f = 0.01$, $\rho_s = 1.0$, $K_s = 5000$, $G_s = 100$, $E_s = 298$, $\nu_s = 0.49$, and then determine the values for U_∞ and T that would induce a significant response in the solid. By setting the inflow velocity to an adequate magnitude oscillating at a non-resonant frequency of the pipe, a suitable steady-state response of the pipe would be achieved.

The principle of standing waves with reference to acoustic resonance of a fluid in an

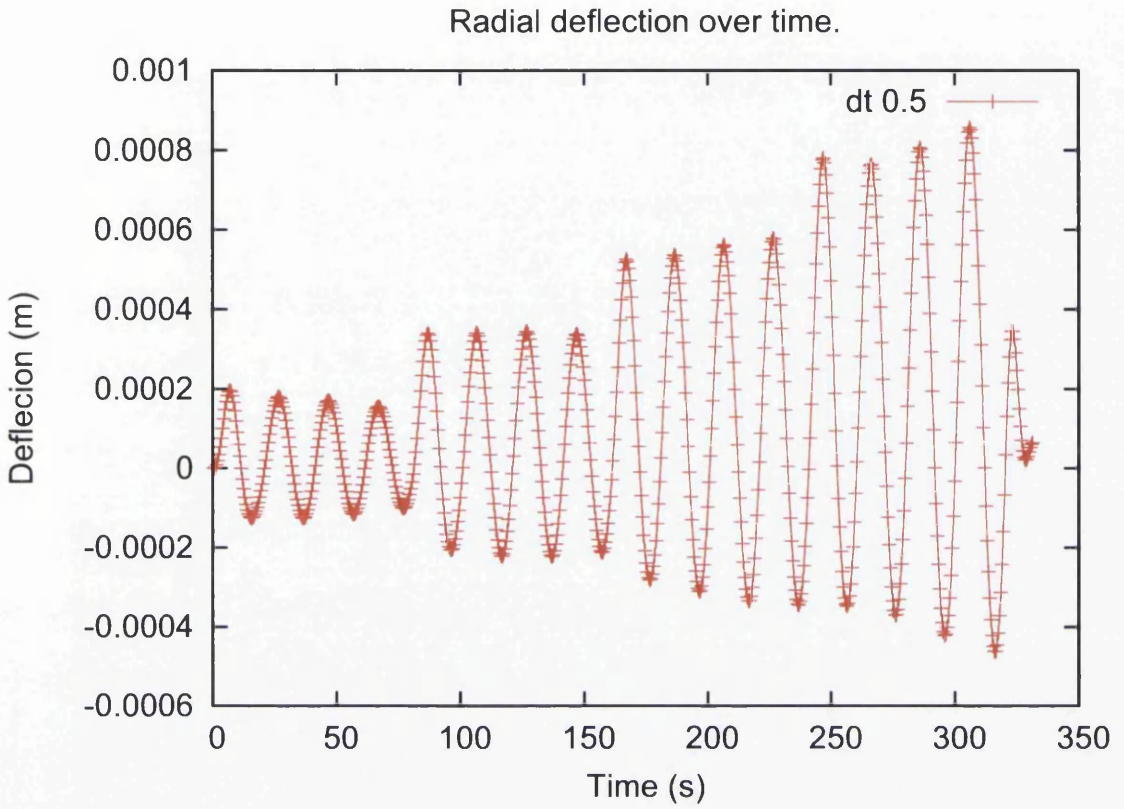

Figure 9.7: Radial deflection over time at outlet for Case 2. Legend indicates time step size employed in analysis.

open pipe equates the resonant frequency of the wave to the speed at which a vibration travels through the fluid, conventionally referred to as the speed of sound in the medium as described by such texts as Kinsler and Frey [43]. This equation may be written as:

$$f_a = \frac{nv}{\lambda}, \lambda = 2L. \tag{9.1}$$

Where n is the integer mode of resonance, v is the speed of sound in the medium, λ is the wavelength of the vibration and L is the length of the open pipe. By applying this principle to set up a standing wave between the periodic inflow of the fluid and the reactive vibration in the solid it is possible to determine a set of inflow parameters resulting in a resonant solid response. This resonant case may then be modified by altering the inflow frequency in order to achieve a significant steady-state response in the solid. In order to

achieve this it was necessary to first determine the speed of sound in the solid. This was done by constructing a numerical simulation consisting of the solid mesh only subjected to a radial deflection at one end. This radial deflection was then released, and the rate at which the resulting vibration travelled through the solid was recorded. This value for $v_s = 16.667$ was then inserted into equation (9.1) in order to obtain the resonant frequency $f_a = 0.167$. However, the focus of this work was to be on Reynold's numbers below the order of $Re = 10^3$, and an inflow velocity of $U_\infty = 16.667$ would result in a Reynold's number of $Re = 1667$. It was therefore decided to reduce the scale of the solid geometry by a factor of 10, resulting in a corresponding factor 10 reduction of the Reynold's number and increase in resonant frequency while allowing all other properties to remain unchanged. As a final check for these values, a numerical simulation was set up, consisting of the solid mesh only subjected to a periodic radial force equivalent to the pressure of a periodic fluid inflow with $U_\infty = v_s$ and $f = f_a$. This equivalent force was calculated using Bernoulli's equation for incompressible flow to determine the fluid pressure acting on the solid:

$$F = \frac{1}{2}\rho_f U_\infty^2 A_n \tag{9.2}$$

Where A_n is the area of fluid pressure acting on the solid associated with each radial node of the solid.

Figure 9.8 displays the resonant response of the solid subjected to the forces calculated using equation (9.2). It can be seen that after a sufficient period of time the vibrating response of the solid propagates throughout the entire length of the pipe and the radial deflection reaches magnitudes as large as double the original internal radius. Having confirmed that this particular loading condition results in a resonant response, it follows that a full FSI simulation constructed with an inflow velocity of $U_\infty = 16.667$ oscillating at a frequency non-harmonic to $f_a = 1.67$ would display a suitable steady-state response in the solid.

9.4 Fully 3-D case (Aneurism)

Following the construction of a resonant case, it was decided to increase the complexity of the simulation by the creation of an asymmetric solid structure. It was therefore decided

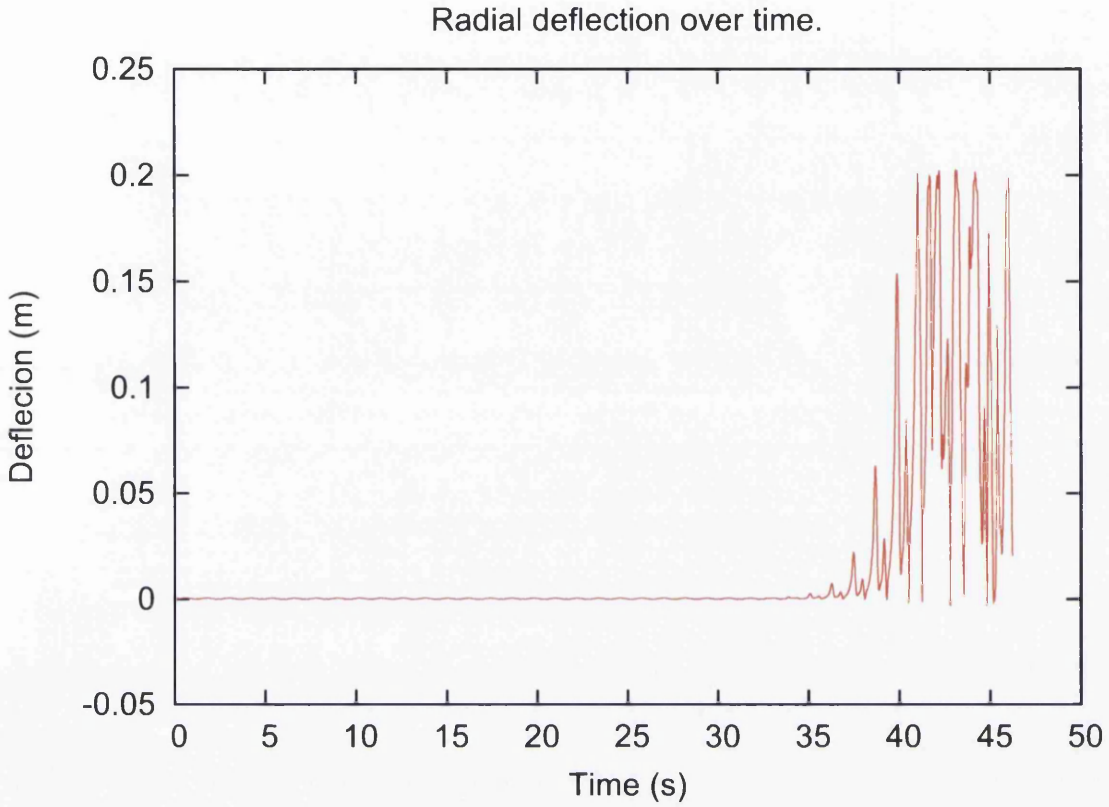

Figure 9.8: Radial deflection over time at "outlet" of solid-only simulation showing resonance.

to model a rough approximation of an aneurism by creating a weakened portion of the solid mesh. The resulting "weak patch" was located at the centre of the pipe, 0.5m long and spanning half of the circumference of the pipe as described by figure 9.9. The material properties of the solid were set to the same values used to determine a resonant case, with $\rho_s = 1.0$, $K_s = 5000$, and $G_s = 100$ equating to a Young's modulus of $E_s = 298$ and Poisson's ratio $\nu_s = 0.49$. The density of the "weak patch" was set to the same value as the rest of the solid, however, the material properties were set to half that of the surrounding solid, resulting in the values of $K_{patch} = 2500$ and $G_{patch} = 50$ equating to $E_{patch} = 149$ and $\nu_{patch} = 0.49$. The fluid properties were set to $\rho_f = 1.0$ and $\mu_f = 0.01$, with parabolic inflow velocity oscillating between 0 and $U_\infty = 16.667$. Selecting an inflow frequency of $f = \frac{f_a}{2} = 0.833$ results in a fluid inflow that is non-harmonic with the frequency calculated using acoustic resonance but may still be expected to produce a significant response in the

new solid structure.

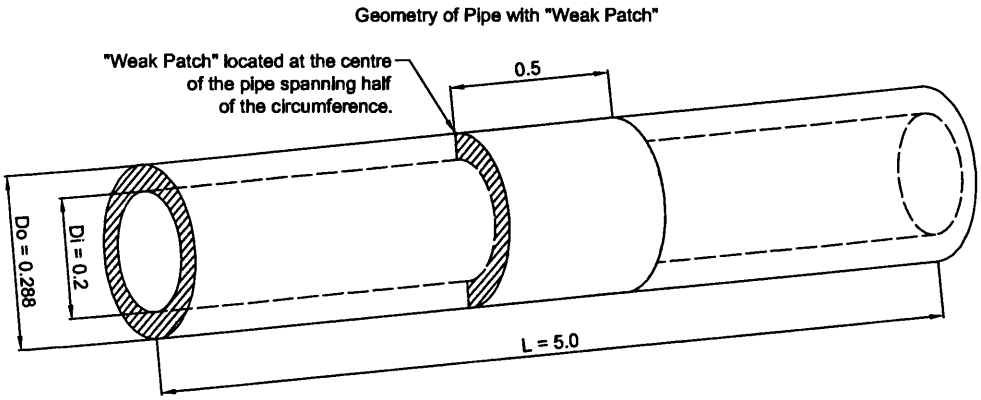

Figure 9.9: Diagram of geometry of asymmetrical flexible pipe.

The solid boundary conditions selected were similar to those of the previous test cases shown in figures 9.4 and 9.5, with the inlet being fully fixed, and the outlet being free to deform radially but fixed in the axial direction. In anticipation of the asymmetric loading conditions expected to be acting on the pipe, it was decided to also fix the outlet in translation in such a way as to still allow radial deflection. This was done by fixing the nodes falling on the axes in their respective perpendicular axial directions as described by figure 9.10.

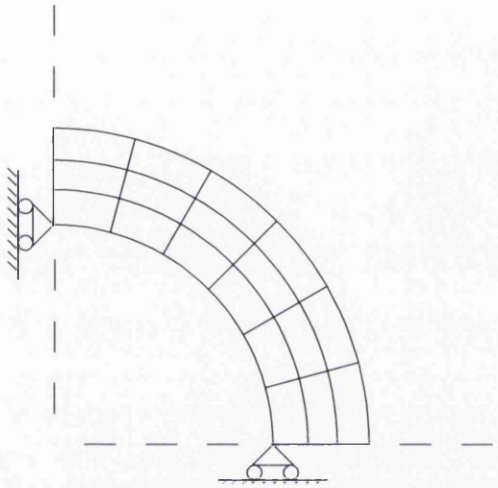

Figure 9.10: Diagram of outlet boundary conditions of asymmetric flexible pipe.

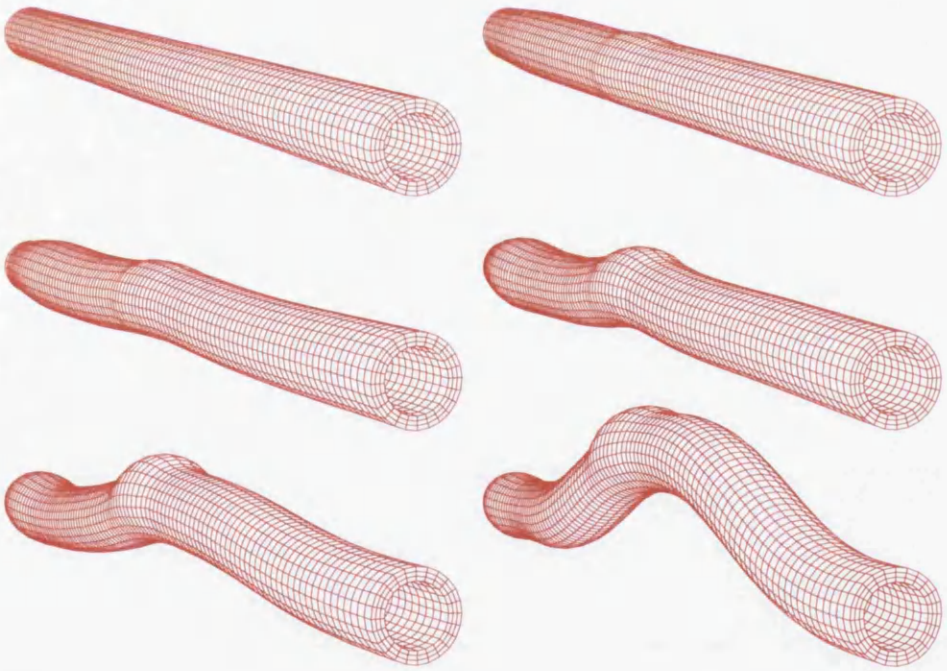

Figure 9.11: Solid mesh behavior of the weakened pipe with inner solid boundary free.

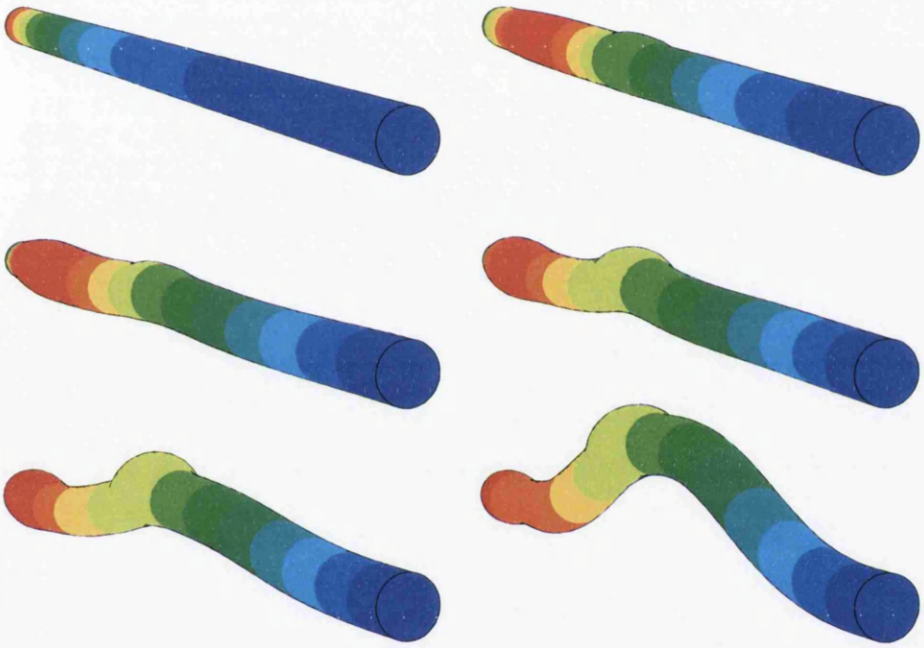

Figure 9.12: Fluid pressure in the weakened pipe with inner solid boundary free.

Figures 9.11 and 9.12 highlight the fact that this set of boundary conditions provides insufficient support along the length of the pipe, resulting in lateral bucking rather than the desired radial deformation. To solve this, a new set of boundary conditions was applied in which the solid boundary conditions at the outlet were applied throughout the entire length of the pipe, as displayed in figure 9.13. This new set of boundary conditions successfully resulted in the radial only response of the solid, as shown in figures 9.14 and 9.15. As may be expected when considering the nature of the solid structure, the majority of the solid response to the fluid is located at the "weak patch", with the rest of the solid maintaining a relatively constant cross-sectional area. In addition to the very significant deformation of the "weak patch" a relatively minor radial deflection of the solid was observed upstream of the "patch".

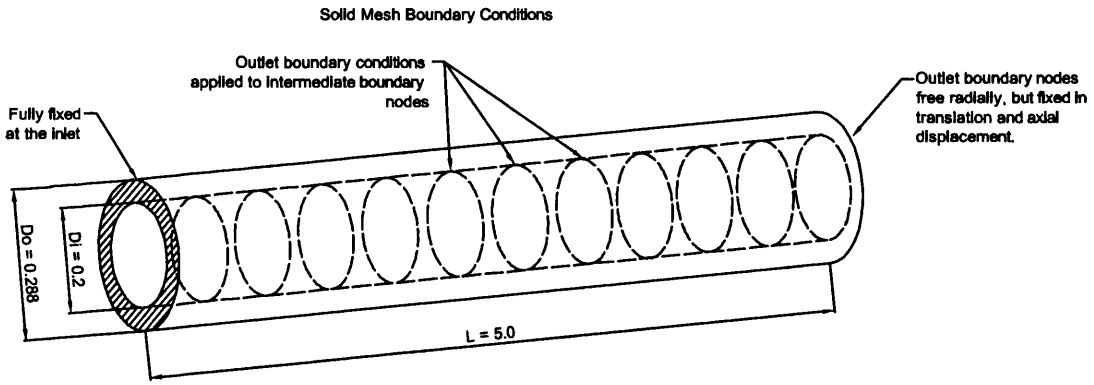

Figure 9.13: Diagram of final boundary condition configuration.

Figure 9.14: Solid mesh behavior of the weakened pipe with inner solid boundary translation fixed.

Figure 9.15: Fluid pressure in the weakened pipe with inner solid boundary translation fixed.

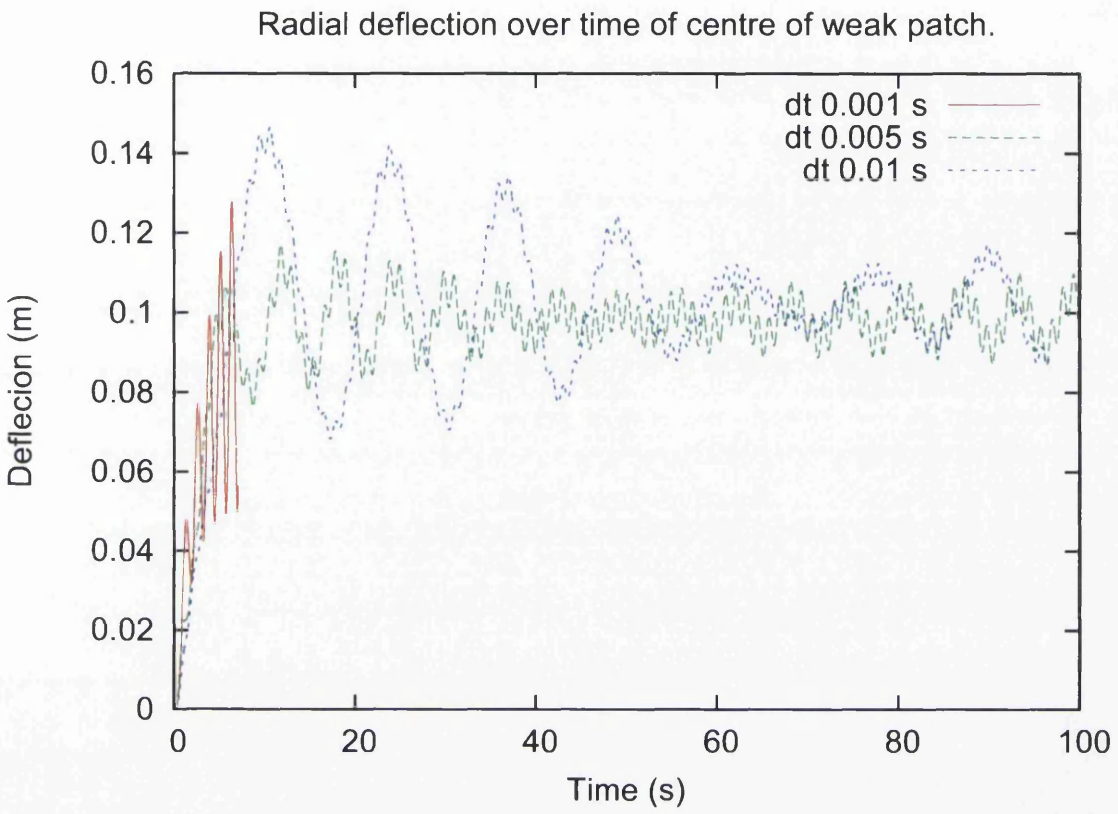

Figure 9.16: Radial deflection over time of central point in weak patch. Legend indicates time step size employed in analysis.

Figure 9.16 displays the results obtained by solving this model using the novel staggered scheme with various time step sizes. It should be noted that the solution weighted average parameter β was set to a value very close to 0 ($\beta = 0.00005$) in anticipation of difficulties in solving for the solid over fluid mass ratio of 1. This sacrifice in accuracy may account for the solution failing to converge using a time step size of $\Delta t = 0.001$.

Due to the time constraints of this work and the high computational cost of this simulation, a more in-depth study of solving this model to a higher degree of accuracy was not performed. However, a quantitative comparison with a known analytical solution to an alternate internal flow model problem is presented in Chapter 10.

Chapter 10

3-D Hose FSI

10.1 Analytical Solution and Selection of Material Properties

A classic example of an internal flow fluid-structure interaction problem is the onset of translational instability in a cantilever pipe caused by the internal flow reaching a critical velocity, at which the traction forces from the fluid overcome the inertia and stiffness of the solid pipe. This instability can result in large scale deformations with amplitudes of oscillation reaching higher than 50% of the length of the pipe. Some commonly known examples of this would be a fireman's hose needing to be restrained by hand, or even a common garden hose with the pressure too high. Not only is solving this problem useful from an industry standpoint, as such deformations could be catastrophic if not taken into account during design of cantilever pipes, but it is also very useful for the purpose of this investigation due to the existence of an analytical solution, as presented in Blevins [5]. This presents an opportunity for comparison in order to gauge the relative accuracy of the monolithic Newton solution scheme employed within this work. The purpose of this chapter is therefore to set up a numerical model problem based on material properties obtained using the analytical solution and then solve for a range of steady inflow velocities in order to obtain the numerical critical velocity for the onset of instability.

In Chapter 10.1.2 of 'Flow Induced Vibration' by Blevins [5], the analytical solution to the critical flow velocity for onset of instability in a cantilever pipe is derived by the forma-

tion of the equation of motion for the free transverse vibration of a straight, tension-free fluid conveying pipe. This is done by first applying the equilibrium of small deformations in the y direction to obtain

$$F - pA\frac{\partial^2 Y}{\partial x^2} = \rho A\left(\frac{\partial}{\partial t} + \nu\frac{\partial}{\partial x}\right)^2 Y, \quad \frac{\partial Q}{\partial x} + T\frac{\partial^2 Y}{\partial x^2} - F = m\frac{\partial^2 Y}{\partial t^2}. \tag{10.1}$$

where F is the pressure force per unit length of the pipe walls acting on the fluid, T is the longitudinal tension in the pipe, m is the mass per unit length of the empty pipe, Y is the transverse displacement of the pipe, and Q is the transverse shear load acting on the pipe related to the deformation and bending moment M_b of the pipe by

$$Q = -\frac{\partial M_b}{\partial x} = -EI\frac{\partial^3 Y}{\partial x^3}. \tag{10.2}$$

Combining these equations to eliminate F and Q, and applying the outlet boundary condition $pA - T = 0$ results in the equation of motion

$$EI\frac{\partial^4 Y}{\partial x^4} + \rho A\nu^2\frac{\partial^2 Y}{\partial x^2} + 2\rho A\nu\frac{\partial^2 Y}{\partial x \partial t} + M\frac{\partial^2 Y}{\partial t^2} = 0, \tag{10.3}$$

where $M = m + \rho A$ is the combined mass per unit length of the pipe and fluid. Finally, applying the cantilever boundary conditions

$$Y(0,t) = \frac{\partial Y}{\partial x}(0,t) = 0, \quad \frac{\partial^3 Y}{\partial x^3}(L,t) = \frac{\partial^2 Y}{\partial t^2}(L,t) = 0, \tag{10.4}$$

and inserting the trial solution

$$Y(x,t) = Real[\Psi(\frac{x}{L})e^{i\omega t}], \quad where \quad e^{i\omega t} = cos\omega t + isin\omega t \tag{10.5}$$

into the equation of motion, results in the equation:

$$\Psi'''' + V^2\Psi'' + 2i\beta^{\frac{1}{2}}V\Omega\Psi' - \Omega^2\Psi = 0 \tag{10.6}$$

where $\beta = \frac{\rho A}{M}, \Omega = \omega L^2\left(\frac{M}{EI}\right)^{\frac{1}{2}}, V = \nu L\left(\frac{\rho A}{EI}\right)^{\frac{1}{2}}$ and $'$ denotes the derivative with respect to $\frac{x}{L}$. It can be seen that the stability of the system depends on whether the dimensionless

constant Ω is greater or less than 0. By setting $\Omega = 0$ the onset of instability can therefore be expressed as a function of V and β. By choosing the values for all but one of the variables required to solve the system it was possible to obtain a full set of material properties for which the analytical solution for U_{cr} is known.

The geometry of the pipe was chosen as $L = 5.0$, $D_i = 0.2$, $D_o = \sqrt{2}D_i$, and the desired critical inflow velocity was chosen as $U_{cr} = 10.0$. Setting $\rho_f = 1.0$ and $\mu_f = 0.01$ resulted in a critical Reynolds number of $Re_{cr} = \frac{\rho_f U_{cr} D_i}{\mu_f} = 200$. By choosing $\frac{\rho_f A_f}{(\rho_f A_f + \rho_s A_s)} = 0.8$ the relationship $vL(\frac{\rho_f A_f}{E_s I_s})^{\frac{1}{2}} = 13.5$ was obtained. This relationship was then solved for the unknown value $E_s = 1829.0$.

10.2 Formulation of the Numerical Solution

An FSI simulation was performed by constructing a coupled system consisting of an unstructured fluid mesh of 34.5k 4-noded tetrahedral elements, and the same uniform solid mesh employed in the beginning of the previous chapter, consisting of 7200 8-noded linear elements. A range of constant flow velocities, parabolic at the inlet and stepped up sinusoidally from 0 over the first second of simulation, were then solved using the monolithic Newton solution method, and the translational behavior of the pipe recorded. The solid boundary conditions were set to being fully fixed at the inlet and free throughout the length of the pipe. The fluid boundary conditions were set as having the fluid fixed to the solid boundary, with a specified inflow and one point at the outlet fixed in pressure.

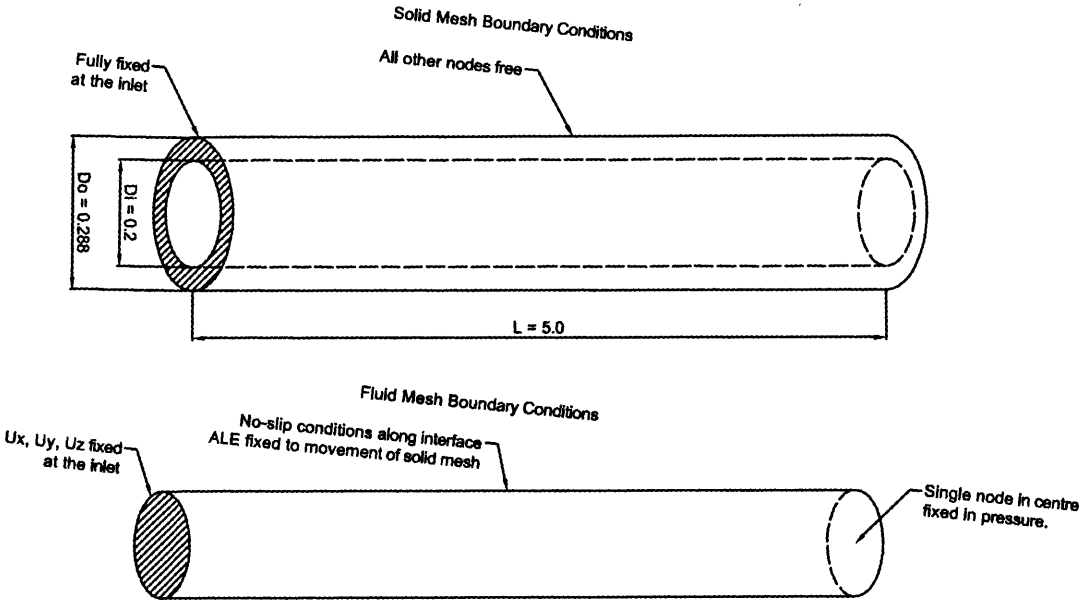

Figure 10.1: Diagram of boundary conditions.

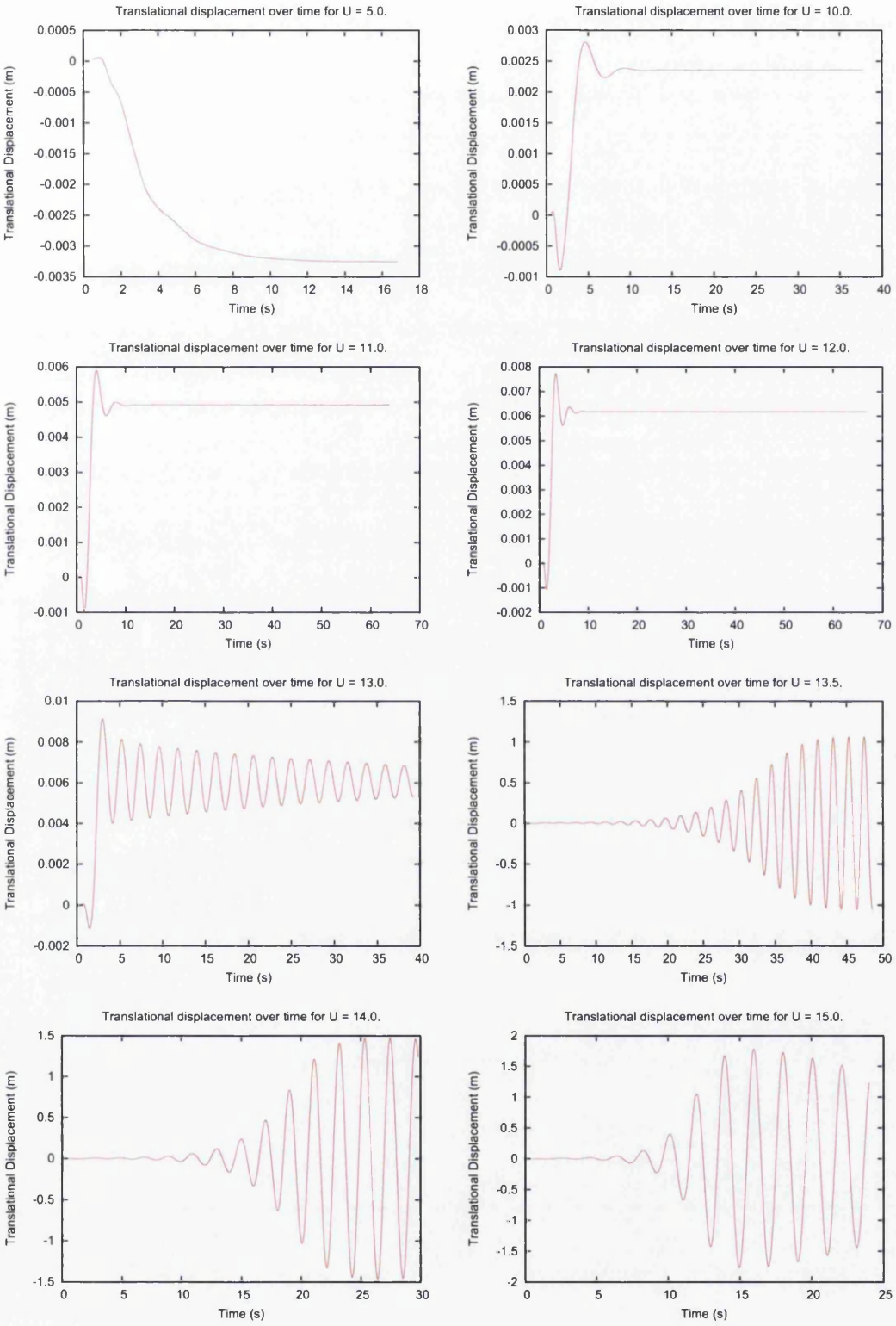

Figure 10.2: Diagrams displaying translational displacement of the free end of the pipe over time for varying steady inflow velocities.

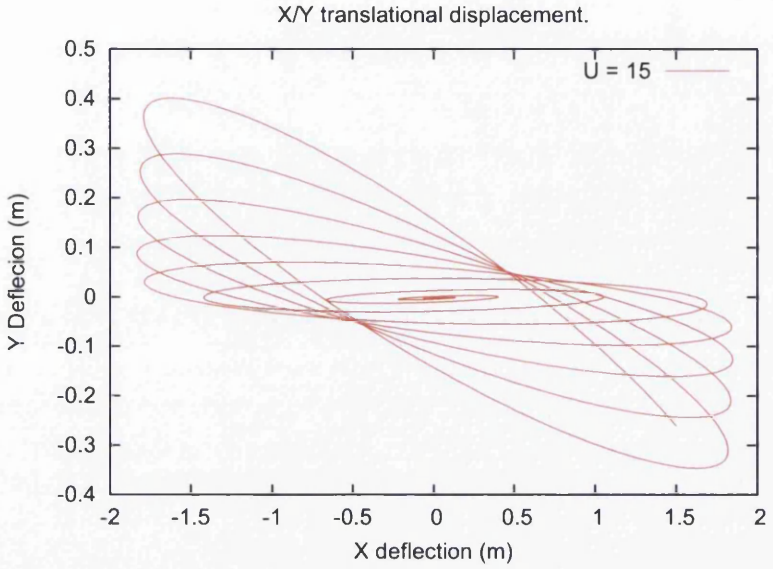

Figure 10.3: X vs Y translational displacement for hose with inflow velocity of 15 m/s.

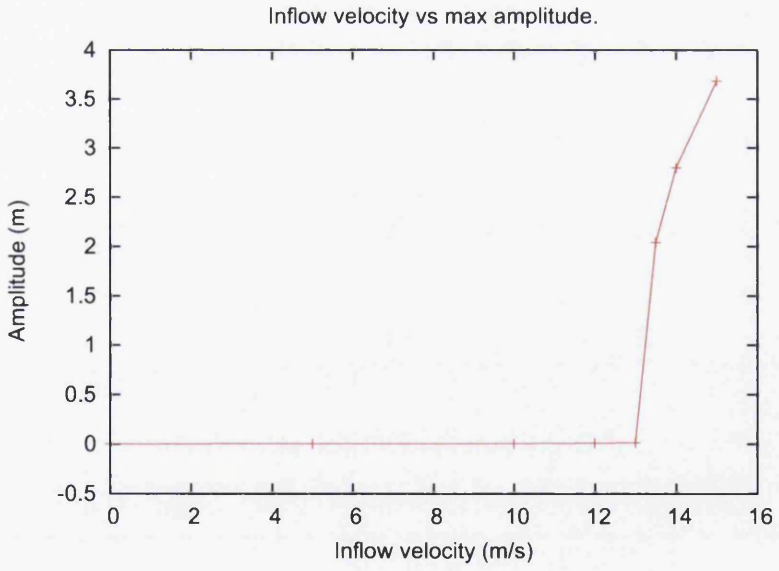

Figure 10.4: Inflow velocity vs maximum steady amplitude of oscillation.

10.3 Discussion of Results

One noticeable shortcoming of the analytical solution considered in this investigation is that it does not take into account radial and axial deformation of the pipe, only translational stability. By observing the behavior of the pipe at sub-critical inflow velocities it can be seen that these displacements can be as large as 5%. By taking the radial deformation into account and applying the principle of conservation of mass, an effective critical velocity can be calculated.

$$U_{cr} \times A_f = Q = U'_{cr} \times A'_f \tag{10.7}$$

Solving the above equation resulted in an effective critical velocity $U'_{cr} = 11$, however this still resulted in an error of 20.5% when compared to the numerical solution $U_{crn} = 13.25$. This disagreement may be a result of the alteration of the solid properties I_s, E_s and L due to the radial and axial deformation of the pipe. In order to dismiss the possibility of the numerical solution for a critical velocity not displaying an appropriate solid response due to the axisymmetric nature of the model problem, a numerical simulation was performed with an inflow velocity of $U'_{cr} < U < U_{crn}$ and a temporary force perpendicular to the length was applied at the end of the pipe for a small duration once the flow was fully realised throughout the length of the pipe. Figure 10.5 displays the results of this simulation, in which the pipe may be seen to return to a neutral displacement position after being displaced by the temporary force. This is a strong indication that the pipe is in a stable configuration, confirming that the inflow velocity of $U = 12.0$ is sub-critical for the numerical solution. It may therefore be concluded that the numerical result displays a good correspondence with the analytical solution considering the assumptions that are made in the formation of the analytical solution.

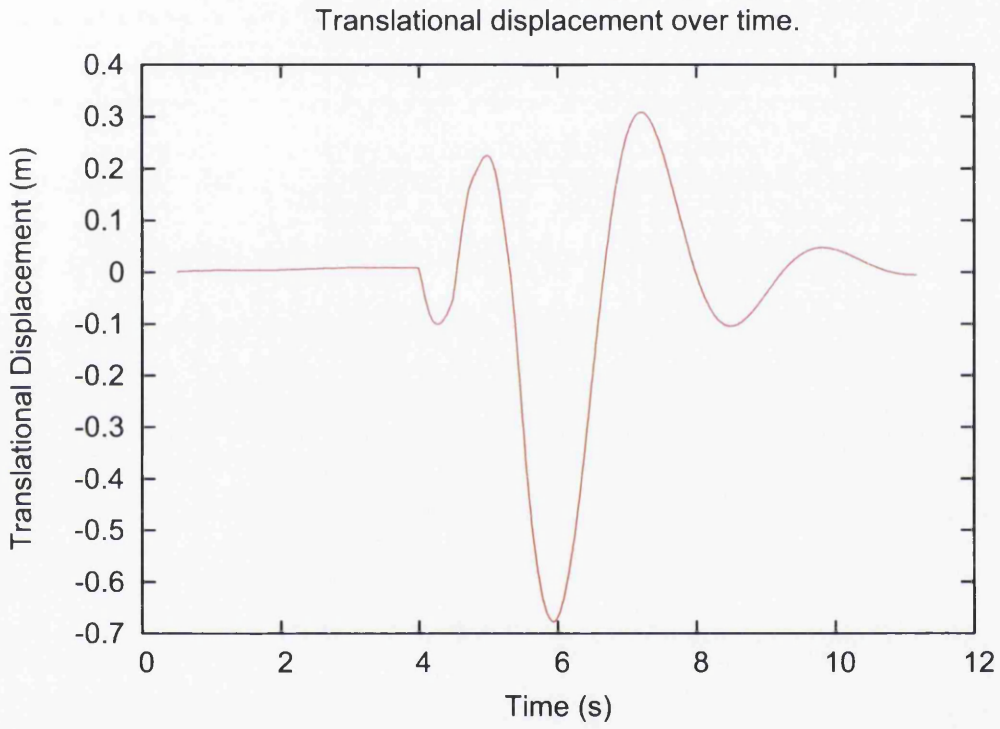

Figure 10.5: Translational displacement vs time for inflow U = 12 m/s with small perpendicular force at t=4.0-4.5s.

Chapter 11

Discussion and Conclusions

As detailed in section 1.2 the aim of this thesis was to present various three dimensional FSI model problems as well as to analyse the relative suitability of the monolithic Newton, block Gauss-Seidel, and novel staggered schemes presented in Chapter 6. Through the use of the three dimensional numerical examples presented in Chapters 7 - 10 this aim has been achieved. The relative strengths and weaknesses of the solvers have been presented based on criteria easily identified in the conceptual stage of a model problem, allowing the preemptive selection of the most suitable solver without the need for numerical analysis. Section 11.1 presents a summary of the conclusions reached throughout this work.

11.1 Final Assessment of Relative Solver Suitablility

Monolothic Newton Solver: Being the most computationally expensive and accurate solution method, this solver should only be employed when accuracy is the highest priority.

Block Gauss-Seidel Solver: Equal in computational cost and accuracy to the monolithic Newton method, this solver is rendered undesirable by the difficulty of handling small solid over fluid mass ratios.

Novel Staggered Scheme: Sacrificing a small amount of accuracy for one third the relative computational cost, this solver should be considered the most suitable for the majority of computational FSI problems. The exceptions being problems in which the highest accuracy is required, or those with a solid over fluid mass ratio less than one.

Table 11.1: Summary of Relative Criteria

	Solver		
Criteria	MN	GS	NS
Computational Cost	More	More	Less
Convergence	Quadratic	Linear	Quadratic
Accuracy	More	More	Less
Stability w.r.t. $\frac{m_{solid}}{m_{fluid}}$	More	Less	Less

11.2 Discussion and Recommendations for Future Work

The analysis conducted in this work is focused solely on the context of incompressible Newtonian fluid flow interacting with flexible solid structures. Logical extensions of this work for future research include:

- The three dimensional rendering of compressible or turbulent flow.
- Extending the interface to account for free surface flow and fluid-fluid interaction.
- Reduction of computational cost in order to apply computational FSI modelling to more complex model problems.
- Repeating the analysis performed in Chapter 10 using a stiffer material in order to reduce the radial and axial deformation of the solid, allowing for a more accurate comparison. This analysis may also be performed using other solution techniques in order to quantify relative accuracy.
- The establishment of quantitative values for the accuracy of solution techniques through comparison with reliable experimental data.

Bibliography

[1] K. J. Bathe (1996), *Finite Element Procedures*, Prentice Hall, New Jersey.

[2] Y. Bazilevs, V. M. Calo, Y. Zhang, and T. J. R. Hughes (2006), Isogeometric Fluid-Structure Interaction Analysis with Applications to Arterial Blood Flow, *Computational Mechanics*, Issue 4, Springer, Berlin Heidelberg, **38**: 310–322.

[3] M. Behr and T. Tezduyar (1999), The Shear-Slip Mesh Update Method, *Computer Methods in Applied Mechanics and Engineering*, **174**: 261–274.

[4] T. Belytschko, W. K. Liu, and B. Moran (2000), Nonlinear Finite Elements for Continua and Structures, *John Wiley & Sons*,Chichester, UK.

[5] R.D. Blevins (2001), *Flow-Induced Vibration*, Second Edition, Krieger, Malabar, Florida.

[6] J. Bonet and R. Wood (1997), Nonlinear Continuum Mechanics for Finite Element Analysis, *Cambridge University Press*, Cambridge, UK.

[7] H. Braess and P. Wriggers (2000), Arbitrary Lagrangian Eulerian Finite Element Analysis of Free Surface Flow, *Computer Methods in Applied Mechanics and Engineering*, **190**: 95–109.

[8] S. C. Brenner and L. R. Scott (2002), The Mathematical Theory of Finite Element Methods, *Springer*, 2nd Edition.

[9] F. Brezzi and J. Pitkäranta (1984), On the Stabilisation of Finite Element Approximations of the Stokes Equations, In W. Hackbusch, editor, *Efficient Solutions of Elliptic Systems*, volume 10 of *Notes on Numerical Fluid Mechanics*, Braunschweig, Wiesbaden.

[10] A. N. Brooks and T. J. R. Hughes (1982), Streamline-Upwind/Petrov-Galerkin Formulations for Convection Dominated Flows with Particular Emphasis on the Incompressible Navier-Stokes Equations, *Computer Methods in Applied Mechanics and Engineering*, **39**: 199–259.

[11] T. R. Chandrupatla and A.D. Belegundu (1997), Introduction to Finite Elements in Engineering, *Prentice Hall*, New Jersey, 3rd Edition.

[12] J. Chung and G. M. Hulbert (1993), A Time Integration Algorithm for Structural Dynamics with Improved Numerical Dissipation: The Generalized-α Method, *Journal of Applied Mechanics*, **60**: 371–375.

[13] P. G. Ciarlet (1978), The Finite Element Method for Elliptic Problems, *North-Holland*, Amsterdam.

[14] R. D. Cook, D. S. Malkus, M. E. Plesha, and R. J. Witt (2002), Concepts and Applications of Finite Element Analysis, *John Wiley & Sons*, 4th Edition

[15] M. A. Crisfield (1991), Non-Linear Finite Element Analysis of Solids and Structures, *John Wiley & Sons*, Chichester, UK.

[16] W. Dettmer (2004), *Finite Element Modelling of Fluid Flow with Moving Free Surfaces and Interfaces Including Fluid-Solid Interaction*, PhD thesis, University of Wales Swansea.

[17] W. Dettmer and D. Perić (2003), An Analysis of the Time Integration Algorithms for the Finite Element Solutions of Incompressible Navier-Stokes Equations Based on a Stabilised Formulation, *Computer Methods in Applied Mechanics and Engineering*, **192**: 1177–1226.

[18] W. Dettmer and D. Perić (2006), A Computational Framework for Free Surface Fluid Flows Accounting for Surface Tension, *Computer Methods in Applied Mechanics and Engineering*, **195**: 3038–3071.

[19] W. Dettmer and D. Perić (2006), A Computational Framework for Fluid-Rigid Body Interaction: Finite Element Formulation and Applications, *Computer Methods in Applied Mechanics and Engineering*, **195**, 1633–1666.

[20] W. Dettmer and D. Perić (2006), A Computational Framework for Fluid-Structure Interaction: Finite Element Formulation and Applications, *Computer Methods in Applied Mechanics and Engineering*, **195**, 5754–5779.

[21] W. Dettmer and D. Perić (2007), A Fully Implicit Computational Strategy for Strongly Coupled Fluid-Solid Interaction, *Archives of Computational Methods in Engineering*, **14,3**, 205–247.

[22] W. Dettmer and D. Perić (2008), On the Coupling Between Fluid Flow and Mesh Motion in the Modelling of Fluid-Structure Interaction, *Computational Mechanics*, **43,1**, 81–90.

[23] W. Dettmer and D. Perić (2011), A Novel Staggered Scheme for Fluid-Structure Interaction, *International Journal for Numerical Methods in Engineering*, **Accepted**, 1–23.

[24] W. Dettmer, P. H. Saksono, and D. Perić (2003), On a Finite Element Formulation for Incompressible Newtonian Fluid Flows on Moving Domains in the Presence of Surface Tension, *Communications in Numerical Methods in Engineering*, **19**: 659–668.

[25] J.Donea (1983), Arbitrary Lagrangian-Eulerian Finite Element Methods, in T. Belytschko and T. J. R. Hughes, editors, *Computational Methods for Transient Analysis*, Elsevier Science Publishers, 473–516.

[26] J. H. Ferziger and M. Perić (2002), Computational Methods for Fluid Dynamics, *Springer*, Berlin/Heidelberg, Germany, 3rd Edition.

[27] J. P. Den Hartog (1956), *Mechanical Vibrations*, Fourth Edition, Mc Graw-Hill Book Company, New York, Toronto, London.

[28] C. W. Hirt, A. A. Amsden, and J. L. Cook (1974), An Arbitrary Lagrangian Eulerian Computing Method for all Flow Speeds, *Journal of Computational Physics*, **14**: 227–253.

[29] J. Hron and S. Turek (2006), A Monolithic FEM/Multigrid Solver for an ALE Formulation of Fluid-Structure Interaction with Applications in Biomechanics, In H. J. Bungartz and M. Schäfer editors, *Fluid-Structure Interaction*, Springer, Berlin Heidelberg, **53**: 146–170.

[30] B. Hübner, E. Wallhorn, and D. Dinkler (June 2001), Strongly Coupled Analysis of Fluid-Structure Interaction Using Space-Time Finite Elements, *ECCM*, Cracow, Poland.

[31] A. Huerta and W. K. Liu (1988), Viscous Flow with Large Free Surface Motion, *Computer Methods in Applied Mechanics and Engineering*, **69**: 277–324.

[32] T. J. R. Hughes (1987), The Finite Element Method: Linear Static and Dynamic Finite Element Analysis, *Prentice Hall*, New Jersey.

[33] T. J. R. Hughes, L. P. Franca, and M. Balestra (1986), A New Finite Element Formulation for Computational Fluid Dynamics: V. Circumventing the Babuska-Brezzi Condition: A Stable Petrov-Galerkin Formulation of the Stokes Problem Accomodating Equal-Order Interpolations, *Computer Methods in Applied Mechanics and Engineering*, **59**: 85–99.

[34] T. J. R. Hughes, W. K. Liu and T. K. Zimmermann (1981), Lagrangian-Eulerian Finite Element Formulation for Incompressible Viscous Flows, *Computer Methods in Applied Mechanics and Engineering*, **29**: 329–349.

[35] K. E. Jansen, C. H. Whiting, and G. M. Hulbert (2000), A Generalized-α Method for Integrating the Filtered Navier-Stokes Equations with a Stabilized Finite Element Method, *Computer Methods in Applied Mechanics and Engineering*, **190**: 305–319.

[36] C. Johnson (1987), Numerical Solution of Partial Differential Equations by the Finite Element Method, *Cambridge University Press*, Cambridge.

[37] C. Johnson, U. Nävert and J. Pitkäranta (1984), Finite Element Methods for Linear Hyperbolic Problems, *Computer Methods in Applied Mechanics and Engineering*, **45**: 285–312.

[38] C. Johnson and J. Saranen (1986), Streamline Diffusion Methods for the Incompressible Euler and Navier-Stokes Equations, *Mathematics of Computation*, **47(175)**: 1–18.

[39] M. M. Joosten, W. Dettmer, and D. Perić (2009), Analysis of the block Gauß-Seidel solution procedure for a strongly coupled model problem with reference to fluid-structure interaction, *International Journal for Numerical Methods in Engineering*, **78**, 757–778.

[40] M. M. Joosten, W. Dettmer, and D. Perić (2010), On the temporal stability and accuracy of coupled problems with reference to fluid-structure interaction, *International Journal for Numerical Methods in Fluids*, **64**, 1363–1378.

[41] C. Kassiotis, A. Ibrahimbegovic, R. Niekamp and H. G.Matthies (2011), Nonlinear fluid-structure interaction problem. Part I: Implicit partitioned algorithm, nonlinear stability proof and validation examples, *Computational Mechanics*, **47**, 305–323.

[42] C. Kassiotis, A. Ibrahimbegovic, R. Niekamp and H. G.Matthies (2011), Nonlinear fluid-structure interaction problem. Part II: Space discretization, implementation aspects, nested parallelization and application examples, *Computational Mechanics*, **47**, 335–357.

[43] L. Kinsler and A. Frey (1962), *Fundamentals of Acoustics*, Second Edition, Wiley, New York.

[44] T. Nomura and T. R. J. Hughes (1992), An Arbitrary Lagrangian-Eulerian Finite Element Method for Interaction of Fluid and a Rigid Body, *Computer Methods in Applied Mechanics and Engineering*, **95**: 115–138.

[45] A. Masud and T. J. R. Hughes (1997), A Space-Time Galerkin/Least-Squares Finite Element Formulation of the Navier-Stokes Equations for Moving Domain Problems, *Computer Methods in Applied Mechanics and Engineering*, **146**: 91–126.

[46] D. Perić and S. Slijepčević (2001), Computational Modelling of Viscoplastic Fluids Based on a Stabilised Finite Element Method, *Engineering Computations*, **18**: 577–591.

[47] B. Ramaswamy (1990), Numerical Simulation of Unsteady Viscous Free Surface Flow, *Journal of Computational Physics*, **90**: 396–430.

[48] B. Ramaswamy and M. Kawahara (1987), Arbitrary Lagrangian-Eulerian Finite Element Method for Unsteady, Convective, Incompressible Viscous Free Surface Fluid Flow, *International Journal for Numerical Methods in Fluids*, **7**: 1053–1075.

[49] B. D. Reddy (1998), Introduction to Functional Analysis, *Springer*

[50] P. A. Sackinger, P. R. Schunk, and R. R. Rao (1996), A Newton-Raphson Pseudo-Solid Domain Mapping Technique for Free and Moving Boundary Problems: A Finite Element Implementation, *Journal of Computational Physics*, **125**: 83–103.

[51] P. H. Saksono, W. Dettmer, and D. Perić (2007), An adaptive remeshing strategy for flows with moving boundaries and fluid-structure interaction, *International Journal for Numerical Methods in Engineering*, **71,9**, 1009–1050.

[52] J. Sarrate, A. Huerta, and J. Donea (2001), Arbitrary Lagrangian-Eulerian Formulation for Fluid-Rigid Body Interaction, *Computer Methods for Applied Mechanics and Engineering*, **190**: 3171–3188.

[53] M. von Scheven, E. Ramm (2011), Strong coupling schemes for interaction of thin-walled structures and incompressible flows, *International Journal for Numerical Methods in Engineering*, **87**, 214–231.

[54] C. Schwab (1998), p- and hp-Finite Element Methods. Theory and Applications to Solid and Fluid Mechanics, *Oxford University Press*, Oxford.

[55] S. Slijepčević (2003), *Computational Modelling of Non-Newtonian Fluids Based on the Stabilised Finite Element Method*, PhD Thesis, University of Wales Swansea, School of Engineering, Civil and Computational Engineering Centre.

[56] A. Soulaimani, M. Fortin, G. Dhatt, and Y. Ouellet (1991), Finite element simulation of two- and three-dimensional free surface flows, *Computer Methods in Applied Mechanics and Engineering*, **86**: 265–296.

[57] A. Soulaimani and Y. Saad (1998), An Arbitrary Lagrangian-Eulerian Finite Element Method for Solving Three-Dimensional Free Surface Flows, *Computer Methods in Applied Mechanics and Engineering*, **162**: 79–106.

[58] T. E. Tezduyar, M. Behr, and J. Liou (1992), A New Strategy for Finite Element Computations Involving Moving Boundaries and Interfaces - The Deforming-Spatial-Domain/Space-Time Procedure: I. The Concept and the Preliminary Numerical Tests, *Computer Methods in Applied Mechanics and Engineering*, **94**: 339–351.

[59] T. E. Tezduyar, M. Behr, and J. Liou (1992), A New Strategy for Finite Element Computations Involving Moving Boundaries and Interfaces - The Deforming-Spatial-Domain/Space-Time Procedure: II. Computation of Free-Surface Flows, Two-Liquid Flows and Flows with Drifting Cylinders, *Computer Methods in Applied Mechanics and Engineering*, **94**: 353–371.

[60] T. E. Tezduyar, S. Mittal, S. E. Ray, and R. Shih (1992), Incompressible Flow Computations with Stabilized Bilinear and Linear Equal-Order-Interpolation Velocity-Pressure Elements, *Computer Methods in Applied Mechanics and Engineering*, **95**: 221–242.

[61] W. A. Wall and E. Ramm (1998), Fluid-structure interaction based upon a stabilized (ALE) finite element method, in S. R. Idelsohn and E. Onate, editors, *Computational Mechanics - New Trends and Applications, 4th World Congress on Computational Mechanics*, CIMNE, Barcelona, Spain.

[62] O. C. Zienkiewicz and R. L. Taylor (2000), The Finite Element Method, *Butterworth-Heinemann*, Oxford, UK, 5th Edition.